

# **SYNTHESIS AND CHARACTERIZATION OF THERMOELECTRIC MATERIALS FOR EFFICIENT HARNESSING OF SOLAR ENERGY**

by

**M. SARAVANAN**

**(Enrolment No: 2K12/Ph.D./ME/05)**

**DEPARTMENT OF MECHANICAL ENGINEERING**

Submitted

in fulfillment of the requirements for the degree of

**DOCTOR OF PHILOSOPHY**

to the



**DELHI TECHNOLOGICAL UNIVERSITY**

**JUNE 2018**

©DELHI TECHNOLOGICAL UNIVERSITY-2018  
ALL RIGHTS RESERVED



**DELHI TECHNOLOGICAL UNIVERSITY**

**BAWANA ROAD, DELHI – 110042**

**CERTIFICATE**

---

This is to certify that the Ph.D. thesis entitled "*Synthesis and characterization of thermoelectric materials for efficient harnessing of solar energy*" being submitted by **M. Saravanan (Enrolment No.: 2K12/PhD/ME/05)** for the award of degree of *Doctor of Philosophy (Ph.D.)* in Mechanical Engineering, Delhi Technological University, is an authentic work carried out by him under our guidance and supervision.

It is further certified that the work is based on original research and the matter embodied in this thesis has not been submitted earlier for the award of any degree or diploma to the best of our knowledge and belief.

**Dr. R. C. Singh**

Professor,  
Department of Mechanical Engineering,  
Delhi Technological University,  
Delhi 110042.

**Dr. Ajay Dhar**

Head & Chief Scientist,  
Advanced Materials & Devices Division,  
CSIR- National Physical Laboratory,  
New Delhi 110012.

**Dr. B. D. Pathak**

Professor,  
Department of Mechanical Engineering,  
Delhi Technological University,  
Delhi 110042.



## ACKNOWLEDGEMENTS

---

I would like to express my deep gratitude, sincere thanks and appreciation to my supervisors Prof. R.C. Singh, Prof. B.D. Pathak and Dr. Ajay Dhar for their valuable guidance for the last six years time. I thank you from my heart for all the help, encouragement, and support you generously extended to me during the six years time.

I would like to express, sincere gratitude to Director, CSIR-National Physical Laboratory (NPL), Head of the Department & DRC Chairman, Mechanical Engineering, Delhi Technological University, for their valuable help and extending all the necessary processing and characterization facilities during my research work.

Thanks are also due to Prof. L.M. Das, Prof. R.K. Pandey, Dr. Rajesh Kumar and Dr. Ramesh Srivastava, for serving my SRC committee and much critical help without which I would not be able to complete my thesis in time.

I also thank Dr. A. K. Srivastava for TEM work and Dr. Sreekumar Chockalingam for nanoindentation characterization. I would like to express my sincere thanks to Prof. R.C. Budhani, Dr. R.P. Aloysius, Dr. Jiji Pulikkotil and Dr. N. Vijayan for their teaching and help without that I would not be able to finish my thesis in time.

I would like to express my sincere thanks to Prof. Rajiv Chaudhary, Prof. Ranganath M. Singari & Mr. Roop Lal for their teaching and help during my research work. My sincere thanks to all the faculty and staff members of Department of Mechanical Engineering (DTU), who supported me during my entire coursework and research work. I am grateful to Rajesh Bohra, Radhey Shyam, and N. K. Upadhyay for their technical and experimental support.

I would like to express my sincere thanks to fellow scientists, Dr. Bathula Sivaiah, Dr. Bhasker Gahtori and Dr. Nidhi Singh, Technical and Supporting staffs and my students for their support and encouragement throughout this period.

I gratefully acknowledge Council of Scientific and Industrial Research for sponsoring CSIR-TAPSUN programme under the project (NWP-54) entitled “Novel approaches for solar energy conversion under technologies and products for solar energy utilization through networking.”

I would also like to thank Appa and Amma for their support. I am grateful to my wife Mrs. Rohini for her support and encouragement during the six years time. Finally, I dedicate this Ph.D. thesis to my dearest son Suraj, for his love and cuteness.

## ABSTRACT

---

Thermoelectric generators (TEGs), based on the Seebeck effect, which converts heat into useful electrical energy, are gaining momentum for renewable energy applications. However, it is well accepted that for the thermoelectric technology to compete with other recognized green-energy generation technologies, like photovoltaics, the material, and manufacturing costs of thermoelectric devices, have to be significantly reduced. Also, the majority of the presently available competent thermoelectric materials possess expensive constituent materials (Te, Ge, Ag, rare-earths, etc.), which adds another dimension to this problem. Thus, the thrust of thermoelectric research for energy generation is currently focussed on the development of n and p-type materials, which are thermoelectrically compatible, thermally stable and consisting of elements that are earth-abundant and non-toxic.  $\text{Mg}_2\text{Si}$  (*n-type*) and  $\text{MnSi}_{1.73}$  (*p-type*) are the ideal combinations for developing a cost-effective and non-toxic thermoelectric device due to their Seebeck coefficient compatibility, thermal and chemical stability and low density.

The present work is an emphasis on the synthesis and characterization of two such thermoelectric compounds, n-type  $\text{Mg}_2\text{Si}$ , and p-type  $\text{MnSi}_{1.73}$ , as cost-effective thermoelectric technology, which is anticipated to play a vital role in meeting the energy challenge of the future. This present work reports the synthesis of  $\text{Mg}_2\text{Si}$  and  $\text{MnSi}_{1.73}$  using reactive spark plasma assisted sintering process, which consumes only a limited processing time as compared to long duration hours using conventional manufacturing techniques. The phase crystal structure, chemical composition, and microstructure of synthesized materials were studied employing X-ray diffraction, high-resolution electron microscopy, and energy dispersive spectroscopy techniques. The electrical conductivity, thermal conductivity and Seebeck coefficient of synthesized  $\text{Mg}_2\text{Si}$  and  $\text{MnSi}_{1.73}$  have been studied, to understand its thermal-electric conversion efficiency. The mechanical performance of synthesized materials is also crucial to circumvent the unexpected structural failure of their components during actual operational conditions. The comprehensive spectrum of mechanical properties of synthesized  $\text{Mg}_2\text{Si}$  and  $\text{MnSi}_{1.73}$  has been studied, to recognize the durability of these thermoelectric materials, under actual working environmental conditions.

# TABLE OF CONTENTS

---

Acknowledgements.....	(i)
Abstract.....	(ii)
List of Tables.....	(vii)
List of Figures.....	(viii)
Abbreviations.....	(xiv)
Symbols and Physical Constants .....	(xv)

## CHAPTER 1: INTRODUCTION

1.1.	Thermoelectric background .....	1
1.2.	Thermoelectric efficiency .....	2
1.3.	Seebeck effect .....	3
1.4.	Electrical conductivity .....	5
1.5.	Thermal conductivity .....	6
1.6.	Energy Band Gap .....	8
1.7.	Carrier concentration .....	9
1.8.	Mobility.....	10
1.9.	Figure-of-Merit (ZT).....	11
1.10.	Strategies to maximize the thermoelectric performance.....	12
1.11.	Thermoelectric materials for low-temperature applications (< 500 K) .....	13
1.12.	Thermoelectric materials for mid temperature applications (500 -900 K) ..	14
1.13.	Thermoelectric materials for high-temperature applications ( > 900 K) .....	15
1.14.	Applications of thermoelectrics .....	17
1.14.1.	Space applications .....	17
1.14.2.	Automotive applications .....	17
1.14.3.	Industrial waste heat applications .....	18
1.14.4.	Marine applications .....	18
1.14.5.	Aerospace applications.....	19
1.14.6.	Wearables .....	19
1.14.7.	Consumer Products .....	19

1.14.8.	Solar application of thermoelectrics .....	20
1.15.	Motivation and objectives .....	26
<b>CHAPTER 2 : LITERATURE REVIEW</b>		
2.1.	Introduction .....	29
2.2.	N-type Magnesium Silicides .....	30
2.3.	P-type Manganese Silicides .....	35
<b>CHAPTER 3 : EXPERIMENTS DETAILS</b>		
3.1.	Introduction .....	39
3.2.	Experimental techniques used for material synthesis .....	39
3.2.1.	High Energy Ball Milling (HEBM) .....	39
3.2.2.	Melt Spinning equipment .....	42
3.2.3.	Spark plasma sintering .....	44
3.3.	Experimental techniques used for material characterization .....	47
3.3.1.	X-ray diffraction analysis .....	47
3.3.2.	Scanning electron microscope analysis .....	49
3.3.3.	Transmission electron microscope analysis .....	51
3.4.	Experimental techniques used for thermoelectric transport properties measurements .....	52
3.4.1.	Thermal transport properties .....	52
3.4.1.1.	Thermal diffusivity measurement .....	53
3.4.1.2.	Specific heat capacity measurement .....	54
3.4.1.3.	Density measurement .....	55
3.4.1.	Electrical transport properties .....	56
3.4.1.1.	Seebeck coefficient measurement & Electrical conductivity measurement .....	56
3.4.1.2.	Hall properties measurement .....	58
3.5.	Experimental techniques used for mechanical properties measurements ....	58
3.5.1.	Vickers hardness test .....	58
3.5.2.	Nanoindentation test .....	60
3.5.3.	Wear and friction test .....	63



## **CHAPTER 4 : MICROSTRUCTURE AND THERMOELECTRIC PROPERTIES OF N-TYPE MAGNESIUM SILICIDE**

4.1.	Single doped n-type Magnesium Silicide .....	65
4.1.2.	Introduction.....	65
4.1.2.	Experimental details.....	66
4.1.3.	X-ray diffraction Analysis .....	68
4.1.4.	Microstructural analysis.....	69
4.1.5.	Thermoelectric properties .....	73
	4.1.5.1. Electronic transport properties .....	73
	4.1.5.2. Thermal transport properties.....	74
	4.1.5.3. Figure-of-merit (ZT) .....	75
4.1.6.	Conclusions.....	77
4.2.	Double doped n-type Magnesium Silicide.....	78
4.2.1.	Introduction.....	78
4.2.2.	Experimental details.....	79
4.2.3.	X-ray diffraction Analysis .....	80
4.2.4.	Microstructural analysis.....	80
4.2.5.	Thermoelectric properties .....	82
	4.2.5.1. Electronic transport properties .....	82
	4.2.5.2. Thermal transport properties.....	82
	4.2.5.3. Figure-of-merit.....	83
4.2.6.	Conclusions.....	84

## **CHAPTER 5 : MICROSTRUCTURE AND THERMOELECTRIC PROPERTIES OF P-TYPE HIGHER MANGANESE SILICIDE**

5.1.	Bulk p-type Higher Manganese Silicides .....	85
5.1.1.	Introduction.....	85
5.1.2.	Experimental details.....	88
5.1.3.	X-ray diffraction Analysis .....	89
5.1.4.	Microstructural analysis.....	90
5.1.5.	Thermoelectric properties .....	93
	5.1.5.1. Electronic transport properties .....	93

5.1.5.2.	Thermal transport properties .....	95
5.1.5.3.	Figure-of-merit.....	98
5.1.6.	Conclusions.....	98
5.2.	Nanostructured p-type Higher Manganese Silicides.....	100
5.2.1.	Introduction.....	100
5.2.2.	Experimental details.....	102
5.2.3.	X-ray diffraction analysis.....	106
5.2.4.	Microstructural analysis .....	108
5.2.5.	Thermoelectric properties .....	113
5.2.5.1.	Electronic transport properties .....	113
5.2.5.2.	Thermal transport properties .....	114
5.2.5.3.	Figure-of-merit.....	115
5.2.6.	Conclusions.....	117
<b>CHAPTER 6 : MECHANICAL PROPERTIES OF THERMOELECTRIC N-TYPE MAGNESIUM SILICIDE &amp; P-TYPE HIGHER MANGANESE SILICIDE</b>		
6.1.	Introduction.....	118
6.2.	Experimental Details.....	120
6.3.	Microhardness analysis .....	121
6.4.	Nanoindentation analysis .....	124
6.5.	Fracture toughness analysis .....	127
6.6.	Thermal shock resistance studies.....	132
6.7.	Friction and wear studies .....	133
6.8.	Worn surface analysis .....	136
6.9.	Conclusions.....	141
<b>CHAPTER 7 : CONCLUSIONS AND SCOPE OF FUTURE WORK</b>		
7.1.	Conclusions.....	143
7.2.	Scope of future work.....	146

## References

## Publications List

## Author's Bio-data

## LIST OF TABLES

---

Table 1.1.	The Seebeck coefficient values of some common materials	5
Table 1.2.	Thermal conductivity values of some common materials	8
Table 1.3.	Materials and temperature ranges deployed in solar thermoelectric generation systems	24
Table 5.1.	The crystallite sizes and transport parameters of the melt-spun combined spark plasma sintered higher manganese silicides processed at different wheel speeds	105

## LIST OF FIGURES

---

Figure 1.1. Schematic diagram of Seebeck effect	4
Figure 1.2. Schematic of Solar Thermoelectric power conversion	20
Figure 1.3. Schematic of Concentrated Solar Power Thermoelectric conversion	22
Figure 1.4. Thermoelectric generator used in different solar thermal non-concentrating(a) and concentrating linear fresnel lens(b), Parabolic power(c) systems.	23
Figure 2.1. Materials cost for thermoelectric applications	30
Figure 2.2. Schematic diagram of atomic positions in the cubic structure lattice ( $Mg_2Si$ ), red color spheres indicate Mg and green indicate Si atoms.	31
Figure 2.3. The Mg-Si phase diagram showing the $Mg_2Si$ phase.	32
Figure 2.4. Schematic diagram of atomic positions in the tetragonal structure of $MnSi_{1.75}$ , red color spheres indicates Mn and green indicate Si atoms	35
Figure 2.5. The Mn-Si phase diagram showing the HMS phase, narrow range $MnSi_{1.7}$ to $MnSi_{1.75}$	36
Figure 3.1. (a) High energy ball mill (M/s. Fritsch, Pulverisette, P-4, Germany) used for ball milling (b) Schematic diagram showing the ball movement inside the ball mill and (c) powder particles trapped between the balls.	41
Figure 3.2. Glove box used for loading and unloading of ball milled powders from the Stainless Steel Jars (Make: Mbraun, Germany, Model: MB20)	42
Figure 3.3. Schematic of Melt spinning process	43
Figure 3.4. (a) Melt Spinning Unit (Make: Edmund Buhler GmbH, Model: Melt Spinner HV) used for synthesizing	

nanostructured ribbons/flakes (b) Water cooled Copper wheel with crucible	44
Figure 3.5. (a) Spark plasma sintering facility (SPS 725, Fuji electric co., Japan) used for materials synthesis (b) principle of operation.	46
Figure 3.6. (a) Basic principles of X-ray diffraction and Bragg's law, (b) X-ray Diffractometer used for characterization of crystal structure and phase purity of synthesized materials ( Rigaku, Japan, Model- Miniflex-II)	48
Figure 3.7. The schematic and working principle of Field emission scanning electron microscope	50
Figure 3.8. Field emission scanning electron microscope (Zeiss, Supra 40VP, Germany) used for microstructure analysis.	51
Figure 3.9. a) High-Resolution Transmission electron microscope ( Tecnai G2 F30 STWIN, Germany) used for nanostructure and lattice scale imaging (b) Schematic and working principle of HR-TEM	52
Figure 3.10.(a) Thermal diffusivity measurement (LFA 1000. Linseis, Germany) facility (b) Schematic and working principle.	53
Figure 3.11.(a) Differential scanning calorimeter used for Specific heat (Cp) measurements ( Make: Netzsch, Germany, Model: 404 F3)	55
Figure 3.12.Density measurement setup (M/S. Mettler Toledo)	56
Figure 3.13.(a) Seebeck coefficient and electrical resistivity measurement (M/s. ULVAC, ZEM-3, Japan) facility (b) Schematic and working principle.	57
Figure 3.14.(a) Vickers micro-hardness testing (Future Tech. Corp., FM-e7) used for hardness and fracture toughness measurement and (b) principle of indentation and measurement	59
Figure 3.15.(a) Schematic of nano-indentation method, (b) load-displacement	61
Figure 3.16.Nanoindentation equipment (Fischer-Cripps, Model: IBIS-B, Australia) used for Nanomechanical properties measurement	62

Figure 3.17. Sliding wear and friction machine (Ducom, Model: TR20LE, India) used for tribological properties measurement, (b) disc and (c) pin specimens used for evaluation	63
Figure 4.1. The photograph showing (a) SPS processing zone while sintering, and (b) SPS synthesized n-type doped Mg <sub>2</sub> Si pellets.	68
Figure 4.2. X-ray powder diffraction pattern of spark plasma sintered undoped, 1at% and 2 at % doped n-type Mg <sub>2</sub> Si	68
Figure 4.3. HR-TEM microstructures of SPS processed magnesium silicide exhibiting (a) the grains distribution, (b) a magnified view of Mg <sub>2</sub> Si grains, (c) an atomic lattice scale image, and (d) a grain boundary	70
Figure 4.4. HR-TEM microstructures of single element doped Mg <sub>2</sub> Si exhibiting (a) grains distribution, (b) a magnified view of Mg <sub>2</sub> Si grains and subgrains, (c) an atomic lattice scale image at a junction, and (d) Doped Mg <sub>2</sub> Si grain at atomic scale	71
Figure 4.5. HR-TEM microstructure of single doped Mg <sub>2</sub> Si material showing the evidence of Mg <sub>2</sub> Pb particles in the Mg <sub>2</sub> Si matrix. FFT (inset (b)) reveals the cubic Mg <sub>2</sub> Pb crystal structure. Inset(c) reveals Mg <sub>2</sub> Pb nano-particle at low magnification microstructure	73
Figure 4.6. Thermoelectric properties of undoped and single doped Mg <sub>2</sub> Si. (a) electrical conductivity, (b) Seebeck coefficient, (c) thermal conductivity, (d) figure-of-merit (ZT).	75
Figure 4.7. Schematic representation of grain & grain boundary model of synthesized doped Mg <sub>2</sub> Si	76
Figure 4.8. The X-ray powder diffraction pattern of spark plasma sintered (a) undoped, (b) Pb and Bi-doped, (c) Pb and Sb-doped, and (d) Sb and Bi-doped	80
Figure 4.9. SEM images of sintered Mg <sub>2</sub> Si. (a) undoped, (b) Pb and Sb-doped, (c) Pb and Bi-doped, and (d) Sb and Bi-doped.	81
Figure 4.10. Temperature dependence of (a) the electrical conductivity and (b) the Seebeck coefficient of double-doped Mg <sub>2</sub> Si during heating and cooling.	82

Figure 4.11. Temperature dependence of undoped and double-doped Mg <sub>2</sub> Si (a) electrical conductivity, (b) Seebeck coefficient, (c) thermal conductivity, (d) figure-of-merit (ZT).	83
Figure 5.1. Crystal structures of higher manganese silicides showing different tetragonal phases Mn <sub>4</sub> Si <sub>7</sub> , Mn <sub>11</sub> Si <sub>19</sub> , Mn <sub>15</sub> Si <sub>26</sub> , and Mn <sub>27</sub> Si <sub>47</sub> , with same lattice constant 'a' of ~ 0.552 nm and different lattice constants 'c' of ~ 1.75, 4.81, 6.53 and 11.8 nm, respectively	87
Figure 5.2. The photograph showing (a) SPS processing zone while sintering, and (b) SPS synthesized p-type doped MnSi <sub>1.73</sub> pellets.	89
Figure 5.3. X-ray powder diffraction pattern of spark plasma sintered undoped and Al doped MnSi <sub>1.73</sub>	90
Figure 5.4. SEM images of (a) SPS processed HMS (MnSi <sub>1.73</sub> ), and showing the individual elemental maps of (b) Mn, (c) Si and (d) EDS spectrum.	91
Figure 5.5. SEM images of (a) SPS processed Al-doped HMS (MnSi <sub>1.73</sub> ) sample, and showing the individual elemental maps of (b) Mn, (c) Si and (d) EDS spectrum	92
Figure 5.6. HR-TEM microstructures of Al-doped HMS (MnSi <sub>1.73</sub> ) revealing (a) grains distribution, (b) atomic scale image, and (c) atomic scale image of HMS with extra primary silicon. Insets: (A) Si and HMS grain, (B) diffraction pattern of HMS grain, and (c) diffraction pattern of silicon.	94
Figure 5.7. Temperature dependence of the thermoelectric properties of the synthesized undoped HMS sample (a) Seebeck coefficient and electrical conductivity, (b) total and lattice thermal conductivity, (c) power factor and figure-of-merit.	97
Figure 5.8. Temperature dependence of the thermoelectric properties of sintered Al-doped HMS (a) Seebeck coefficient and electrical conductivity, (b) total and lattice thermal conductivity, (c) power factor and figure-of-merit.	99
Figure 5.9. The photograph showing the process flow of bulk nanostructured Al-doped HMS synthesis, employing Melt spinning combined with Spark plasma sintering	103
Figure 5.10. Variations of Ribbon thickness and cooling rate, at different wheel speeds (15, 23 & 30 m/s) during Melt spinning process	104

Figure 5.11. X-ray diffraction pattern of processed HMS samples (a) melt-spun flakes/ribbons (b) melt-spinning combined spark plasma sintered HMS and (c) peak broadening, at a different wheel speeds	107
Figure 5.12. SEM micrographs of the melt-spun processed HMS ribbons/flakes and corresponding grain distributions, at different wheel speeds (a) 15 m/s, (b) 23 m/s and (c) 30 m/s	109
Figure 5.13. (a) SEM micrographs of Melt-spun ribbons and its EDS spectrum (inset); (b), (c) and (d) individual elemental maps of melt-spun HMS	110
Figure 5.14. (a) SEM micrographs of spark plasma sintered HMS and its EDS spectrum (inset); (b), (c) and (d) individual elemental maps of the SPS processed HMS	110
Figure 5.15. HR-TEM microstructures of melt-spinning and spark plasma sintered HMS (a) grains distribution of melt-spun ribbons, (b) magnified view of the grains, (c) a complex microstructure of melt-spin & spark plasma sintered sample, and (d) atomic scale image of (c) showing the planes, (e) Silicon nanoparticles and (f) atomic scale image of a nano-sized Si. Insets: (A) electron diffraction pattern of HMS grains, (B) grain boundaries, and (C) atomic scale image, (D) atomic scale image of a grain boundary, and (E) Moire fringes and a set of atomic planes	112
Figure 5.16. Thermoelectric properties of melt-spinning combined with spark plasma sintered HMS (a) Seebeck coefficient and electrical conductivity, (b) total and lattice thermal conductivity, (c) power factor and figure-of-merit.	116
Figure 6.1. Microhardness values of synthesized (a) n-type $Mg_2Si$ , (b) p-type $MnSi_{1.73}$ , at different applied load conditions.	123
Figure 6.2. A load-displacement (P-H) curves of synthesized (a) n-type $Mg_2Si$ , (b) p-type $MnSi_{1.73}$ , at different applied load conditions.	126
Figure 6.3. Load dependence nanoindentation results SPS synthesized n-type $Mg_2Si$ : (a) Hardness (GPa) and, (b) Elastic modulus (GPa)	128
Figure 6.4. Load dependence nanoindentation results SPS synthesized p-type $MnSi_{1.73}$ : (a) Hardness (GPa) and, (b) Elastic modulus (GPa)	129



Figure 6.5. Electron microscope images of indentation cracks of (a) n-type $\text{Mg}_2\text{Si}$ and, (b) p-type $\text{MnSi}_{1.73}$	131
Figure 6.6. Photographs showing the worn-out surfaces of Pin & Disc tribo-pair	133
Figure 6.7. (a) Wear rate and Wear coefficient values, as a function of sliding velocity with 10,30,50 N load conditions	135
Figure 6.8. The coefficient of friction ( $\mu$ ) as a function of sliding distance (m) with different applied load conditions (a) 10 & (b) 30 and, (c) 50 N, respectively.	137
Figure 6.9.(a) Worn surfaces of $\text{Mg}_2\text{Si}$ after sliding experiments at maximum load (50 N) and sliding velocity (7 m/s) and (b)–(d) elemental mappings of the worn surface of $\text{Mg}_2\text{Si}$ .	139
Figure 6.10.(a) Surfaces of disc wear track after sliding experiments at maximum load (50 N) and sliding velocity (7 m/s) and (b)–(d) elemental mappings of the worn surface of the disc.	140

## ABBREVIATION

---

TE	:	Thermoelectric
XRD	:	X-Ray Diffraction
DSC	:	Differential Scanning Calorimetry
FE-SEM	:	Field Emission Scanning Electron Microscope
HR-TEM	:	High-Resolution Transmission Electron Microscope
EDS	:	Energy Dispersive Spectroscopy
SPS	:	Spark Plasma Sintering
PF	:	Power Factor
R <sub>T</sub>	:	Thermal Shock Resistance

## SYMBOLS AND PHYSICAL CONSTANTS

---

Thermoelectric figure-of-merit	ZT
Seebeck coefficient	$\alpha$
Electrical conductivity	$\sigma$
Thermal conductivity	$\kappa$
Lattice thermal conductivity	$\kappa_L$
Electronic thermal conductivity	$\kappa_e$
Power factor	PF
Voltage difference	$\Delta V$
Temperature gradient	$\Delta T$
Heat	Q
Current	I
Resistivity	$\rho$
Conductivity	$\sigma$
Thermoelectric conversion efficiency	$\eta_{TE}$
Planck's constant	$h = 6.63 \times 10^{-34} \text{ m}^2 \text{ kg/s}$
Boltzmann constant	$k_B = 1.38 \times 10^{-23} \text{ m}^2 \text{ kg s}^{-2} \text{ K}^{-1}$
Mass of electron	$m_e = 9.1 \times 10^{-31} \text{ kg}$
Electron charge	$e = 1.6 \times 10^{-19} \text{ coulombs}$
Efficiency	$\eta$
Effective mass	$m^*$
Lorentz number	L
Absolute temperature	T
Hot-side temperature	$T_h$
Cold-side temperature	$T_c$
Carrier mobility	$\mu$
Carrier concentration	n
Specific heat at constant volume	$C_v$
Specific heat at constant pressure	$C_p$
Density	$\rho$
Diffusivity	D

Bragg angle	$\theta$
Hall coefficient	$R_H$
Wavelength	$\lambda$
Relaxation time	$\tau$
Load	$P$
Young's Modulus	$E$
Poisson's ratio	$\nu$
Coefficient of thermal expansion	$\delta$

# CHAPTER 1

Chapter 1 deals with the introduction of thermoelectrics and the research work carried in thermoelectric materials development. Basic concepts and understanding of thermoelectric properties, Seebeck coefficient, thermal and electrical conductivities have been described in this chapter. The main objectives of the current thesis have been described clearly, outlining the novelty and justification of current work.

## 1.1. Thermoelectric background

Thermoelectric generators (TEG), which convert waste-heat into electrical energy, are gaining momentum as a source of renewable energy [1–4]. A TEG produces electric power when there is a temperature gradient across the thermoelectric couple and is based on the Seebeck effect [1,4–6]. Several waste heat sources are available for TEG applications which include automotive exhaust (~ 500-900 K), engine and generator exhaust ( ~ 700 K ), industrial processes and furnaces (> 900 K), etc. However harnessing the heat from solar energy through TEG is an attractive green power generation technology, which addresses the environmental and fossil fuels depletion concerns [7–16]. The Infra-red spectrum of the solar energy density (which constitutes about 42% of the total solar energy density), could be exploited as a clean source of electricity generation, using TEGs [14]. Solar thermoelectric generators (STEGs) are green energy generators; they are using solid state material without any moving parts; they eliminate the use of traditional external systems such as steam boiler, turbine, and generators [7,17].

The TEG consists of *p-type* and *n-type* leg elements joined by metallic connectors in series electrically and thermally in parallel. This thermoelectric couple is in between a hot side (heat source) and a cold side (heat sink), thus creating a

temperature gradient, which is converted into useful electrical energy. The TEG conversion efficiency ( $\eta$ ) depends on the material's figure-of-merit. The figure-of-merit ( $ZT$ ) is a parameter determining the usefulness of any material as a thermoelectric element and is calculated by using the equation  $ZT = \alpha^2 \sigma / \kappa$ , where ' $\alpha$ ' is Seebeck coefficient, ' $\sigma$ ' is electrical conductivity, and ' $\kappa$ ' is thermal conductivity. To maximize the  $ZT$  and hence the  $\eta$ , the  $\alpha$  and  $\sigma$  must be a significantly large, and  $\kappa$  must be relatively small. Maximizing the  $ZT$  is a challenging task, as optimizing one of this physical parameter directly affects the other. Therefore, currently, there is an increasing emphasis on the development of thermoelectric materials with high  $ZT$ , as promising materials for thermoelectric applications. Various solar concentrators such as Linear Fresnel Lens, Parabolic Trough collector, Solar Tower, and Solar Dish-Stirling can generate temperature in the ranges of  $\sim 500$ - $1050$  K which could be harnessed for generation of electrical energy [7,17,18]. Therefore, the development of  $n$  and  $p$ -type thermoelectric materials with high  $ZT$  in the mid-to-high temperature ranges are the key issues for the development of a STEG harnessing heat from concentrating (500-1050 K) solar thermal power applications.

## 1.2. Thermoelectric efficiency

The overall performance of a thermoelectric device is characterized by the product of the Carnot thermodynamic efficiency and  $ZT$  [1,19,20]. The thermoelectric device optimum conversion efficiency is given by

$$\eta = \frac{T_{hot} - T_{cold}}{T_{hot}} \frac{\sqrt{1+ZT}}{\sqrt{1+ZT} + \frac{T_{cold}}{T_{hot}}} \frac{-1}{T_{hot}} \quad \text{----- (1.1)}$$

$$\eta_{max} = \eta_{Carnot} \cdot \eta_{TE\ Materials} \quad \text{----- (1.2)}$$

where  $T_{hot}$  is hot side, and  $T_{cold}$  is cold side temperature. Equation 1 provides the performance of thermoelectric materials of different  $ZT$  under various temperature

differences. In real thermoelectric devices, additional losses resulting from the inherent mechanism of all electrical devices such as interconnect contact resistances and Joule heating. The thermoelectric figure-of-merit is directly correlated to the efficiency of a device, and it is a dimensionless parameter for comparing the efficiency of thermoelectric conversion [21]. The value of  $ZT = 1$  is considerably good value at low-temperature applications, and enhancement to 2-3 at low-temperature could increase a thermoelectric conversion efficiency to  $\geq 20\%$ . The superior performance thermoelectric converters and thermo-electric devices with  $ZT \sim 3$  will compete with electrical generators/alternators efficiency. Comparison of efficiencies of two materials or systems is carried out by the materials'  $ZT$ . The best thermoelectric material will possess a high  $ZT$ . The  $ZT$  is mathematically defined as,

$$ZT = \frac{\alpha^2 \sigma}{\kappa} \quad \text{----- (1.3)}$$

where ' $\alpha$ ' is Seebeck coefficient, ' $\sigma$ ' is electrical conductivity, and ' $\kappa$ ' is thermal conductivity. A good thermoelectric material should have a high Seebeck coefficient value, a high electrical conductivity value, and low thermal conductivity value. The three physical properties of materials are interrelated, and optimization of one affects the other adversely. The three fundamental thermoelectric transport properties are explained in detail the following sessions.

### **1.3. Seebeck effect**

The Seebeck effect is a physical phenomenon of the materials, wherein a temperature difference between two dissimilar materials joined together at the ends produces a voltage difference between the ends. Thomas J Seebeck discovered the Seebeck effect in 1821 and described with a needle deflected by a closed loop formed by two dissimilar materials joined in two ends, with a temperature difference between the junction ends.

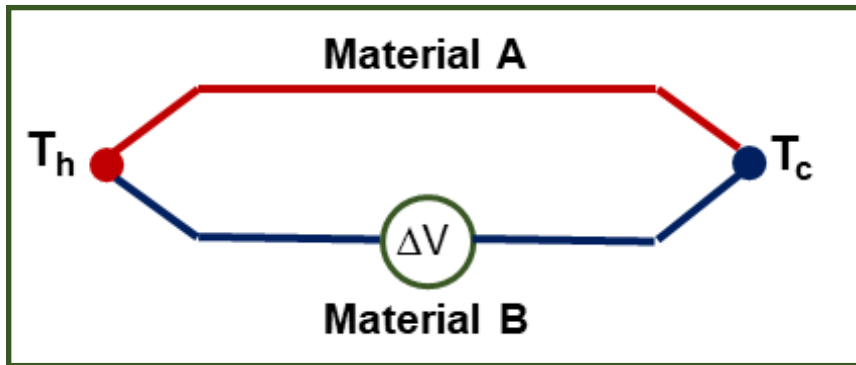


**Figure 1.1. Schematic diagram of Seebeck effect**

The Seebeck coefficient is originated from the electrons, which can transport both heat and electricity. The temperature gradient across the material causes a net movement of electrons from the hot end toward the cold end, thus producing an electric field. Seebeck coefficient value and its sign are associated with Fermi energy electron distribution. The Seebeck coefficient of the material mainly depends on the electronic structure, effective mass, and carrier concentration. When one end of the junction is heated, electrons/holes flow to the colder side. The electromotive force developed by the movement of these electrons/holes is called as Seebeck voltage. When the electrons move from the hot to cold end is called *n-type* material and the holes move from the cold to hot end is called *p-type* material. The ratio between the voltage difference generated with the temperature difference is called the Seebeck coefficient.

The Seebeck coefficient is described as the electromotive force (emf) generated per unit temperature difference and is a material property. The Seebeck coefficient is defined as mathematically,

$$\Delta V = \alpha \Delta T \quad \text{----- (1.4)}$$

$$\alpha = \frac{\Delta V}{\Delta T} \quad \text{----- (1.5)}$$



Metals have Seebeck coefficient values in the range, very low to approximately 80  $\mu\text{V/K}$ . The semiconductors have Seebeck coefficient values ranges from 50 to 1000  $\mu\text{V/K}$ . The Seebeck coefficient values required for good thermoelectric performance are greater than 200  $\mu\text{V/K}$ . Therefore, Semiconductors are the optimum choice of material for thermoelectric devices because of the high thermopower. At high temperatures, the Seebeck coefficients values become zero, for all the materials.

**Table 1.1.The Seebeck coefficient values of some common materials**

<b>Material</b>	<b>Seebeck coefficient (<math>\mu\text{V/K}</math>)</b>	<b>Material</b>	<b>Seebeck coefficient (<math>\mu\text{V/K}</math>)</b>
Antimony	47	Chromel- Alumel	40
Gold	6.5	Selenium	900
Silver	6.5	Tellurium	500
Lead	4	Silicon	440
Aluminium	3.5	Germanium	300

#### **1.4. Electrical conductivity**

The electrical conductivity of the materials causes the flow of electrons (electronic conductivity) or the movement of ions (ionic conductivity). The conduction caused by electrons are called *n*-type conduction and through holes is called *p*-type conduction. The electrical conductivity of metal is due to flow of electrons, and its value increases with the number of electrons. The ions flow causes the conduction is called ionic conduction. In ionic conduction, the defects in the crystal structure increase its conductivity. The unit of electrical conductivity is Siemens per meter. The precision

of the measurement of conductivity should be high for thermoelectrics, and it can be achieved by use of a four-probe technique.

$$\sigma = \frac{IL}{VA} \quad \text{----- (1.6)}$$

Metals have a very high electrical conductivity at room temperature, but exhibit linear decrease in conductivity with temperature rise. Semiconductors exhibits increase in conductivity or consistency with temperature rise. Doping in semiconductors becomes near-metallic properties but at high temperatures exhibits lower conductivity. In semiconducting materials, the conductivity could be controlled by addition of small atomic level impurities. This doping process alters the conductivity of the semiconducting materials via a change in carrier concentration density and charge carriers' mobility. The conductivity of semiconductors can be determined as,

$$\sigma = ne\mu \quad \text{----- (1.7)}$$

where 'n' is carrier concentration, 'e' is the electron charge and 'μ' is carrier mobility.

### 1.5. Thermal conductivity

The thermal conductivity is the ability to transfer the heat energy. In the classical approach, the thermal conductivity of solid is defined by Fourier law of conduction, the heat energy transferred through the surface area, with respect to the temperature difference between two surfaces. The unit of thermal conductivity is W/mK.

$$Q = -\kappa A \frac{dT}{dx} \quad \text{----- (1.8)}$$

where, 'Q' is the heat energy transferred, 'κ' is the thermal conductivity, 'A' is the cross-sectional area, and 'dT/dx' is the temperature gradient. The thermal conductivity

value of a solid would be three to four orders of magnitude higher than that of gas. The tendency of high thermal conductivity in solids is due to large differences in intermolecular spacing between the two states. Metallic solids conduct the heat via electrons, whereas the Non-metallic solids conduct the heat via lattice vibrations. The heat transfer is often described by the term phonons transport. Metals are good thermal conductors than non-metals due to the free electrons participation in the transfer of heat. Normally, in metals, heat conduction is dominated by electrons and the lattice vibration is almost negligible. Both electron and lattice vibration conduction mechanism is responsible in case of semiconductors. The thermal conductivity will decrease with increasing temperature in metals. By introduction of defects, alloying, cold working will further reduce the thermal conductivity of materials. The ratio of the thermal conductivity to the heat capacity described as thermal diffusivity is an essential property in thermoelectric materials.

$$\alpha = \frac{\kappa}{\rho c_p} \quad \text{----- (1.9)}$$

Thermal diffusivity ( $\alpha$ ) is described as the ability of material, to conduct heat energy relative to its ability to store the energy. Materials of high thermal diffusivity value will impart quick response to changes in their thermal environment conditions, while materials of low thermal diffusivity value will give a more sluggish respond, taking a long time to reach a thermal equilibrium condition. The thermal conductivity ( $\kappa$ ) in contrast, is the sum of the electronic ( $\kappa_{el}$ ) and lattice ( $\kappa_{ph}$ ) contributions were given by the Wiedemann-Franz law

$$\kappa = \kappa_{el} + \kappa_{ph} \quad \text{-----(1.10)}$$

$$\kappa_{el} = \sigma LT = ne\mu LT \quad \text{----- (1.11)}$$

$$\kappa_{ph} = \frac{1}{3} C_v v_s \lambda_{ph} \quad \text{----- (1.12)}$$

where, ‘ $\sigma$ ’ is the electrical conductivity, ‘ $L$ ’ is the Lorenz number, ‘ $T$ ’ is the temperature, ‘ $C_v$ ’ is the specific heat, ‘ $v_s$ ’ is the sound velocity and ‘ $\lambda_{ph}$ ’ is the phonon mean free path.  $\kappa_{ph}$  is independent of charge carriers, but  $\kappa_{el}$  increases with an increase in the carrier concentration. It can be observed that total thermal conductivity value increases with electrical conductivity (electronic component) and hence reduce the lattice conductivity is always the best choice for improvement of figure-of-merit ( $ZT$ ) of thermoelectric materials.

**Table 1.2. Thermal conductivity values of some common materials**

<b>Material</b>	<b>Thermal conductivity (W/mK)</b>	<b>Material</b>	<b>Thermal conductivity (W/mK)</b>
Diamond	1300	Marble	2.8
Silver	420	Fused Silica	1.4
Copper	400	Gypsum	0.51
Aluminium	237	Polyethylene	0.35
Iron	76	Wood	0.13

## 1.6. Energy Band Gap

The energy gap ( $E_g$ ) is a measure of the energy which must be imparted to an electron in the valence band to place it in the conduction band. In conduction band,

electrons are freely mobile and therefore capable of carrying current. The extent of the population of energy levels lying within the conduction band is measured by the position of Fermi level ( $E_F$ ). When the Fermi level coincides with the lower edge of the conduction band indicates the degeneracy and degeneracy show the near metallic like properties in semiconductors. Fermi level lies middle portion of the energy gap (between the valence and the conduction band) indicates insulator and near conduction band indicates n-type and near valence band indicates p-type semiconductor. The Fermi level is given by

$$E_F = kT \ln \left( \frac{nh^3}{2(2\pi m_e kT)^{\frac{3}{2}}} \right) \text{ ----- (1.13)}$$

where ‘ $k$ ’ is Boltzmann’s constant, ‘ $T$ ’ is the absolute temperature, ‘ $n$ ’ is the number of charge carriers, ‘ $h$ ’ is Planck’s constant and ‘ $m_e$ ’ is the effective mass of the carriers.

### 1.7. Carrier concentration

In conduction band, the number of electrons per unit volume or in the valence band, the number of holes per unit volume is called carrier concentration. The number of electrons per unit volume in the conduction band is called electron-carrier concentration, and the same time the number of holes per unit volume is called as hole-carrier concentration. In metals, a large number of carriers available for conduction, for example,  $n \geq 10^{22}$  carriers/cm<sup>3</sup>, exhibits high electrical conductivity value in the order of  $10^8$  S/m. In semiconductors, the electrical conductivity occurs through the contributions of both holes and electrons. Also, the carriers (electrons/holes) would be thermally excited across a gap for conduction to occur.

$$\sigma = C \exp \left( -\frac{E_g}{kT} \right) \text{ ----- (1.14)}$$

where, ‘ $C$ ’ is material constant, ‘ $E_g$ ’ is the band gap, ‘ $k$ ’ is Boltzmann’s constant, ‘ $T$ ’ is the absolute temperature. The electrical conductivity values of semiconducting materials are ranges between  $10^{-2}$  and  $10^6$  S/m. The carrier density not only increases the electrical conductivity, influences on the thermal conductivity. Thus, the increase in the carrier concentration of thermoelectric material increases the electronic portion of the thermal conductivity. As a result, an increase in total thermal conductivity reduces the figure-of-merit value. Heavily doped thermoelectric materials are naturally best thermoelectric characteristics and with a carrier concentration of  $10^{19}$  to  $10^{21}$  carriers/cm<sup>3</sup>.

### 1.8. Mobility

The mobility is a measure of the movement of charge carriers (electrons/holes) by an electric field. In other words, the electron mobility indicates how quickly an electron can move through a material when pulled by an electric field. The mobility of the semiconductor is directly proportional to mean free path of the carrier and inversely proportional to the mass of the charge carrier. The more frequent collisions will shorter the mean free path which causes the small mobility of charge carrier. The conductivity of the material is directly related to the mobility, which depends on the density of charge carriers, temperature, and electric field strength. The mobility of a charge carrier is given by

$$\mu = \frac{4}{3} \frac{el}{(2\pi mkT)^{\frac{1}{2}}} \text{----- (1.15)}$$

where, ‘ $l$ ’ is the mean free path, ‘ $k$ ’ is Boltzmann’s constant, ‘ $T$ ’ is the absolute temperature, ‘ $m$ ’ is an effective mass of the carriers. The unit of electron mobility is cm<sup>2</sup>/(V·s). The mobility value of some materials is carbon nanotubes  $\sim 1 \times 10^5$  cm<sup>2</sup>/(V·s)

graphene  $\sim 2 \times 10^5 \text{ cm}^2/(\text{V}\cdot\text{s})$ , Crystalline Silicon  $\sim 1.4 \times 10^3 \text{ cm}^2/(\text{V}\cdot\text{s})$ , Gallium Nitride  $\sim 3 \times 10^2 \text{ cm}^2/(\text{V}\cdot\text{s})$  Organic semiconductors  $\sim 50 \text{ cm}^2/(\text{V}\cdot\text{s})$ .

### 1.9. Figure-of-Merit (ZT)

A.F. Ioffe developed the concept of figure-of-merit (ZT) in 1949, and it is a determining parameter of the usefulness of any material as a thermoelectric element. The dimensionless figure-of-merit for a single material is calculated by using

$$ZT = \frac{\alpha^2 \sigma}{\kappa} \quad \text{----- (1.16)}$$

where ‘ $\alpha$ ’ is Seebeck coefficient, ‘ $\sigma$ ’ is electrical conductivity, and ‘ $\kappa$ ’ is thermal conductivity. Materials with high thermoelectric figure-of-merit are heavily doped degenerated semiconductors.

To maximize a figure-of-merit, Seebeck coefficient and electrical conductivity values should be high and thermal conductivity value should be small. The maximizing figure-of-merit is a challenging task, as optimizing one of this physical parameter affects the other. To achieve higher efficiency, improving the figure of merit is the viable solution. In a broad context, the figure of merit is influenced by both electron transport and heat transport as well as the coupling of these two within a material of interest. The maximum figure-of-merit can be determined from the mobility ( $\mu$ ) and effective mass of electrons/holes ( $m$ ) and lattice thermal conductivity ( $\kappa_{ph}$ ):

$$ZT = \frac{\mu m^{3/2}}{\kappa_{ph}} \quad \text{----- (1.17)}$$

The high-performance thermoelectric system is possible through high figure-of-merit material development to broaden the device applications. The device efficiency

depends on the  $ZT$  of the material parameter when there are no external system losses such as thermal and electrical contact resistances, load and thermal interfaces [21]. The figure-of-merit values for the commonly available thermoelectric materials are;  $\text{Bi}_2\text{Te}_3 \sim 1.1$  at 400 K [22] ,  $\text{PbTe} \sim 2$  at 650 K [23–25] and  $\text{SiGe} 1.5$  at 1273 K [26]. The maximum reported  $ZT$  values of the materials are  $\text{AgPb}_m\text{SbTe}_{2+m} \sim 2.2$  at 800 K [27] ,  $\text{SnSe} \sim 2$  at 723 K [21] and  $\text{Cu}_2\text{Se} \sim 2.1$  at 973 K [28].

### **1.10. Strategies to maximize the thermoelectric performance**

From the fundamental explanations above, an efficient thermoelectric material should possess a high electric conductivity with a high Seebeck coefficient and have a low thermal conductivity. The electric conductivity and Seebeck coefficient are determined by the electronic properties of the thermoelectric material and is known as power factor. Thermal conductivity is divided into two parts, electron ( $\kappa_{el}$ ) and lattice ( $\kappa_L$ ) thermal conductivities.

Several strategies have been used to enhance the thermoelectric properties of thermoelectric materials, and few of them employed in the present study.

- Single & multiple doping
- Nanocrystalline structures
- Grain boundary engineering.

The increase in electrical conductivity is associated with an increase in the thermal conductivity and decreases in Seebeck coefficient, and hence optimizing  $ZT$  becomes a challenging task. The power factor could be increased by varying the concentration of carriers in the material, but decreasing thermal conductivity becomes more challenging, especially for lattice thermal conductivity. The lattice thermal conductivity mostly depends on the materials' crystal structure, rigidity, atomic masses, and other characteristics of the lattice. The high value of Seebeck coefficient and low thermal



conductivity value without sacrificing electrical conductivity are the requirements of efficient thermoelectric materials. Semiconductors meet these specifications better than metals. In general, vibrating independently scattering phonons without affecting significantly the electron transport is the methodology used to reduce thermal conductivity without affecting electrical conductivity. It has been shown in recent years that the short-range disorder caused by alloying acts as an efficient scattering of phonons thereby reducing the phonon thermal conductivity without affecting significantly electrical conductivity [10]. The nanocrystalline structures open the door to reduce the lattice thermal conductivity without affecting the electrical conductivity [29]. By using advanced materials processing technologies and development, it has been possible to design the more efficient thermoelectric materials.

Melt spinning employing rapid solidification is one of the best material processing techniques, which could able to produce the nanocrystallite boundaries, at different length scales [30,31]. The nanocrystallite grain boundaries scatter a broad spectrum of low and medium wavelength region phonons and therefore exhibiting a low lattice thermal conductivity [32]. The nanocrystalline microstructure with the control of chemical composition, introduced by melt spinning- rapid solidification technique could direct to a significant improvement in thermoelectric properties.

### **1.11. Thermoelectric materials for low-temperature applications (< 500 K)**

Low temperature (< 500 K) thermoelectric materials have more attention for small power generation and cooling modules. The Bismuth telluride and its alloys are dominating materials in low-temperature thermoelectric applications since 1950, due to its high figure-of-merit.  $\text{Bi}_2\text{Te}_3$  shows optimum Seebeck coefficient  $\sim 280 \mu\text{V/K}$  and maximum figure-of-merit ( $ZT$ )  $\sim 1.2$  at 400 K [22].  $\text{Bi}_2\text{Te}_3$  have layered structures with heavy atoms, offers very low thermal conductivity. The narrow band gap of 0.15 eV

exhibits a high electrical conductivity, and the large band degeneracy is also beneficial to produce a high power factor ( $\alpha^2\sigma$ ) value [33,34]. Because of these advantages,  $\text{Bi}_2\text{Te}_3$  and its alloys have been used for a wide range of low-temperature thermoelectric applications.  $\text{Bi}_2\text{Te}_3$  exhibits the delamination tendency due to its rhombohedral structure and weak Van der Waals force. The fabrication of  $\text{Bi}_2\text{Te}_3$  involves extra care due to its softness and delamination properties. Further, the high cost of tellurium and toxicity, compel the use of a substitute for  $\text{Bi}_2\text{Te}_3$  based alloys in the low-temperature ranges. Bismuth selenide ( $\text{Bi}_2\text{Se}_3$ ) is an n-type semiconductor material, exhibits a very small band gap of 0.35 eV.  $\text{Bi}_2\text{Se}_3$  has a layered structure comprising of five layers of atoms in a hexagonal plane and exhibiting a rhombohedral lattice.  $\text{Bi}_2\text{Se}_3$  shows optimum Seebeck coefficient  $\sim 100 \mu\text{V/K}$  and maximum  $ZT \sim 0.7$  at 400 K [35]. Antimony telluride ( $\text{Sb}_2\text{Te}_3$ ) is a p-type semiconductor for low-temperature applications, shows optimum Seebeck coefficient  $\sim 150 \mu\text{V/K}$  and maximum  $ZT \sim 0.95$  at 420 K [36]. The  $\alpha$ -MgAgSb is the earth abundant, non-toxic low-temperature thermoelectric material, exhibits  $ZT \sim 1$  at 500 K [37].  $\text{CsBi}_4\text{Te}_6$  is another promising thermoelectric material for low-temperature applications, having a very small band gap of 0.1 eV.  $\text{CsBi}_4\text{Te}_6$  has shown a maximum  $ZT \sim 0.82$  at 225 K [38]. Te/Sb/Ge/Ag (TAGS) materials are efficient thermoelectric material, exhibits very low thermal conductivity and maximum  $ZT \sim 1.6$  at 600 K [39]. It is indicating that the materials used in the low-temperature range are scarce, non-toxic and expensive, which imparts the high cost on thermoelectric devices.

### **1.12. Thermoelectric materials for mid temperature applications (500 -900 K)**

Mid-range temperature (500 – 900 K) materials are suitable for waste heat recovery from automotive, power plant, and industrial furnaces. PbTe is a common thermoelectric material for mid temperature range, showing the maximum  $ZT$  of about

2.2 at 900 K [40], but the constituent elements are expensive (Te) and toxic (Pb). Half-Heusler (HH) alloys have more attention for mid temperature applications due to its non-toxic and thermal stability. (Hf, Zr) NiSn alloys are showing the maximum  $ZT \sim 1.3$  at 850 K embedding of nanoparticles [41]. The materials of choice for mid temperature applications are a CoSb<sub>3</sub> family of skutterudites, showing the maximum  $ZT \sim 0.8$  at 700 K, however, the presence of rare-earth leads to the limitations of cost optimization. Zn<sub>4</sub>Sb<sub>3</sub> shows a maximum  $ZT \sim 1.3$  at 670 K [42], and Cu<sub>2</sub>Se shows a high  $ZT$  of 2.1 [28] at 973 K, are the good mid temperature thermoelectric materials, but poor stability restricts its applications.

Silicides have proven to be the best candidate for an excellent thermoelectric generation. Among chromium silicides (CrSi<sub>2</sub>) are the family of transition metal silicides, potential materials for mid temperature applications due to their high melting point and chemical stability. CrSi<sub>2</sub> has an energy gap of 0.30 eV and shows a maximum  $ZT$  of about 0.18 at 700 K. Magnesium has a very low density, which results in high conversion efficiency per unit mass compared to other thermoelectric materials. The specific thermoelectric conversion efficiency of magnesium silicide and the earth abundance of constituent elements, add to the advantages of Mg<sub>2</sub>Si over other compounds and prefer it as a hopeful thermoelectric material [43–45]. Higher manganese silicides (HMS) are the silicides family of *p-type* thermoelectric materials in thermoelectric devices [46–56]. Higher manganese silicides are unique thermoelectric materials for low cost and non-toxic thermoelectric power generation using chemically and thermally stable materials for the mid-temperature TEG applications.

### **1.13. Thermoelectric materials for high-temperature applications (> 900 K)**

High temperature (> 900 K) materials are suitable for niche applications, generating power for deep space missions, where excellent reliability and durability of

materials performance is essential. At higher temperatures, material decomposition and vaporization possibilities are very high, which make thermoelectric performance degradation and failure. Silicon is one of the excellent material for high-temperature thermoelectric applications, due to its nontoxic, inexpensive, and naturally abundant. Silicon shows good electrical properties ( $\alpha^2\sigma$ ), but high lattice thermal conductivity leads to low  $ZT \sim 0.23$  at 1033 K [57]. Lanthanum telluride is an n-type semiconductor having a band gap 0.9, shows a maximum  $ZT \sim 1.1$  at 1200 K [58].

Oxide-based materials are potential thermoelectric materials for high-temperature application, due to their high thermal and chemical stability. Strontium titanate ( $\text{SrTiO}_3$ ) oxides are cubic structure high-temperature thermoelectric materials exhibits  $ZT \sim 0.35$  at 1000 K [58]. Zinc oxide provides a wide band gap, and ZnO semiconductor exhibits a band gap of 3.2 to 3.5 eV and shows a  $ZT \sim 0.65$  at 1273 K [58]. Layered cobalt oxides have much attraction on metal oxides and exhibit  $ZT \sim 0.7$  at 1000 K [59].  $\text{Yb}_{14}\text{MnSb}_{11}$  exhibits a high figure of merit ( $ZT$ )  $\sim 1$  at 1200 K [60], with low thermal conductivity value ( 0.7 to 0.9 W/mK, for the temperature ranges 300 to 1275 K).  $\text{CaMnO}_3$  has been promoted as a hopeful thermoelectric material because of high Seebeck coefficient value with low thermal conductivity.  $\text{CaMnO}_3$  is a n-type semiconductor shows a  $ZT \sim 0.13$  at 973 K [61]. Si-Ge alloys show high thermoelectric performance at high temperatures and extensively used in power generation applications in space missions. SiGe alloys are the most widely used materials for thermoelectric power generation, due to their high  $ZT$  for high-temperature range ( $>1273$  K). Si-Ge alloy (n-type) exhibits  $ZT \sim 1.5$  [26], and *p-type* Si-Ge alloy exhibits  $ZT \sim 1.2$  at 1173 K [62], are a best suitable combination for high-temperature operations.

## **1.14. Applications of thermoelectrics**

### **1.14.1. Space applications**

Space exploration missions need a reliable electric power source to the proper functioning of their instruments, spares, and accessories. Radioisotope Thermoelectric Generators (RTGs), offer power for electronic components associated with spacecraft by converting the heat generation of plutonium-238 (Pu-238) into electrical power [63]. RTGs show as a highly reliable, safe power option for future space missions. Thermoelectric elements used in RTGs excels a service time of ~30 years, and a not a single thermoelectric leg failed to produce electric power. In an RTG, plutonium-238 heats the hot-side junctions while the other junction keeping the space environment. Thermoelectric materials commonly used in RTGs are highly effective, costlier thermoelectric materials like bismuth telluride (BiTe), lead telluride (PbTe), TAGS, and silicon germanium (SiGe). The high efficient thermoelectric materials convert the heat produced by the Pu-238 fuel into electrical power by using Seebeck effect employing single or segmented or combination of both design modules. Several spacecraft components utilize the output power generated by TEGs. The most important space exploration mission applications of thermoelectric generators are Applo, Voyager, Jupiter-Cassini, Mars-Curiosity.

### **1.14.2. Automotive applications**

Thermoelectric generators (TEGs) improve the fuel efficiency ~ 5% by recovering the waste heat coming out from exhaust gas in automobiles. The energy generated from TEGs from waste heat provide the required amount of power for displays, sensors, and other electronic accessories. The BMW vehicle experimented at a speed of 130 km/h and produced a peak power of 200 watts [64]. Further modifications and installation in the radiator of BMW car, the thermoelectric generator produces peak

power 600 watts. BMW put efforts to generate 1,000 watts (or 1 kilowatt), to make a thermoelectric generator technology economical. The peak power generation of 325 watts would be expected with an exhaust gas mass flow rate of 56.5 kg/hr with a temperature of  $\sim 900$  K. The thermal efficiency of the TEG at highway speeds is  $\sim 5.7\%$  with hot and cold junction temperatures of  $\sim 550$  K and 373 K respectively. Radiator waste-heat conversion using TEGs could be practical, even with the low-temperature difference. The main reasons are, liquid to solid heat transfer is efficient than gas to solid, and lower system weight benefit due to an integrated heat exchanger (called as a radiator) attached to the vehicle.

#### **1.14.3. Industrial waste heat applications**

Manufacturing industrial processes are discharging one-third of its energy consumed as waste heat. Industrial waste heat spread over the temperature range is from  $250^{\circ}\text{C} - 700^{\circ}\text{C}$  best suitable for developing mid-temperature range thermoelectric device applications. Waste heat recovery opportunities mostly available in chemical industries (process heaters, reactors, and fired boilers), cement industries (lime kilns, rotary cement kilns) and steel plants (melting & heating furnaces) and thermal power plants (boilers, turbines & reactors).

#### **1.14.4. Marine applications**

The heat engines used in marine applications delivers considerable amount heat energy as waste heat except to drive a ship in the water. Nuclear power-driven ships become popular for submarines and other underwater marine applications. The temperature difference between the heat source (engine side) and the cold side sink (the water) is beneficial and well suited for thermoelectric conversion. The electricity produced using thermoelectric converters TEGs convert this temperature difference into electricity to power the hotel load, recharge batteries, or other applications.

Thermoelectric technology could increase the efficiency of the whole system by reducing the amount of by-product waste heat of IC engines or nuclear power.

#### **1.14.5. Aerospace applications**

The customer needs & satisfaction is the prime objective in commercial aerospace applications nowadays, which increase the electricity demand for charging TV, internet, mobile phone, etc. Temperature differences are substantial in jet engines exhaust to the ambient atmosphere that can be converted into electric power using thermoelectric generators.

#### **1.14.6. Wearables**

Wearable technologies are attracting nowadays due to its flexible and compact. The bismuth-telluride based flexible thermoelectric devices could generate the electricity in the micro to milliwatts using body heat, which is adequate to power the device [65]. The Seiko and Citizen Company manufactured the thermoelectric powered wristwatch. The watch is powered by body heat converted to (22  $\mu$ W) electric power by the thin thermoelectric material elements. Further, human body sensing could become more widespread applications with flexible thermoelectric technology such as wristbands, clothing, athletic apparel that monitor heart rate, body temperature, etc.

#### **1.14.7. Consumer Products**

Thermoelectric technology will be useful for several consumer applications like powering the mobile phones, consumer electronics when cooking. The small thermoelectric devices would helpful for the environments where temperature differentials exist; suitable for low power applications such as wireless sensors network, mobile devices, etc.

### 1.14.8. Solar application of thermoelectrics

Solar energy is a renewable and ultimate clean energy and its thermal energy part can be utilized for generation of electrical energy using a TEG. The Infra-red spectrum of the solar energy density (which constitutes about 42% of the total solar energy density), could be exploited as a clean source of electricity generation, using thermoelectric materials. Approximately six thousand million GWh per year solar energy potential is predicted in Indian geographical conditions, out of which the renewable energy usage is only ~ 5 % of the total energy consumption in India.

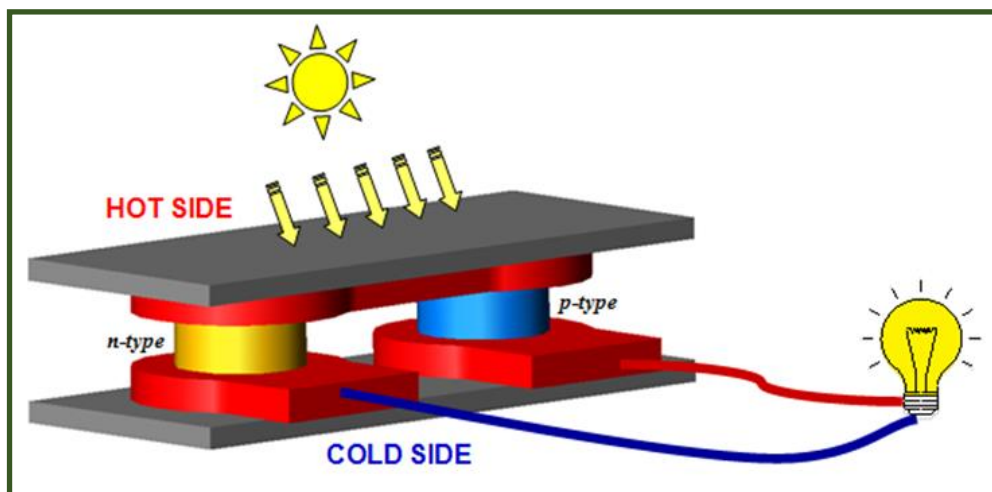


**Figure 1.2. Schematic of Solar Thermoelectric power conversion**

Photovoltaics technology is being used a broad spectrum of applications worldwide and being studied extensively till now. The photovoltaics is dominating in non-concentrating solar energy conversion systems; however, the temperature increase causes the photovoltaic efficiency low, on the other hand, it increases the efficiency of thermoelectric conversion. Therefore, power generation using thermoelectric



technology is gaining momentum in concentrated solar thermal systems and the hot topic of research in a recent couple of years. The direct solar thermoelectric power generation technology eliminates the conventional intermediate mechanical conversion processes like a steam generator, turbine, and electric generators. Solar thermoelectric generators generate electricity by harnessing the energy of sunlight radiation (infra-red spectrum) like photovoltaic systems.

The direct solar thermoelectric power generation has the many following advantages.

- Solid-state and scalable
- Stable, vibration free, noiseless operation
- Durability and consistency
- Demonstrated performance of lengthy service in hostile environment applications

The solar thermal power could be exploited with several collector options on hot side operating temperatures of thermoelectric generators.

- Linear Fresnel Lens (LFL) ~ 663 K
- Parabolic Trough Collector (PTC) ~ 623 – 823 K
- Solar Tower (ST) ~ 523 – 838 K
- Solar Dish-Stirling (SDS) ~ 823 – 1023 K

Applications of the solar thermoelectric generator are attractive in both the ways. STEGs generate electrical energy using the flat-panel solar thermal collector (Figure 1.2) or concentrated solar power collector (Figure 1.3). Solar thermoelectric conversion, the infrared (IR) region of the solar spectrum provides the energy for the hot side of TEG, reported by Tritt et al. [14]. Telkes [10] reported solar thermoelectric generator with an efficiency of 0.6% using flat-panel optical concentration in 1954. The peak efficiency of 4.6 % flat-panel solar thermoelectric generator has demonstrated by

Kraemer et al. [13]. A highly solar-absorbing surface is utilized to create a large temperature gradient, instead of using an optical concentrator. The solar-absorbing surface converts the solar radiation energy into heat and concentrates it onto the hot-side of the thermoelectric elements. The cost of the system is reduced drastically because of elimination of solar flat-panel tracking system. Kraemer et al. [7] reported the solar TEGs with an efficiency of 7.4%. They also reported the performance improvement is due to the use of segmented thermoelectric design, vacuum operated high-temperature solar absorber and combining optical and thermal concentration.

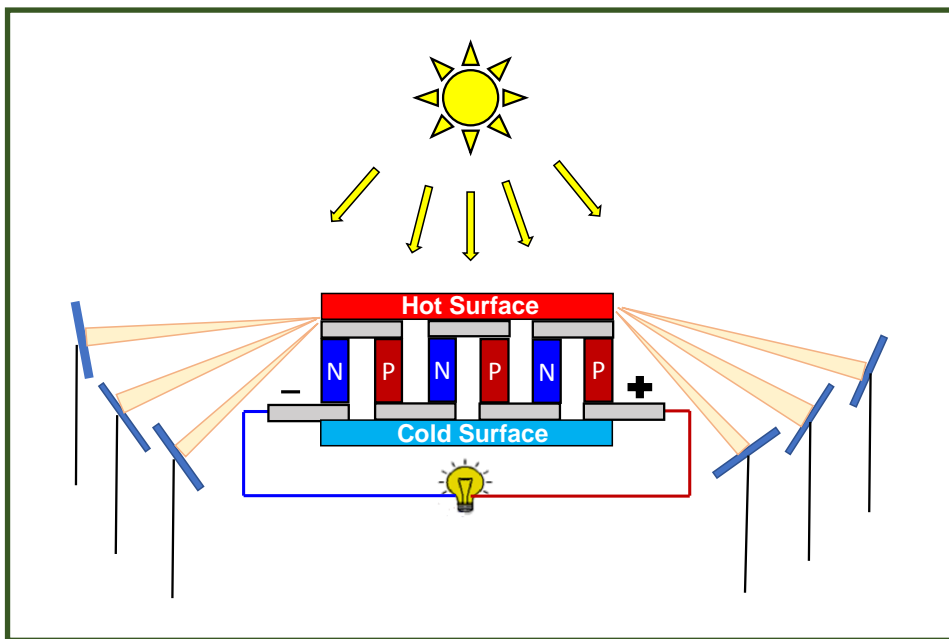


**Figure 1.3. Schematic of Concentrated Solar Power Thermoelectric conversion**

Li et al. [66] developed a prototype concentrated thermoelectric generator and showed the highest possible efficiency of 14.1%. The low efficiency of the solar thermoelectric generator is not an only parameter to determine the technological advancement of thermoelectrics. The other factors, low operating, maintenance costs, high-reliability and long-service lifetime (~ 20 years) would help to make the potential

of a thermoelectric generator for solar power generation applications. Conventional solar thermal power generation involves the water circulation pumps, steam generator, turbine, and condensers, etc. The capital and maintenance cost of these components contributes the significant part of power generation cost. Solar thermoelectric generators (STEGs) provide the direct solid-state energy conversion, which eliminates the mechanical components like water circulation pumps, steam generator, turbine and condensers from the power generation plants. STEG has the advantage to function both the concentrating and non-concentrating solar power systems (Figure.1.4). Concentrated solar irradiation from the sun offers numerous benefits to convert heat into electricity by achieving high-temperature difference between the hot and cold side of the STEG. The maximum temperature (350 K) obtained by the non-concentrating system (Figure 1.4(a)), is the limitation of STEG conversion efficiency. At the same time, the concentrating system (Figure 1.4(b&c)) could reach up to 1000 K using Linear Fresnel Lens, Parabolic, and Solar dish, and would benefit to harness the solar energy efficiently employing thermoelectric generators.

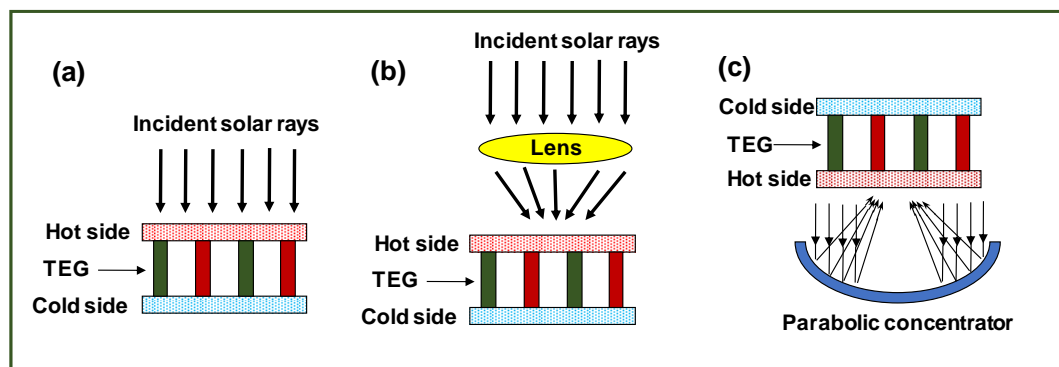


**Figure 1.4. Thermoelectric generator used in different solar thermal non-concentrating(a) and concentrating linear fresnel lens(b), Parabolic power(c) systems.**

The various thermoelectric materials used in solar thermoelectric generators are listed in Table.1.3, based on the operating temperature range and thermoelectric figure-of-

merit. The STEGs demonstrated with most established Bi-Te based alloys, which convert solar heat into electric power at an operating temperature  $\sim 473$  K [13]. However, the materials used for solar energy conversion are enclosed in an evacuated vacuum glass enclosure. The preliminary studies on  $\text{Bi}_2\text{Te}_3$  material covered with CNT sheets are made to utilize the combined thermoelectric property and absorption property of STEG, but temperature ranges are limited to 10 K [15].

**Table 1.3. Materials and temperature ranges deployed in solar thermoelectric generation systems**

<b>Material used</b>	<b>Temperature range /difference (K)</b>	<b>Maximum figure-of-merit (ZT)</b>	<b>system</b>	<b>Ref.</b>
$\text{Bi}_2\text{Te}_3$	475	$\sim 1$	Concentrating	[13]
$\text{Bi}_2\text{Te}_3$	300	$\sim 0.54$	Non-concentrating	[15]
$\text{Bi}_2\text{Te}_3/\text{SKU}$	800	$\sim 1$	Concentrating	[7]
Oxides	800	$\sim 0.08$	Concentrating	[17]

Segmented thermoelectric legs using Skutterudites and  $\text{Bi}_2\text{Te}_3$  are fabricated for demonstrating the high-temperature STEGs ( $\sim 800$  K) by Kraemer et al. [7]. But, maintain a stoichiometric composition and chemical stability at high temperature of these materials remains challenging. Despite extensive research carried out on solar thermoelectric energy conversion with conventional bulk thermoelectric materials, (Table.1), but are not yet commercialized. The reasons are, the rise in the cost and scarcity of tellurium like elements put a curtain on solar thermoelectric technology competition with solar photovoltaics, etc. The degradation of thermoelectric properties

with the cyclic thermal loading of these materials is the principal concern, an especially crucial parameter for solar thermal power conversion. The most of the thermoelectric materials used in STEG contain toxic elements which add another dimension and other handling issues, from an environmental point of view. The literature shows lack of research, necessity, and demand for the development of thermoelectric materials for concentrating solar thermal range (500–800 K) (Table 1). Also, the parameters that control the efficiency of thermoelectric materials ( $ZT$ ), like Seebeck coefficient, electrical conductivity, and thermal conductivity, will be enhanced, to make STEG be viable futuristic efficient power generation technologies.

The cost of solar thermoelectric energy conversion is directly impediment by its low conversion efficiency and the requirement of costly materials. The development of efficient thermoelectric materials (high figure-of-merit) combined with processing methods is first and foremost technical need to enhance the solar thermoelectric energy conversion.  $Mg_2Si$ - $MnSi_{1.73}$  materials have a high potential in solar thermoelectric conversion due to their cost-effectiveness, earth abundance, and non-toxicity. The thermal stability of these materials in the operating temperature of the concentrated solar thermal region (~500-800 K) is also superior to other conventional thermoelectric materials. Thus, the  $Mg_2Si$ (n-type)- $MnSi_{1.73}$ (p-type) combination is promising for STEGs, for the temperature of ~ 500-800 K (concentrating solar thermal region), due to their Seebeck coefficient and coefficient of thermal expansion compatibility and low density leading to very high conversion efficiency per unit mass. Therefore,  $Mg_2Si$ - $MnSi_{1.73}$  usage in solar thermoelectric generators provides the high impact on low cost, efficient solar conversion technology.

### 1.15. Motivation and objectives

Thermoelectric devices, based on Seebeck effect, are anticipated to play a vital role in realizing the energy demand of the future. An approach could be to harness the infra-red spectrum of solar energy, which constitutes about 42% of the total solar energy density, using TEGs, as a clean source of electricity generation employing thermoelectric materials. As TEGs are stable devices with no moving parts, they are noiseless, durable and scalable, realizing them perfect for renewable energy applications. However, the solar thermoelectric generators (both concentrating  $\sim 500$ - $1000$  K and non-concentrating  $< 500$  K), can only compete with other renewable energy technologies like photovoltaics, if the material and manufacturing costs of the TEG can be significantly reduced. Therefore, the growth of solar thermoelectric technologies is currently concentrating on the production of competent thermoelectric materials that are earth crust abundant, non-toxic and also thermally stable at the TEG operating temperatures.

Silicides have proven to be one of the best candidates for thermoelectric power generation owing to its enhanced thermoelectric figure-of-merit, thermal stability, and the earth-abundance and non-toxic of its constituent elements.  $\text{Mg}_2\text{Si}$  (*n-type*) and  $\text{MnSi}_{1.73}$  (*p-type*) are the ideal combinations for developing a cost-effective and efficient thermoelectric device due to their thermal stability, Seebeck coefficient compatibility, and low density. Silicide based materials have been proposed as useful thermoelectric material primarily because there is the possibility of producing compatible n & p-type thermoelectric elements by suitable doping for thermoelectric devices operating in the intermediate temperature range. Further, the presently used devices made from bismuth-telluride based materials shows the variations in performance, driven by long-term exposure to environment and temperatures cycling.

Magnesium and Manganese based silicides are one of the cheapest compared to the existing conventional thermoelectric materials. Silicides are more thermally stable and abundant in the earth crust. Various strategies and methods have been employed to enhance the thermoelectric efficiency of silicide-based materials. But, the reported values are complex and also adopting different methodologies to synthesize the silicide-based material. Further, in most of these studies, the electrical conductivity increases quite substantially on doping, but the corresponding change in the thermal conductivity is quite high. The reported studies suggest that the enhancement of figure-of-merit in silicide-based systems follows not from the material's band structure. The increase in the figure-of-merit probably originated at the grain boundaries or may pertain to metallic nano-inclusions.

The controlling of the microstructure is the one way of optimizing thermoelectric performance. From a materials point of view, crystallographic texture and grain boundaries arrangements are to be studied in detail to improve the thermoelectric efficiency. Finally, it is observed that there is no clear-cut way or approach to evaluating the thermoelectric properties of materials. Apart from thermoelectric properties, to warrant the structural reliability of the thermoelectric material, the mechanical performance of the material is similarly essential to circumvent sudden failure of their thermoelectric devices during actual working conditions. Also, the relationships between mechanical properties and thermoelectric properties and microstructure features are highly expected, which have not been studied thus far. Thus, in view of the justification from the discussion here, the objectives of the current work are listed below.

## Objectives of thesis

- Synthesize the low-cost, non-toxic, high efficient *n-type*  $\text{Mg}_2\text{Si}$  and *p-type*  $\text{MnSi}_{1.73}$  silicide-based thermoelectric materials, to realize the feasibility of cost-effective and efficient solar-thermoelectric conversion in the high-temperature range (500 – 800 K).
- Synthesis of thermally stable *n-type*  $\text{Mg}_2\text{Si}$  and *p-type*  $\text{MnSi}_{1.73}$  silicide-based thermoelectric material with high  $ZT$  and to understand the role of processing conditions to achieve an efficient silicide-based thermoelectric material.
- Characterize the microstructural and structural properties (XRD, FESEM, EDS, and HRTEM) of the synthesized *n* & *p-type* material and establish Structure-Processing-Property correlation.
- Mechanical properties of the silicide-based thermoelectric material and their correlation with microstructural features.



## CHAPTER 2

Chapter 2 presents the literature review of new and best performance materials; various process methodologies and strategies adopted to improve the figure-of-merit (ZT) in thermoelectric materials have been reviewed. Emphasis has been given to low-cost silicide-based materials.

### 2.1. Introduction

Silicides have proven to be one of the best candidates for an excellent thermoelectric generation, owing to its enhanced thermoelectric figure of merit, thermal stability, and abundance in earth crust associated with non-toxic nature [43,44,67]. The study of underlying physics, structural and mechanical performance of silicides could open new ways for thermoelectric technology. In the present scenario, thermoelectric materials available for device applications such as Bi<sub>2</sub>Te<sub>3</sub>, Cu<sub>2</sub>Se, PbTe, Bi<sub>2</sub>Se<sub>3</sub>, skutterudites, and half-Heuslers are either toxic or very expensive and low crust abundance [68–70]. Figure 2.1 shows the materials cost of the available thermoelectric materials at present and envisage the futuristic promising thermoelectric material as *n-type* Mg<sub>2</sub>Si and *p-type* MnSi<sub>1.73</sub>. In addition to material cost, production methodology plays a vital role in developing the cost-effective thermoelectric device. The advancement and recent development in the area of manufacturing technology like rapid Spark Plasma Sintering (SPS), would enable mass production, which leads to further reduce the cost of production of thermoelectric materials [71,72].

Most of the metal silicides having a high melting point, optimum band gap (0.5-1.3 eV) with semiconducting properties, favorable for thermoelectric applications. Metal silicides are best suitable materials for the temperature ranges from 500 to 900 K, which covers the entire spectrum of waste heat and solar thermal energy recovery applications.

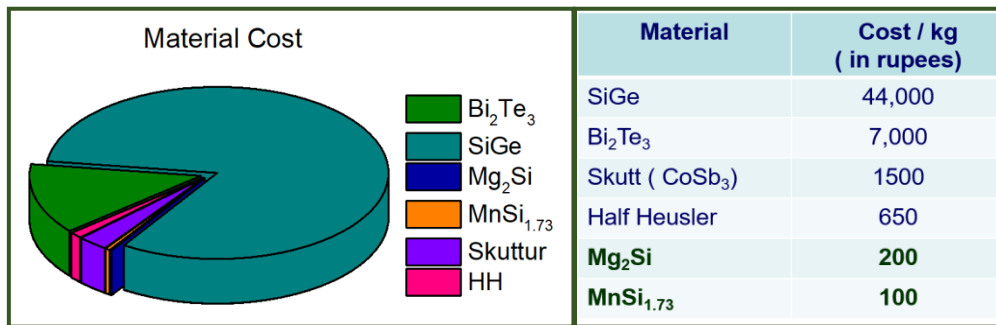


**Figure 2.1. Materials cost for thermoelectric applications [68,73]**

Most of the metal silicides exhibit high electronic properties (Seebeck and electrical conductivity), but their high thermal conductivity brings down its real applications. The engineering of microstructures like nanostructuring, point defect scattering, and nanoinclusions can reduce the thermal conductivity, and it will be useful for future silicide-based thermoelectric technology. Mg<sub>2</sub>Si (n-type) and MnSi<sub>1.73</sub> (p-type) are the ideal combinations for developing a cost-effective and efficient thermoelectric device due to their Seebeck Coefficient compatibility. Mg/Mn-based silicides have low density, resulting in very high conversion efficiency per unit mass. The cost-effective silicide-based thermoelectric materials synthesis makes the thermoelectric technology to play the vital role in future energy challenges.

## 2.2. N-type Magnesium Silicides

Mg<sub>2</sub>Si-based thermoelectric materials are potential materials for thermoelectric generators, due to their attractive figure-of-merit ( $ZT$ ), thermal stability, and earth-abundance of their constituent elements. These properties offer the Mg<sub>2</sub>Si as a promising material for thermoelectric generator applications, as compared to other available state-of-the-art thermoelectric materials, such as Skutterudites, Half-Heuslers and, Chalcogenides. Mg<sub>2</sub>Si-based materials are being explored as an *n-type*

thermoelectric material for TEGs, especially for environment-friendly green energy generation [74,75]. Magnesium silicide ( $\text{Mg}_2\text{Si}$ ), a face-centered-cubic structure, a lattice constant of 0.6351 nm, with an indirect band gap of 0.78 eV and density ( $\rho$ ) of  $\sim 1.98$  g/cc, is shown in Figure 2.2. The structure of  $\text{Mg}_2\text{Si}$  is similar to diamond structure, and there is no bonding between the two magnesium atoms. The  $\text{Mg}_2\text{Si}$  compound shows the bluish-grey color and the distance between the Mg and Si atoms is 0.277 nm. Due to its covalent bonding structure, the  $\text{Mg}_2\text{Si}$  compound has a high melting point ( $\sim 1350$  K) and high hardness value (400-600 HV). The phase diagram for the Mg-Si system is shown in Figure 2.3.  $\text{Mg}_2\text{Si}$  has n-type conduction with an electron carrier concentration  $\sim 10^{17}$   $\text{cm}^{-3}$  and electron mobility  $\sim 370$   $\text{cm}^2 \text{V}^{-1} \text{s}^{-1}$  at room temperature. The main four phases in the Mg-Si phase diagrams are the liquid, (Mg)-hcp, Si-cubic, and  $\text{Mg}_2\text{Si}$  solid phases. There exist three invariant equilibria in this system.

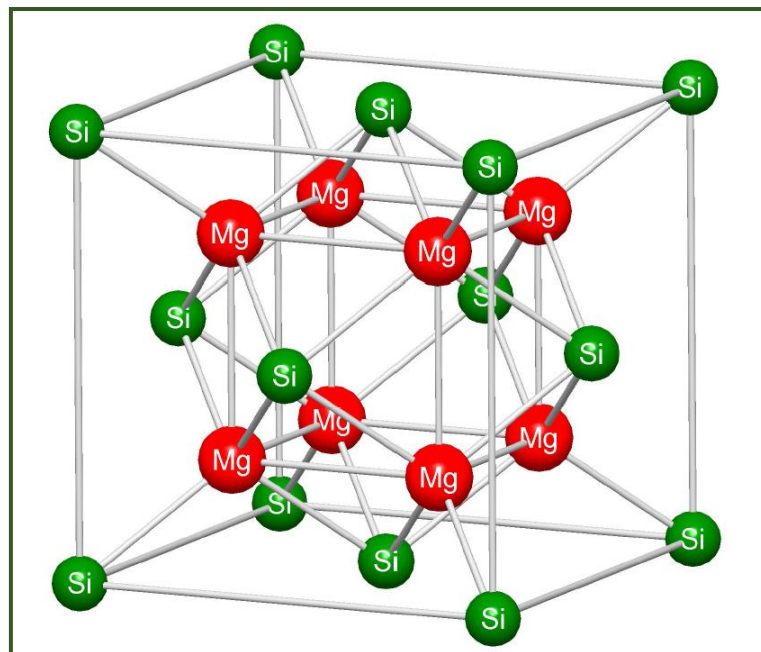


**Figure 2.2.** Schematic diagram of atomic positions in the cubic structure lattice ( $\text{Mg}_2\text{Si}$ ), red color spheres indicate Mg and green indicate Si atoms [76].

They are the eutectic equilibrium on the Mg-rich side,  $L(\text{Mg}) + \text{Mg}_2\text{Si}$ , at 911.88 K; the eutectic equilibrium on the Si-rich side,  $L(\text{Si}) + \text{Mg}_2\text{Si}$ , at 1216.62 K; and the congruent melting of  $\text{Mg}_2\text{Si}$ ,  $L(\text{Mg}_2\text{Si})$ , at 1349.49 K [77]. The synthesis of  $\text{Mg}_2\text{Si}$  is difficult employing the conventional liquid metallurgy technique, due to a huge difference in the melting points of Mg and Si and highly volatile nature of Mg also adds to the problem of maintaining the stoichiometry in the final synthesized  $\text{Mg}_2\text{Si}$ . The reason behind this is, magnesium is highly reactive, and the melting point of magnesium (923 K) and silicon (1685 K) differs largely. The powder metallurgy based techniques lead to the formation of MgO-phase due to highly reactive nature of Mg, which deteriorates the thermoelectric properties of  $\text{Mg}_2\text{Si}$ . Riffel and Schilz used the magnesium and silicon pieces in hardened steel milling balls and hardened steel vessels with milling fluid [78].

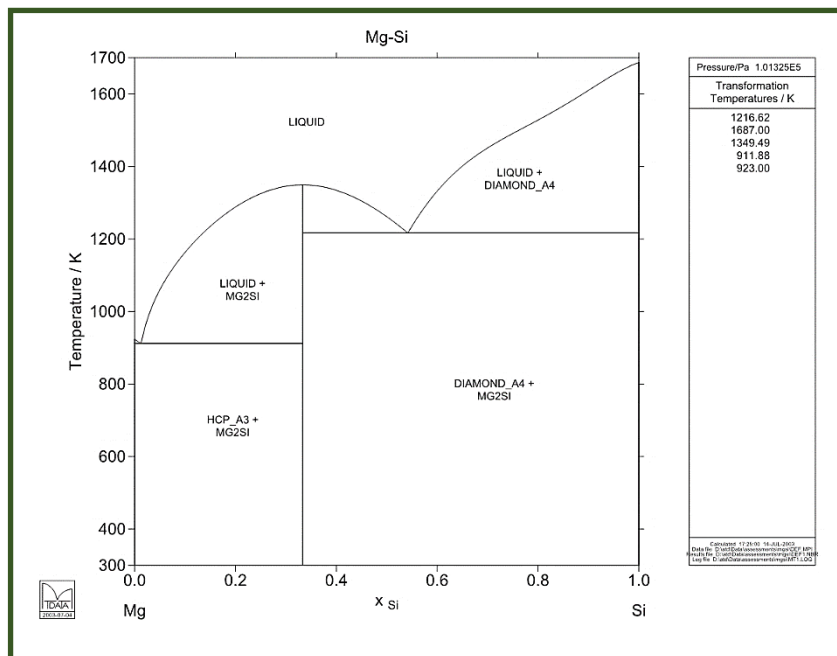


**Figure 2.3. The Mg-Si phase diagram showing the  $\text{Mg}_2\text{Si}$  phase [77].**

Niu and Lu studied the mechanical alloying of magnesium and silicon with powder to ball weight ratio 20:1 [79]. They reported that the formation of  $Mg_2Si$  is not completed even after 30 hours of milling. Clark et al. reported the magnesium silicide formation via ball milling process with 20 hours milling [80]. The formation of magnesium silicide was compared with the literature data. The complete formation of magnesium silicide does not occur in their study. Riffel and Schilz reported magnesium silicide synthesis via mechanical alloying with n-hexane milling fluid and optimized ball milling parameters [81]. Balos et al. reported the complete formation of magnesium silicide employing mechanical alloying with consolidation under the pressure of 464 MPa at 763 K [82]. Kontoh et al. reported the pre-mixed powders of magnesium and silicon compact in a hardened steel die with 600 MPa pressure [83]. The compact is then heated to the temperature  $\sim 1003$  K. The reported synthesis route eliminates the long milling hours for the formation of magnesium silicide. Kontoh et al. again studied the magnesium and silicon elemental powder with repeated plastic working with compaction & extrusion and heated at 773K [84]. The simplest way of formation of magnesium silicide is reported in this study at lower temperatures. Recently Jung et al. reported the synthesis of magnesium silicide by mechanical alloying followed by hot pressing [85]. They reported the mechanical alloying with hot pressing at 1073 K for 2 hours in vacuum at a pressure of 70 MPa to form magnesium silicide. Kajikawa et al. reported the two ways processing of magnesium silicide synthesis, where the required amount of magnesium and silicon were mixed and melted in a crucible and then powdered by ball mill [86]. The powder is again sintered in an argon atmosphere at 1200 K. Kajikawa et al. studied magnesium silicide formation employing spark plasma sintering method [87]. Due to the inherent nature of high diffusion velocity at low temperature, SPS process makes the magnesium silicide formation at the shorter time.

Zhang et al. also reported the SPS processing of magnesium silicide and antimony doped magnesium silicide [88]. They reported the appreciable thermoelectric properties of SPS processed thermoelectric material. Meijun et al. reported magnesium silicide formation with full density, employing SPS. Initially, they synthesized via reaction sintering process employing SPS at 823 K, 10 minutes [89]. The compact was again sintered by SPS at 1023 K, 5 minutes. They have reported the microstructure and XRD analysis of densely formed magnesium silicide. Yang et al. studied the magnesium silicide formation with different holding time in SPS process [90]. Recently, Morozova et al. studied thermoelectric properties doped  $Mg_2Si$  under high pressure and reported the improvement in thermoelectric properties [91]. Li et al. reported the processing and stability of nanostructured magnesium silicide material [92]. Nanostructured magnesium silicide has the advantage over bulk magnesium silicide. Wang et al. reported the formation of nanostructured magnesium silicide through solid state reaction effectively [93]. Wei et al. showed the nanocrystalline  $Mg_2Si$  formation via ball milling and hot pressing in vacuum [94]. They have shown the nanocrystalline structure in SEM analysis. Mei Jun et al. studied the formation of nanocrystalline magnesium silicide employing SPS route and reported the  $ZT \approx 0.36$ , which is 38% higher than that of micro-sized magnesium silicide [95]. Savary et al. recently reported the microwave heating route synthesis of nanostructured magnesium silicide [96]. Although they reported that the microwave heating of nanostructured magnesium silicide is an ultra-fast synthesis process, the supporting thermoelectric properties have not been reported. Further, the limited literature is available on their mechanical properties [97–101], and the reported studies on  $Mg_2Si$ , such as hardness, elastic modulus, and fracture toughness are quite different due to the variation of chemical composition, microstructural effects induced by processing methods.

### 2.3. P-type Manganese Silicides

Higher Manganese Silicides (HMS) are a unique family of intermetallic compounds that are regarded as potential thermoelectric materials, due to their earth-abundant and environmentally-friendly constituent elements coupled with high oxidation resistance [43,44,102]. Higher manganese silicides are the promising *p-type* compatible to the existing *n-type*  $\text{Mg}_2\text{Si}$ . HMSs are Nowotny Chimney-ladder phases, with an indirect band gap of 0.4- 0.7 eV and density ( $\rho$ ) of  $\sim 5.18$  g/cc, is shown in Figure 2.4.

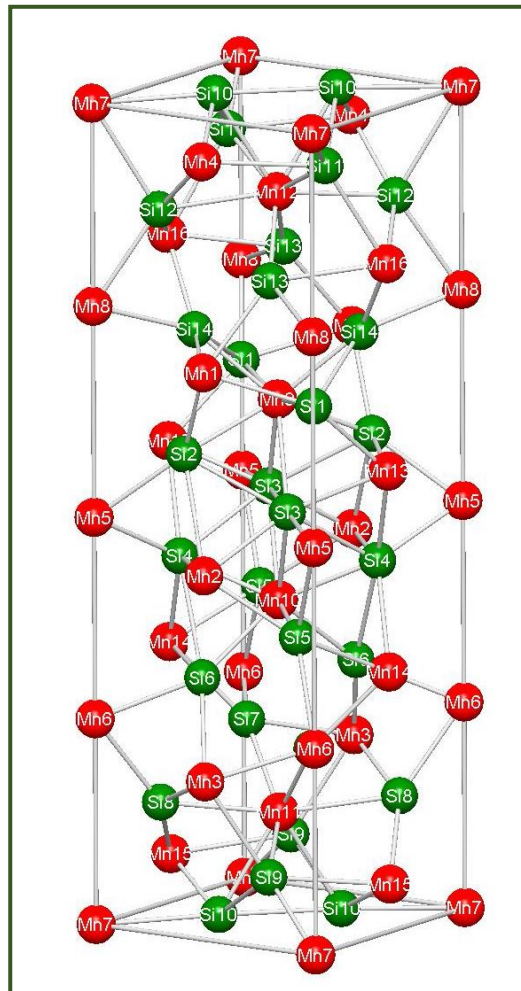


**Figure 2.4. Schematic diagram of atomic positions in the tetragonal structure of  $\text{MnSi}_{1.75}$ , red color spheres indicate Mn and green indicate Si atoms [76]**

Higher manganese silicides, the chemical formula  $\text{MnSi}_{1.75-x}$ , shows different tetragonal phases  $\text{Mn}_4\text{Si}_7$ ,  $\text{Mn}_{11}\text{Si}_{19}$ ,  $\text{Mn}_{15}\text{Si}_{26}$ , and  $\text{Mn}_{27}\text{Si}_{47}$ , with a lattice constant ‘a’ of  $\sim 0.552$  nm and lattice constants ‘c’ of  $\sim 1.75$ , 4.81, 6.53 and 11.8 nm, respectively. The Mn atoms form the exterior ‘chimneys’ within which the Si atoms are arranged in a spiral ladder. They have p-type conduction with a high hole carrier concentration  $\sim 10^{21}$   $\text{cm}^{-3}$  and hole mobility  $\sim 1$   $\text{cm}^2 \text{V}^{-1} \text{s}^{-1}$  at room temperature. For Silicide thermoelectric generators design, the most compatible material for n-type  $\text{Mg}_2\text{Si}$  is higher manganese silicide (p-type HMS). The preparation of p-type higher manganese silicide alloys for thermoelectric applications is quite challenging. The Mn and Si phase diagram shows the existence of HMS phase at a very narrow range is shown in Figure 2.5, which evolves the synthesis of single phase HMS to be difficult. HMS phase forms at 1432 K and has several structure variations, which can be represented by the formula  $\text{MnSi}_x$ , within its range  $\text{MnSi}_{1.7}$  to  $\text{MnSi}_{1.75}$  [52,103–105].

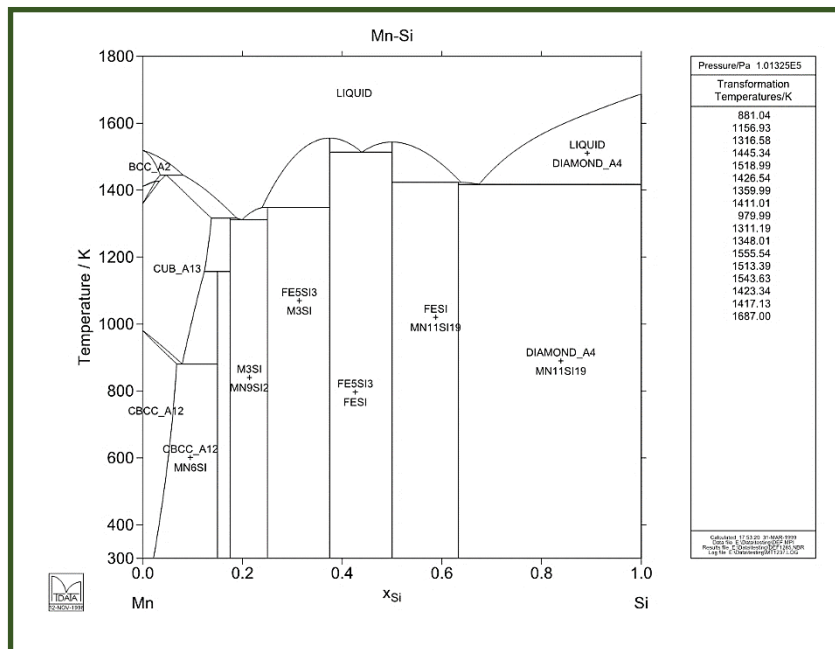


**Figure 2.5.** The Mn-Si phase diagram showing the HMS phase, narrow range  $\text{MnSi}_{1.7}$  to  $\text{MnSi}_{1.75}$  [106].



The presence of metallic cubic-MnSi is unavoidable in HMS phase. Several approaches have been made to overcome the MnSi existence in HMS phase. Luo et al. showed rapid synthesis Melt-spinning followed by SPS synthesis to avoid MnSi phase in HMS phase [107]. They reported that in-situ method of synthesizing nanophase MnSi in HMS phase would be a solution to enhance the performance of HMS. Sadia & Gelbstein showed the synthesis of HMS employing SPS at 1123 K [108]. Further, the studies on dopants addition in HMS phase, Al [109], Ge [51], Fe [110] and Cr [111], reported the enhancement of thermoelectric property in HMS. Itoh et al. showed the influences of mechanical alloying parameters on thermoelectric properties and reported a maximum value of  $ZT \approx 0.47$  at 873 K [112]. Famengo et al. showed the influences of phase content on thermoelectric properties and reported a maximum value of  $ZT \approx 0.34$  at 873 K [113]. The three-step process, vacuum melting, milling and hot-pressing results in a maximum value of  $ZT \approx 0.3$  at 793K [34]. The vacuum sealed annealing and SPS is resulted in a maximum value of  $ZT \approx 0.6$  at 723K, by Satia et al. [108]. Shin et al. [114] recently studied the influences of processing temperature on thermoelectric properties and reported a maximum value of  $ZT \approx 0.28$  at 823K. Nhi Truong et al. showed the improvement of thermoelectric properties by the addition of multi-walled carbon nanotubes in HMS [115]. Also, the trace amount of metallic Cubic-MnSi phase segregates normal to the c axis, and the MnSi is highly conducting hole carrier concentration ( $\sim 10^{22} \text{ cm}^{-3}$ ).

From the literature, it is well known that if the thermoelectric devices have to compete with other established sources of renewable energy the thermoelectric properties of their material couple, has to be substantially enhanced along with reducing their material and processing costs. Currently, the thermoelectric material couple *n-type*  $\text{Mg}_2\text{Si}/p\text{-type}$   $\text{MnSi}_{1.73}$  has been recognized as the most promising for thermoelectric

generator applications, owing to its thermal stability and earth-abundant & non-toxic nature of its constituent elements. In view of the fact that despite *n-type* Mg<sub>2</sub>Si/*p-type* MnSi<sub>1.73</sub> been extensively researched for the past couple of years for the enhancement of thermoelectric performance, its ZT is still limited to ~ 0.4 to 0.5. Further, the blueprint of simple and scalable experimental strategies has not been reported for the enhancement of its thermoelectric performance.

The relationships between microstructure and thermoelectric properties of *n-type* Mg<sub>2</sub>Si/*p-type* MnSi<sub>1.73</sub> are highly expected, to understand the various controlling mechanism of thermal and electronic transport properties, which have not been studied thus far. Apart from thermoelectric properties, to ensure the device integrity of the thermoelectric material, the mechanical properties of the synthesized material are concurrently imperative to avoid structural failure of their thermoelectric modules during actual operation. Dearth of knowledge, the comprehensive study on the mechanical properties of *n-type* Mg<sub>2</sub>Si and *p-type* MnSi<sub>1.73</sub> including elastic modulus, hardness, fracture toughness, thermal shock resistance and friction & wear properties have not been carried out, to understand the endurance limit of the material under real hostile environmental conditions

# CHAPTER 3

Chapter 3 describes the different material synthesis techniques employed in the current work, such as high energy ball milling, arc melting, melt spinning and spark plasma sintering, etc. The material characterization techniques, X-ray diffractometer, field emission scanning electron microscope, high-resolution transmission electron microscope, and energy dispersive spectroscopy have been described. The Seebeck coefficients, electrical and thermal properties using ZEM-3, Laser Flash Apparatus have been discussed in detail. The mechanical properties evaluation techniques, microhardness tester, nanoindentation and wear-friction monitor have also been described in detail.

## **3.1. Introduction**

The advanced manufacturing processes employed in the current work, such as mechanical alloying, rapid solidification melt spinning and plasma assisted reactive spark plasma sintering, etc. are described in detail to realize the efficient silicide-based thermoelectric *n-type* Mg<sub>2</sub>Si and *p-type* MnSi<sub>1.73</sub> materials. The advanced material characterization techniques X-ray diffraction (XRD), field emission scanning electron microscopy (FESEM), high-resolution transmission electron microscopy (HRTEM) and energy dispersive spectroscopy (EDS) have been discussed. The thermal transport and mechanical properties characterization tools have also been discussed in detail.

## **3.2. Experimental techniques used for material synthesis**

### **3.2.1. High Energy Ball Milling (HEBM)**

Ball milling is a powder processing technique used to mix or blend elemental materials. The dry/wet high energy ball milling process involves two or more elemental powders are blended, cold worked, welded and repeatedly fragmented, resulting in

powders with a uniform atomic distribution. The process comprises of fracturing, welding and tearing of tiny particles in between hardened balls inside the bowls [116]. The process of milling is not only limited to the production of complex dispersion strengthened materials but is also producing nanostructured metal powders with controlled, extremely fine microstructures. It is capable of synthesizing a variety of equilibrium and non-equilibrium alloy phases [117]. In ball milling process, the powder mixture consisting elemental powder particles or alloying particles is loaded in the container (known as bowl, jar or vials) of a ball milling machine, together with hardened balls. This mix is then milled for the required time duration until a steady state is reached where the composition of every powder particle is the same as the chemical and size proportion of the desired final products. The milled powder is then compacted into a bulk shape and sintered to obtain the desired microstructure and properties. Ball milling process provides the opportunity for fine dispersion of particles in the alloying system, an increase the level of solid solubility, grain refinement down to nm range. Here, ball mills are also widely used for mixing, blending and dispersing of materials.

The essential components of the milling process are raw materials, types of mills, process variables. Commercially powders with particles sizes ranging from 1 to 200  $\mu\text{m}$  are usually processed in high energy ball milling technique. The types of mills available depending upon the functions are shaking, an attritor and planetary mills. In milling process, the progress and the end product are greatly influenced by the number of processing parameters. The vital parameters are, 1) impact of milling container and grinding medium, 2) milling time and milling speed, 3) Ball-to-Powder Weight Ratio, 4) extent of filling the vial, 5) effect of milling atmosphere and 6) Role of process control agent. Ball milling process is one of the top-down approach technique; the bulk material is broken into the micro- or nanosized particles.

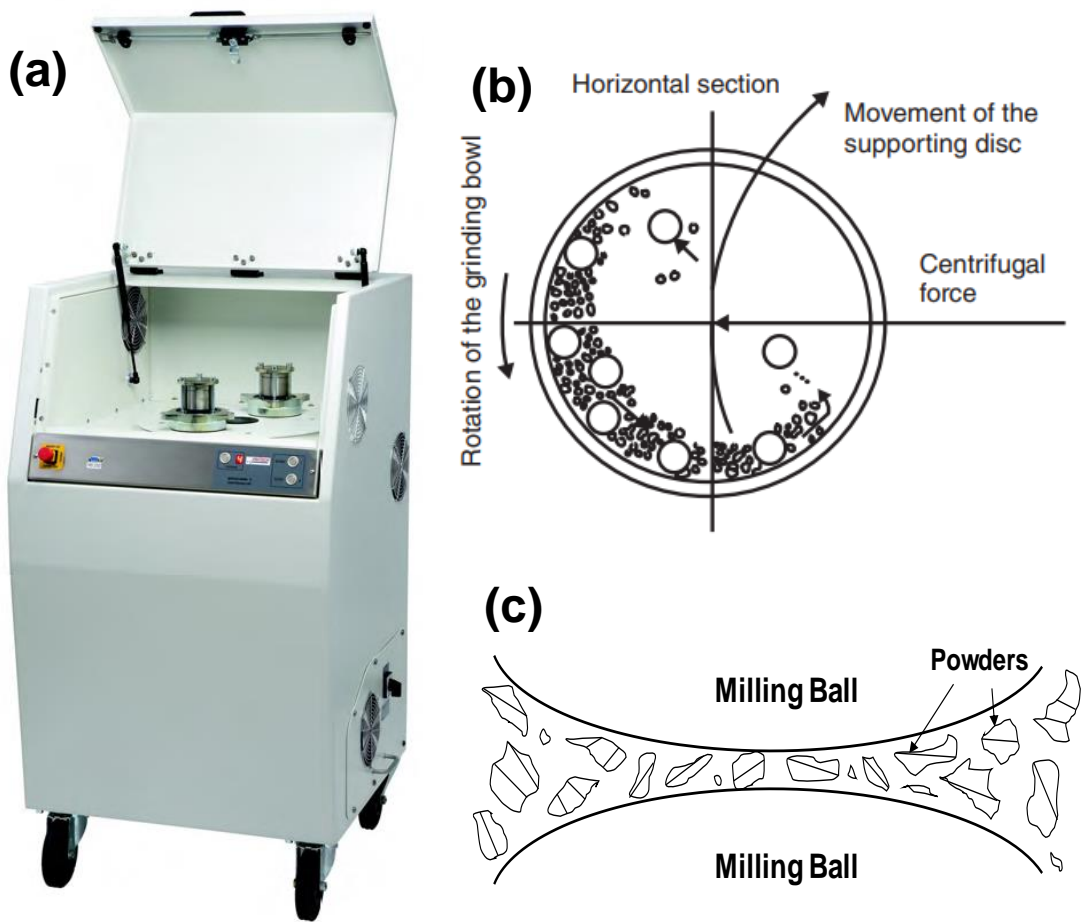


**Figure 3.1. (a) High energy ball mill (M/s. Fritsch, Pulverisette, P-4, Germany) used for ball milling (b) Schematic diagram showing the ball movement inside the ball mill and (c) powder particles trapped between the balls.**

The blending of constituent elements of silicides ( $Mg_2Si$  &  $MnSi_{1.73}$ ) thermoelectric materials is performed by using high energy ball mill technique before subjected to reactive spark plasma sintering (SPS). Milling technique is also used for the milling of nanostructured higher manganese silicide flakes/ribbons, combined with rapid SPS consolidation. The elemental powders filled into a stainless-steel bowl with balls at 15:1 balls to materials weight ratio. The ball milling experiments are carried out

in an inert argon atmosphere. In addition to particle size reduction, ball milling experiments are used here for mixing, blending and dispersing of doping materials. The blended and milled elemental powders are handled in an inert glove box before sintering process, to avoid oxidation and contamination. The glove box used for loading and unloading of milled powders from the Stainless Steels Jars/Balls is shown in Figure 3.2. The antechamber is provided for transferring material in and out of the main inert Glove box without disturbing the inert internal atmosphere.



**Figure 3.2. Glove box used for loading and unloading of ball milled powders from the Stainless-Steel Jars (Make: Mbraun, Germany, Model: MB20)**

### **3.2.2. Melt Spinning equipment**

Melt spinning is a rapid solidification technique, which provides high & rapid cooling to the materials, producing nanoscale features in its microstructures. This method is used to develop materials that require extremely high cooling rates to form, amorphous, nano and ultrafine grain structured materials [30,118,119]. A simple representation of the working principle of melt spinning technique is shown in Figure 3.3. Melt spinning is a technique used for splash cooling of melted materials to make a unique class of materials. Materials are being melted employing induction melting technology. A thin film of melted material is ejected onto the water-cooled fast rotating

copper wheel causing rapid solidification in the form of ribbon or flakes. Surface velocity of 35m/s can be achieved from Melt Spinner HV. Due to rapid cooling (cooling rate  $\sim 10^7$  K/s maximum) nanostructured or amorphous material can be synthesized. The maximum melting of materials  $\sim 1750$  K can be achieved from Melt Spinner HV.

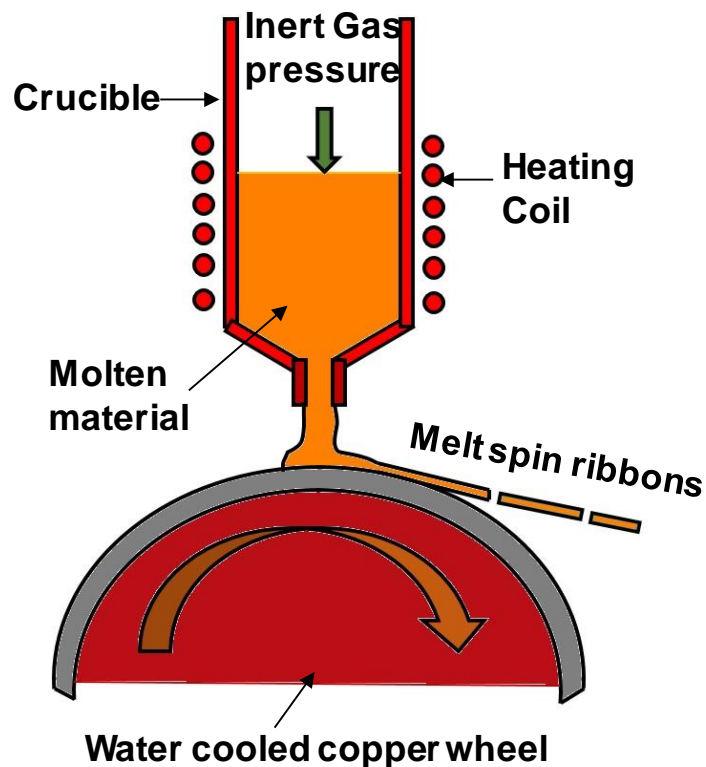


**Figure 3.3. Schematic of Melt spinning process**

The boron nitride or quartz crucible with slit nozzle is being utilized for melting the specified quantity of ingots. The melt-spinning experiment is carried out in Melt Spinner unit has a copper spinning wheel  $\varnothing$  250 mm with variable wheel speeds ranging from 5 to 45 Hz. The entire chamber is being evacuated with a diffusion pump and purged with argon. The molten alloy is injected by inert argon gas, through the split type nozzle over the water-cooled copper wheel. The solidified material in the water-

cooled copper wheel is being thrown out in the form of small strips. The supercooled ribbons/flakes are being collected from the chamber, after the experiments. The microstructural features of melt-spun materials mostly depend on the processing parameters, wheel speed, ejection gas pressure, melt temperature and slit-wheel gap. The thickness of the melt-spun ribbons is the vital parameter for the final product and mainly depends on the cooling rates. In melt spinning technique, the wheel speed is directly proportional to the cooling rate. Here, the nanostructured material is synthesized using melt spinning, varying the cooling rates.



**Figure 3.4. (a) Melt Spinning Unit (Make: Edmund Buhler GmbH, Model: Melt Spinner HV) used for synthesizing nanostructured ribbons/flakes (b) Water cooled Copper wheel with crucible**

### **3.2.3. Spark plasma sintering**

Spark plasma sintering (SPS) is a rapid sintering process in which high ampere direct current is applied to sinter the materials under pressure, and hence fast sintering



rate could be achieved over large volume products. The kinetics and improved diffusion during SPS process benefit in synthesizing a variety of materials that could not be processed using conventional materials fabrication methods. The SPS process sinter the material at lower temperatures than conventional methods and in shorter duration since the powders are heated rapidly by the spark plasma, which has a surface activation effect on the powders being sintered. Spark plasma sintering is an advanced material processing technique used to synthesize high-dense materials from materials/alloy powders by applying rapid spark plasma thermal energy. The processing temperature used for SPS process is generally well below the melting point of the material. The sintering process is mainly divided into two categories- solid state sintering and liquid phase sintering. In solid-state sintering, the powder compact is densified only in a solid state, while liquid phase exists in the powder during liquid phase sintering. Spark plasma sintering (SPS) is a rapid and reactive pressure assisted sintering technology capable of sintering variety of materials (metals, alloys, ceramics, and composites). A high-current, low-voltage power shortly generates spark plasma in the area of contacts between particles. The material can be processed the temperature range between 473-2273 K and usually are 473-773 K lower than with conventional sintering. The quite low temperature associated with fast processing time ensures the improved control over the grain growth, recrystallization, and microstructure of the sintered material.

SPS utilizes uni-axial pressure and direct current pulse high amperage current to create spark plasma discharge and Joule heating points in between the particles. The spark disperses throughout the specimen, resulting in a quick and uniform heat distribution, homogeneous and dense structure. SPS technology makes it possible to sinter the materials without the use of binders. Most conventional sintering processes involve green powder pre-forming with binders, and it leads to expensive binder

removal processes. Binders more often deteriorate the material properties due to their chemical susceptibility, and oxidation breakdown. SPS technology makes it possible to sinter nano-crystalline materials; the bulk nanostructured materials testing is now open to study new ideas in nanomaterials applications.

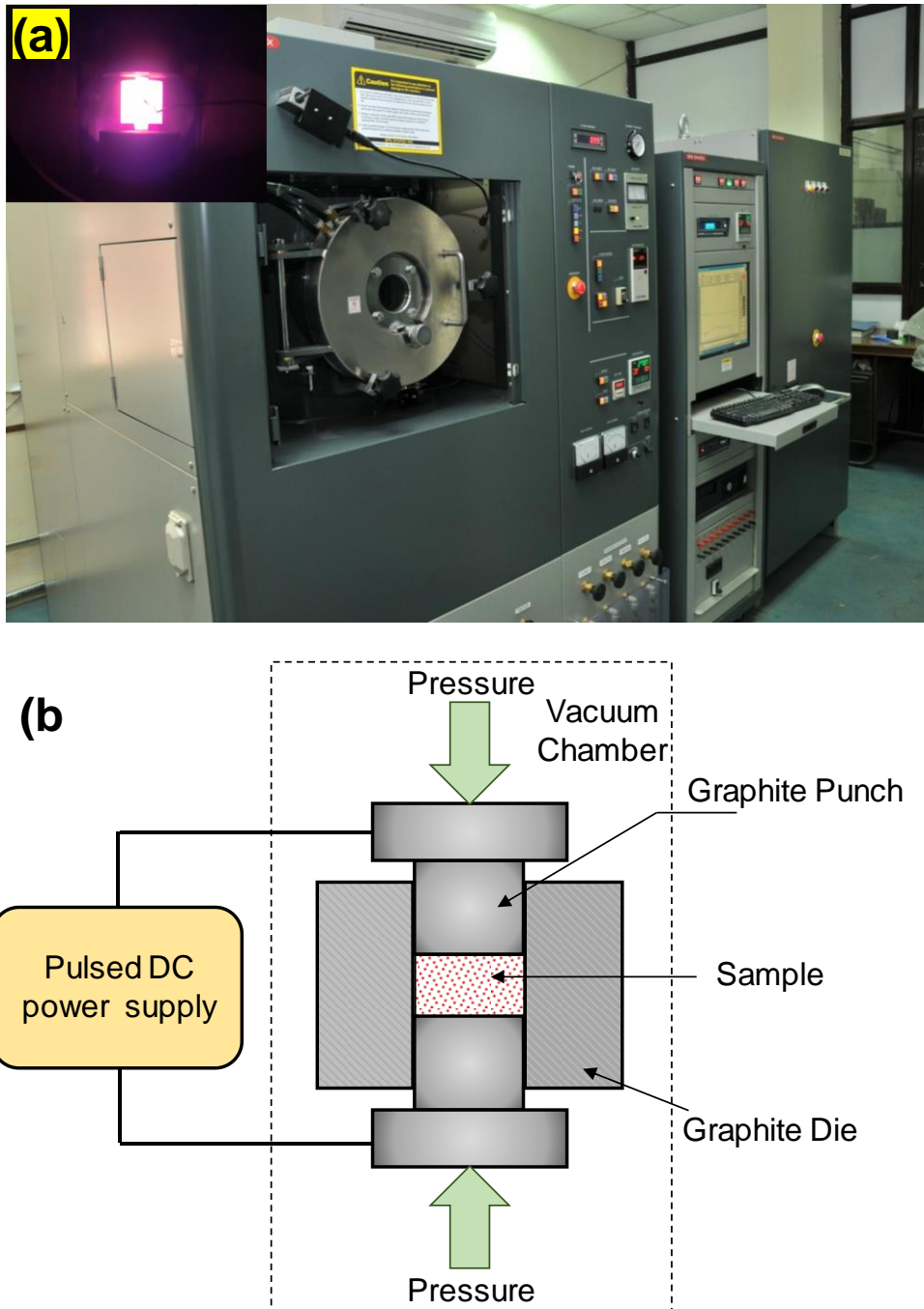


**Figure 3.5. (a) Spark plasma sintering facility (SPS 725, Fuji electric co., Japan) used for materials synthesis (b) principle of operation.**

The two major approaches have experimented in this study to synthesize silicide-based materials and to enhance the thermoelectric figure of merit (ZT). The first method focuses on creating the material with reactive assisted spark plasma sintering with desired properties. The other method focuses on bulk nanostructured material development employing melt spinning combined rapid SPS technique. The brief description of the two methods is discussed in the following text. In the first approach, the in-situ reaction between the material powders and their compaction takes place in the SPS process, and thus the sintering consumes short time duration as compared to long processing hours using conventional sintering techniques. During SPS, spark plasma generation, and consolidation takes place under the axial force to facilitate the material consumes less time in the low-temperature, where non-densifying mechanisms, such as surface diffusion are active, and proceeds quickly to higher temperatures where densifying mechanisms, such as grain boundary or volume diffusion are dominant. In the second approach, to achieve bulk nanostructured materials, a rapid densification with limited grain growth rapid SPS process has been introduced. The nanostructured ribbons/flakes obtained by the melt spinning process are consolidated by spark plasma sintering employing the heating rate of 100 K /min. Thus, the nanostructured features introduced by melt spinning technique are retained in spark plasma sintering compaction, exhibiting a high density of nano-scale nanocrystallite boundaries at different length scales.

### **3.3. Experimental techniques used for material characterization**

#### **3.3.1. X-ray diffraction analysis**

X-ray diffraction (XRD) is a versatile, non-destructive technique that reveals the detailed information about the chemical composition and crystallographic structure of natural and synthesized materials. It is a rapid analytical technique primarily used for

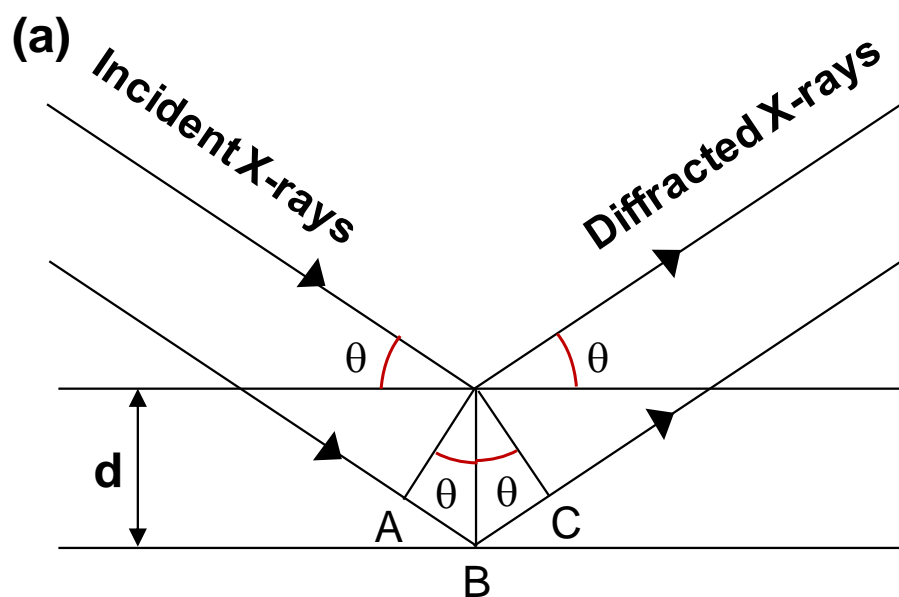


**Figure 3.6. (a) Basic principles of X-ray diffraction and Bragg's law, (b) X-Ray Diffractometer used for characterization of crystal structure and phase purity of synthesized materials (Rigaku, Japan, Model- Miniflex-II)**

phase identification of a crystalline material and can provide information on unit cell dimensions. Also, XRD only provides the collective information of the particle sizes and usually requires a sizable amount of powder. X-ray diffraction techniques would be used for phase and crystallinity analysis and also used to estimate the

crystallite size in developed thermoelectric nanomaterials. X-ray diffraction (XRD) is a useful tool for phase structure determination of the of crystalline materials. The structural analysis is carried out by relating diffraction intensity and peak positions values with the ICDD powder diffraction reference patterns of known elements and compounds. In the present study, X-ray powder diffractometer with Cu  $K_{\alpha 1}$  source ( $\lambda=1.540 \text{ \AA}$  with Ni filter) has been used for determining the phase purity and crystal structure characterization of the synthesized material (Figure 3.6)

### **3.3.2. Scanning electron microscope analysis**

The scanning electron microscope analysis provides the grain & grain boundary information and microstructural phase analysis of solid-state materials. It will give the opportunities & better understanding of structure-property correlations of different kind of materials. It is a very useful tool for nanostructure engineering, compositional control of the compounds and to tailor the physical properties. SEM analysis provides the opportunity for establishing structure-property correlations of synthesized thermoelectric materials.

Understanding principles of Scanning electron microscope are classified the major categories as, electron optics, electron beam-specimen interactions, types of signals mode, quality of the signals and image processors. The main parameters associated with SEM & analysis specimen that one can control are Beam accelerating voltage, Probe convergence angle, Probe current, Probe diameter. Electrons are emitted from a field emission gun source and are focused by electromagnetic lenses. The produced narrow beam impinges the object. The impingement results in the generation of secondary electrons, backscattered electrons, characteristic X-rays, etc. Suitable detectors can detect the angle and velocity of these electrons and provide information about the microstructure and morphology of the materials. A field-emission gun

delivers narrow beams at high and low electron energy which offers improved spatial resolution and minimized sample charging. Analysis of the microstructure and elemental analysis of synthesized  $\text{Mg}_2\text{Si}$  and  $\text{MnSi}_{1.73}$  is performed by FESEM (SUPRA 40VP; Zeiss, Germany). Also, the indentation, crack length, and worn surface analysis is studied using FESEM for better accuracy.

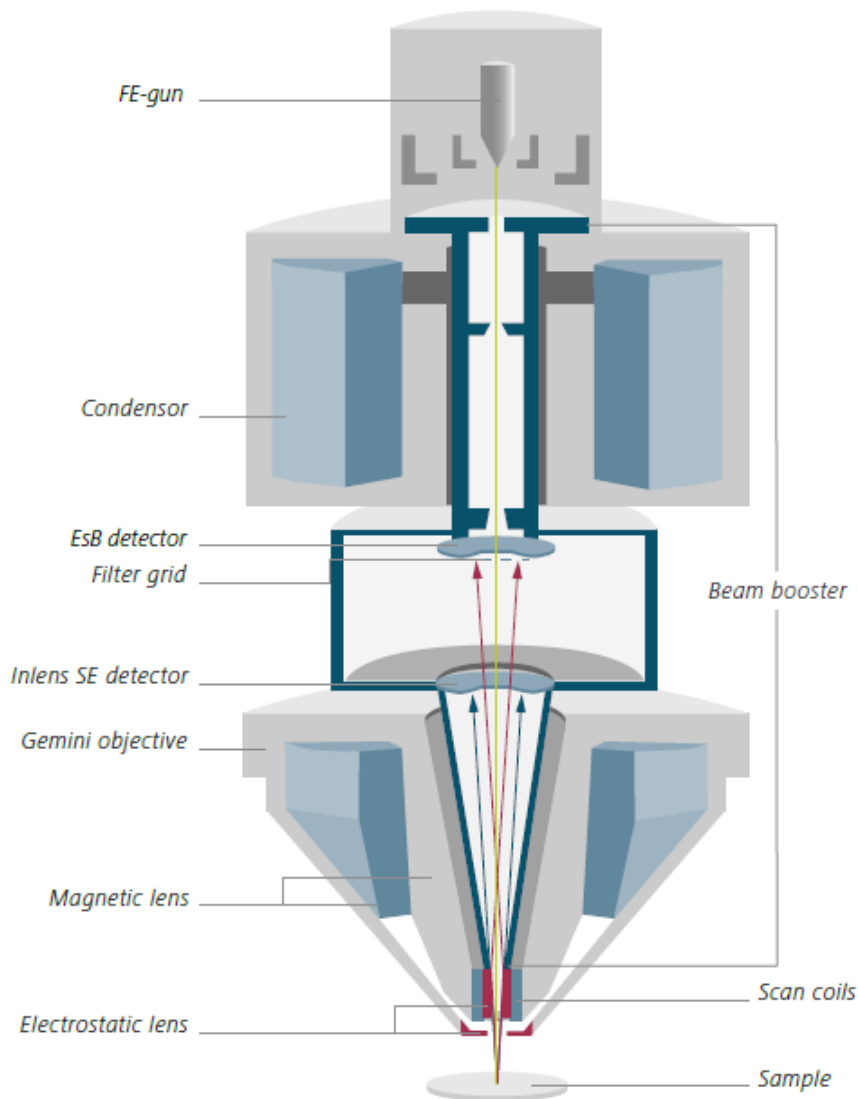


**Figure 3.7. The schematic and working principle of Field emission scanning electron microscope**



**Figure 3.8.** Field emission scanning electron microscope (Zeiss, Supra 40VP, Germany) used for microstructure analysis.

### **3.3.3. Transmission electron microscope analysis**

High-resolution Transmission electron microscope (HRTEM) elucidates high magnified microstructures and diffraction patterns of the specimen by an electron beam which transmitted through the specimen and interacts with it. TEM is an effective method for the lattice scale characterization of materials at high magnification and high resolution. The material could also be studied in reciprocal space. TEM analysis is useful for determination of crystallographic structures by selected area electron diffraction and identification of various phase transformation in the material.

In case of nanomaterials, it is an indispensable characterization tool. Spectroscopy attachment to the main microscope is useful for the elemental analysis at the nanoscale. The electron transparent (< 50 nm thick) solid samples are characterized by using transmission of focused a high energy beam of electrons in an ultrahigh vacuum.

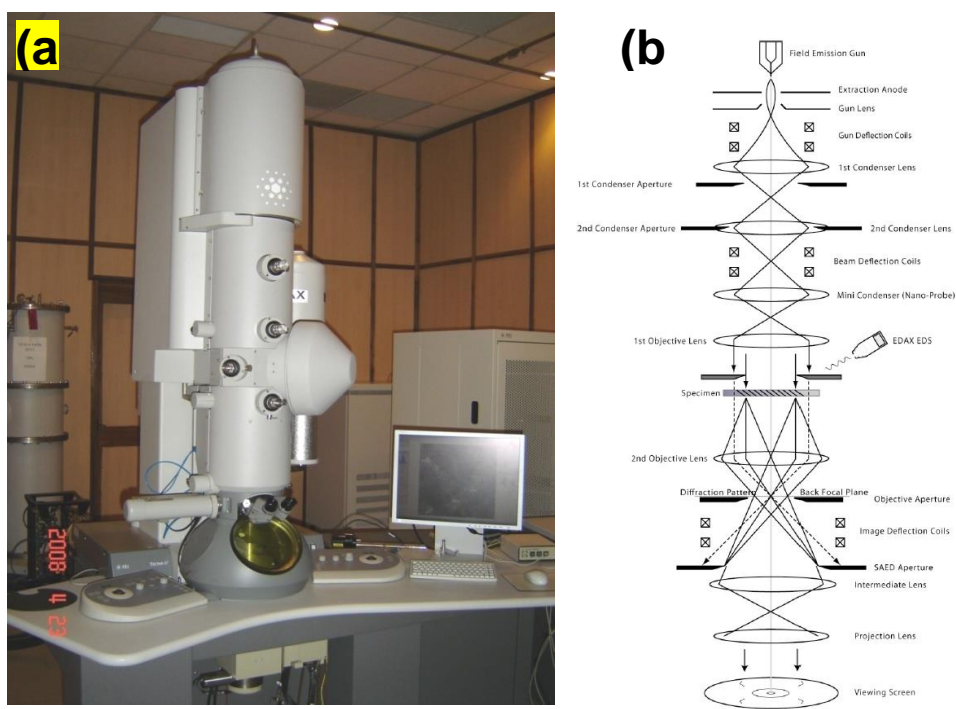


**Figure 3.9. a) High-Resolution Transmission electron microscope (Tecnai G2 F30 STWIN, Germany) used for nanostructure and lattice scale imaging (b) Schematic and working principle of HR-TEM**

The advantages of a field emission system are its better coherence and higher brightness. The high resolution – TEM (HRTEM) will be utilized for characterization of different thermoelectric materials to reveal the topography and internal structure of the materials at even up to sub-nano scale including interfaces and grain boundaries. Using selected area electron diffraction patterns (SAEDPs), the reciprocal space can be explained to understand the crystal structures, phase formations, and orientation relationships.

### **3.4. Experimental techniques used for thermoelectric transport properties measurements**

#### **3.4.1. Thermal transport properties**

Thermal conductivity is an essential property of the thermoelectric material. The high figure-of-merit ( $ZT$ ) of the thermoelectric material can be achieved by decreasing



the thermal conductivity. The thermal conductivity of materials can be determined by either a steady-state method or an unsteady state method.

### 3.4.1.1. Thermal diffusivity measurement

Laser flash diffusivity is the best method to determine the thermal conductivity of the materials, ranges from 150 K to 3000 K.

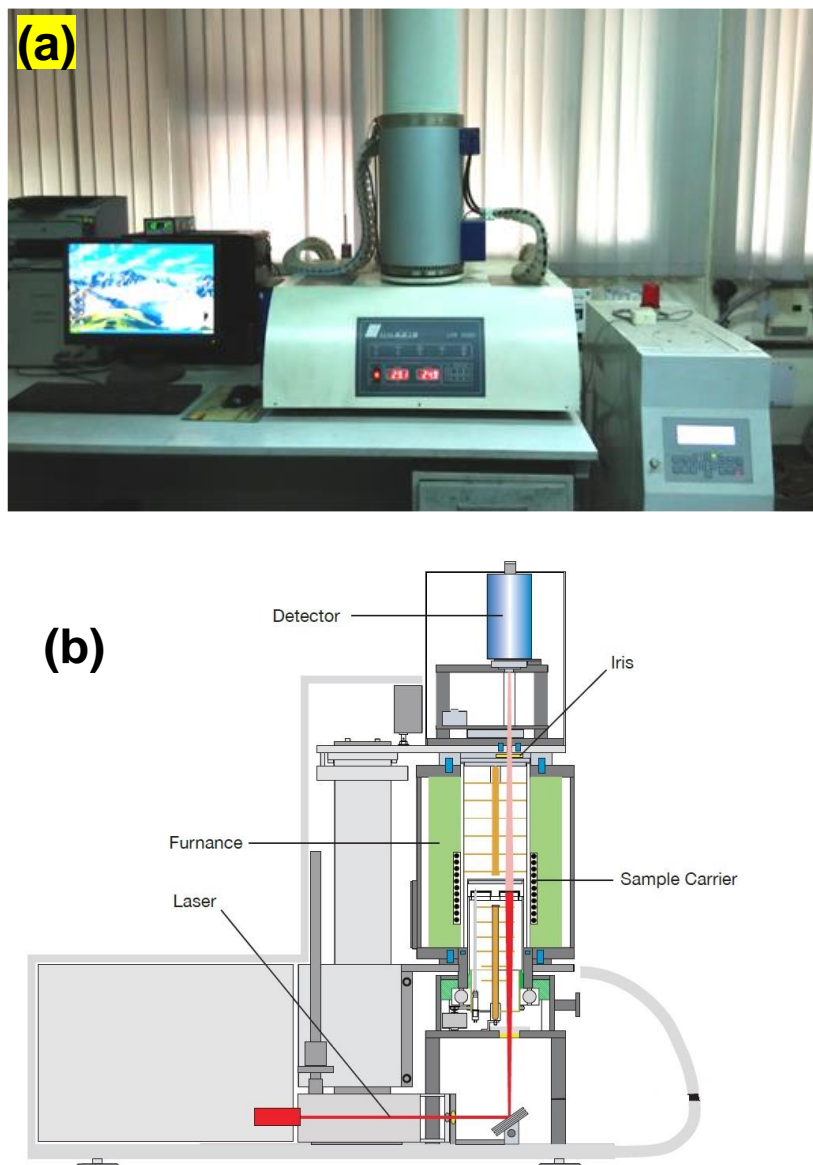


**Figure 3.10. (a) Thermal diffusivity measurement (LFA 1000. Linseis, Germany) facility (b) Schematic and working principle.**

The laser flash technique is presently the most commonly used method for accurate measurement of the thermal diffusivity of the thermoelectric materials. The high precision, reproducibility, and short measurement times are outstanding features of LFA measurement over the Entire application range from RT to 1273 K. The sample is placed on a fabricated silicon carbide sample holder, which is surrounded by a predetermined temperature controlled furnace. The rear side of the specimen is irradiated by using a programmable high-intensity short duration radiant laser energy pulse. The resulting temperature rise on the rear face is measured by using a sensitive high-speed IR detector. The thickness of the sample and the time required for temperature rise in the front face to rear face reaching a percentage of its maximum value provides the thermal diffusivity. If the density ( $\rho$ ) and specific heat ( $C_p$ ) are identified, the thermal conductivity can be computed by using the expression: Thermal conductivity ( $\kappa$ ) = Diffusivity ( $D$ )  $\times$  specific heat ( $C_p$ )  $\times$  density ( $\rho$ ).

#### **3.4.1.2. Specific heat capacity measurement**

Specific heat capacity ( $C_p$ ) is a material property describing the energy required to induce an absolute change in the temperature of a unit mass of the material. A differential scanning calorimeter (DSC) has been employed to determine the specific heat values. The DSC measures specific heat capacity by heating a sample and measuring the temperature difference between the sample and a reference. Reference and sample crucibles are placed on a sample carrier within a furnace of cylindric geometry which generates heat radially toward the center. Thermocouples detect temperature in contact with each crucible. One thermo element is shared between the crucibles allowing the temperature difference to be measured as a voltage. Three measurements are necessary for calculating specific heat. First, a Baseline is recorded. The baseline is the response with both crucibles empty, yielding a signal bias inherent

in the system. Next is a reference test, in which a sample with a well-defined specific heat is tested for comparison to an experimental specimen. Finally, an experimental sample is tested. The “Baseline” allows removal of system bias from the data, while the reference test enables calculation of the specific heat of the experimental sample as a ratio of the reference material specific heat.



**Figure 3.11. (a) Differential scanning calorimeter used for Specific heat (Cp) measurements ( Make: Netzsch, Germany, Model: 404 F3)**

### 3.4.1.3. Density measurement

The density determination of the synthesized samples was performed using Archimedes principle. Water is taken as liquid media with a known density of 1g/cc. The measurement of the weight of the sample in air and water using the density kit shown in Figure 3.12. The density of the sample calculated by using  $\rho_s = [W_a / (W_a - W_w)] \times \rho_w$ , where,  $\rho_s$  density of the samples in ( $\text{g}/\text{cm}^3$ ),  $\rho_w$  density of water ( $\text{g}/\text{cm}^3$ ),  $W_a$  is the weight of sample in air and  $W_w$  is the weight of the sample in liquid.



**Figure 3.12. Density measurement setup (M/S. Mettler Toledo)**

### **3.4.1. Electrical transport properties**

#### **3.4.1.1. Seebeck coefficient measurement & Electrical conductivity measurement**

The Seebeck coefficient ( $\alpha$ ) of a material provides the magnitude of an induced voltage in response to a temperature difference across the material. Seebeck coefficient is one of the crucial property of thermoelectric materials and directly related to the thermoelectric performance. Seebeck coefficient is measured by the instrument ZEM-3 (Figure 3.13, ULVAC RIKO, Japan). Rectangular Solid samples (maximum of 4mm thick  $\times$  4mm width  $\times$  12 mm height), (minimum of 2mm thick  $\times$  2mm width  $\times$  12 mm height) are required for the measurements of Seebeck coefficient and electrical resistivity measurements, as shown in Figure 3.13(b). A rectangular sample is placed in a position between the upper and lower platinum electrodes in the heating furnace. The sample is held at a specified temperature inside the furnace; then it is subjected to localized heating by the heater in the lower Pt electrode to make a temperature gradient. Seebeck coefficient of the specimen is determined by using upper and lower temperatures T1 and T2 with the thermocouples positioned against the sample, followed

by estimation of thermal electromotive force(emf) between the same thermocouple wires as shown in Figure 3.13.

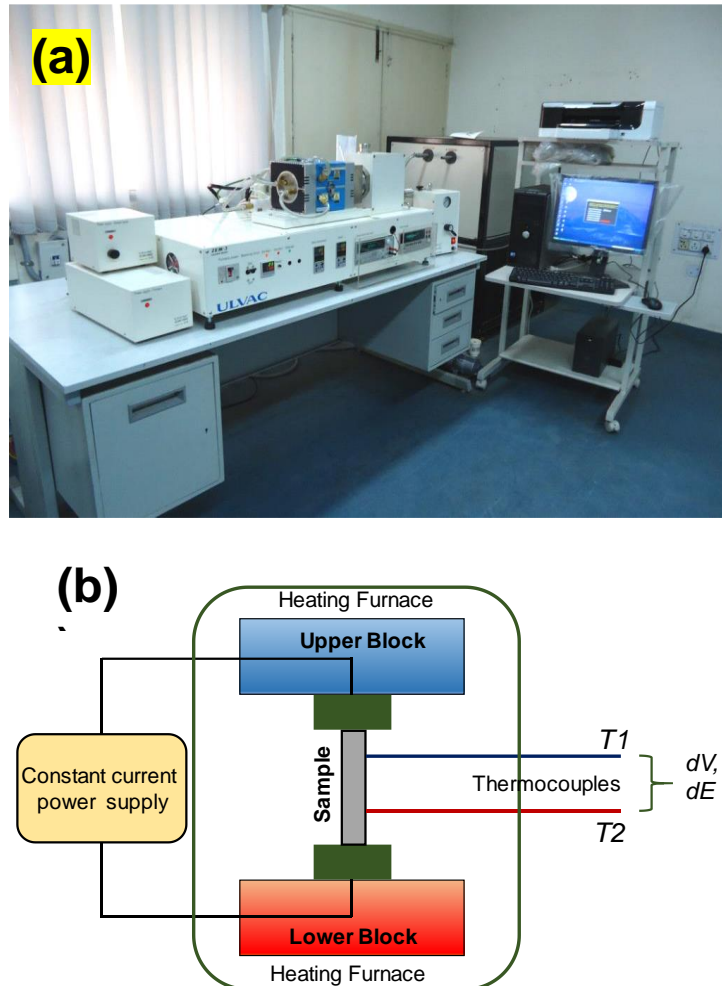


**Figure 3.13. (a) Seebeck coefficient and electrical resistivity measurement (M/s. ULVAC, ZEM-3, Japan) facility (b) Schematic and working principle.**

Electric resistance is measured by the dc four-terminal method, in which a DC current is applied to both ends of the specimens to measure and determine voltage drop  $dV$  between the thermo-electromotive force between leads. The system automatically examines the contact of the two probes with a sample ohmic property and uses the best value of electric current to determine the resistivity of the sample without the influence of heat transfer. Rectangular specimens ( $3 \times 3 \times 12\text{mm}$ ) were cut from the center of the

synthesized samples, Mg<sub>2</sub>Si & MnSi<sub>1.73</sub>, for the evaluation of Seebeck coefficient and electrical conductivity. Seebeck coefficient and electrical conductivity are measured simultaneously in Helium atmosphere from room temperature to 873 K. The accuracies in the Seebeck coefficient, and electrical conductivity measurements in the present study using ZEM-3 are  $\pm 6\%$  and  $\pm 10\%$ , respectively.

### 3.4.1.2. Hall properties measurement

The Hall transport properties were characterized by using HEMS system (Nanomagnetics Instruments, U.K) with a magnetic field strength of  $\pm 1$  T. Hall properties were carried out using the van der Pauw method at room temperature, to obtain the carrier concentration, Hall mobility and Hall coefficient. The carrier concentration ( $n$ ) was calculated from the following equation:

$$n = \frac{1}{e R_H} \quad (3.1)$$

where,  $e$  is the charge of the carrier ( $1.6021 \times 10^{-19}$  C) and  $R_H$  is the Hall coefficient

The mobility ( $\mu$ ) was obtained from the following equation:

$$\mu = \frac{1}{e n} \quad (3.2)$$

where,  $n$  is the carrier concentration and  $\sigma$  is the electrical conductivity.

## 3.5. Experimental techniques used for mechanical properties measurements

### 3.5.1. Vickers hardness test

A specific set of the load is applied to an indenter in contact with a material specimen and time duration. After removal of the load, and the area of the impression is measured. The ration between load and the area of indentation is expressed as hardness. The Vickers hardness test comprises of a diamond indenter, in the form of a square pyramid with a base and an angle of  $136^\circ$  between opposite faces and loading

ranges of 1 to 100 kgf. The peak load is generally applied for 10 to 20 dwell seconds. After removal of the load, the diagonals of the square indentation (d1 and d2) are measured using a high-resolution microscope and arithmetic mean (d) is computed. The Vickers hardness is the proportion determined from the following expression,

$$H_v = \frac{2 P \sin \left( \frac{136^\circ}{2} \right)}{d}$$

where, P= Load in kgf and d = Arithmetic mean of the two diagonals, d1 and d2 in mm.

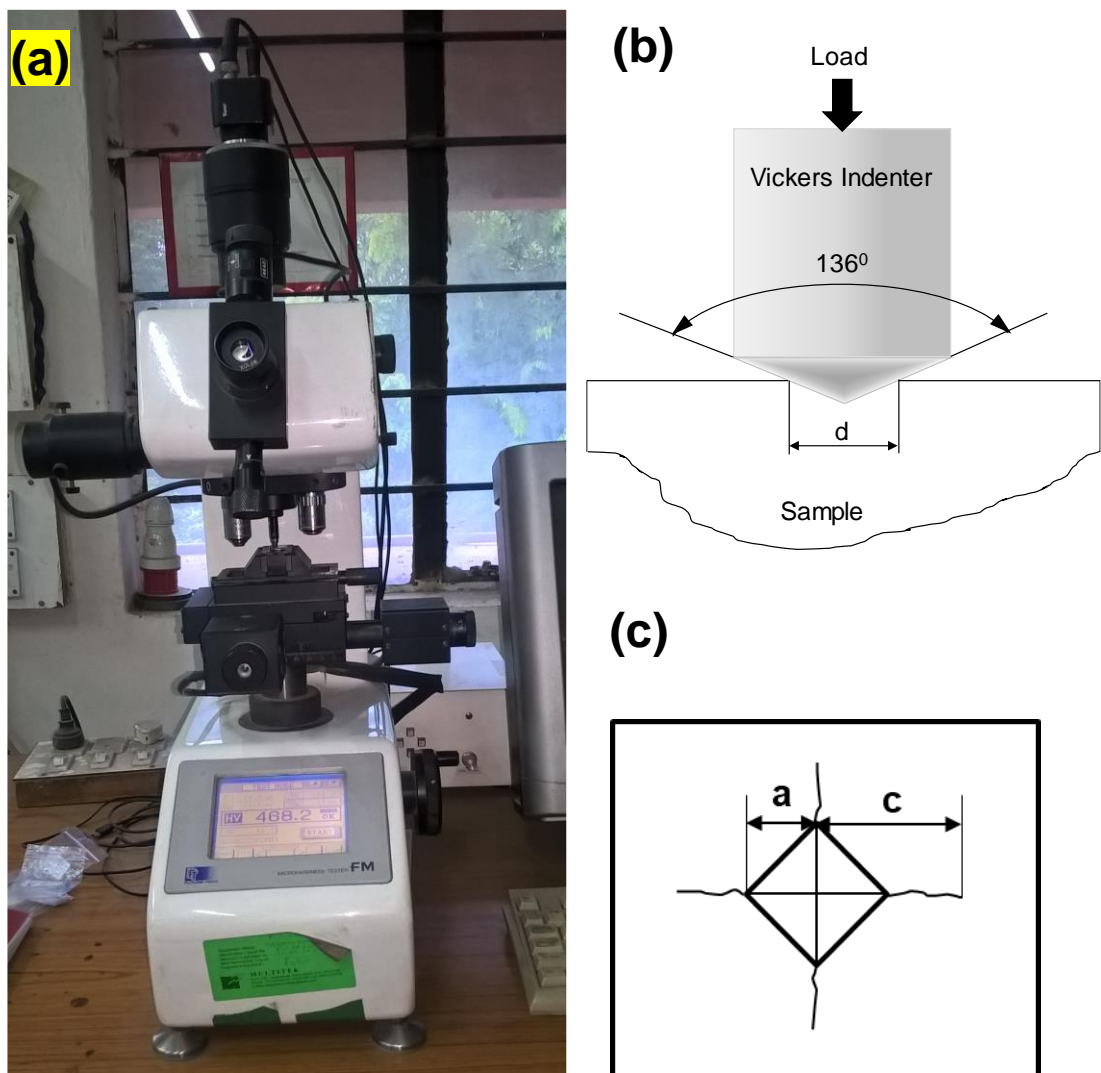


**Figure 3.14. (a) Vickers micro-hardness testing (Future Tech. Corp., FM-e7) used for hardness and fracture toughness measurement and (b) principle of indentation and measurement**

The advantages of the Vickers hardness test is that very accurate measurement is possible and single indenter could be used for all varieties of materials and surface coatings. The slow speed of operation and requirement of the optical high-resolution microscope are the major disadvantages of Vickers hardness technique. For this reason, perpendicular to the indenter axis is a significant factor, as any inclination would give an irregular indentation.

The fracture toughness, as measured by Vicker's indentation crack technique using the equation (1),

$$K_{IC} = 0.0089 \times \left(\frac{E}{H}\right)^{\frac{2}{5}} \times \frac{P}{a l^{1/2}}; \quad 0.25 \leq l/a \leq 2.5 \quad \text{----- (1)}$$

where 'P' is the load, 'l' is the crack length, 'a' is half-diagonal of Vicker's indentation, 'E' is Young's modulus, and 'H' is the hardness. The parameters 'a' & 'l' are measured using a microscope, which is shown in Figure 3.14(c).

### 3.5.2. Nanoindentation test

The standard system of tensile, compressive test measurements may not be possible for evaluating the mechanical strength of small size thermoelectric leg elements. The demand arises to characterize the mechanical properties measurement. Thus the micro & nanoscale testing equipment evolves to solve the problem of developing thermoelectric devices. The nanoindenter is a mechanical microprobe capable of touching the surface of minimum dimensions in a specified level of speed and determining the mechanical properties of the nanoscale. The nanoindenter is developed to apply a prescribed load to a precisely conical shaped indenter in contact with the material surface. The mechanical properties of the material are determined by using load-displacement curve. The technique provides very small mN to nN load range and  $\mu\text{m}$  nm resolution using the precise level actuator, force, and displacement sensors.



There is a tiny impression left in the specimen surface thus, making the technique used for tests on specimens which cannot be tested normal mechanical testing methods. The precise nature of the measurement enables events on the micro to nanoscale to be evaluated. The damage at the macroscale could be interpreted and correlated by events on the nanoscale, therefore fundamental properties of the materials could be examined in detail and tailored for precise applications.

The specimen is subjected to a prescribed load using an indenter tip with contact. The displacement of the indenter is determined with respect to the applied load. The area of contact at peak load is computed by the depth of the imprint and the indenter angle or radius. The hardness determined by dividing the load by the area of contact. The shape of the unloading curve provides a measure of elastic modulus. The schematic of the load-displacement curve is shown in Figure 3.15.

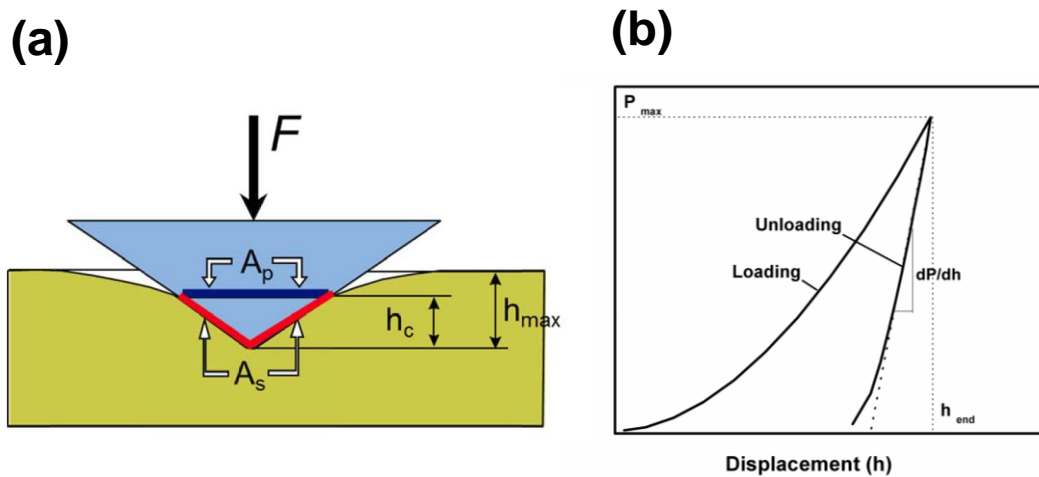


**Figure 3.15. (a) Schematic of nano-indentation method, (b) load-displacement**

The hardness is calculated by the formula

$$H = \frac{P}{A_c}$$

where,  $P_{\max}$  is the maximum indentation load, and  $A_c$  is the contact area of the indentation. The area is calculated from the calibrated indenter tip and is a function of contact depth ( $h_c$ ).

The elastic modulus is calculated by the formula

$$E = \frac{dP}{dh} \frac{1}{2h} \frac{1}{\beta} \sqrt{\frac{\pi}{24.5}}$$

Where,  $\beta = 1.034$  for Berkovich indenter

The nanomechanical characterization of  $Mg_2Si$  and  $MnSi_{1.73}$  is performed by using nanoindentation, based on which the mechanical performance has been discussed in the present study.



**Figure 3.16. Nanoindentation equipment (Fischer-Cripps, Model: IBIS-B, Australia) used for Nanomechanical properties measurement.**

### 3.5.3. Wear and friction test

Wear and friction properties of sintered specimens are estimated using a pin-on-disc sliding wear equipment shown in Figure 3.17 (Make: Ducom, model: TR20). The Ducom wear and friction monitor records friction and wear in sliding contact in dry, lubricated, controlled environment (inert or vacuum conditions). The tribometer is designed for wear and friction analysis of the material as per ASTM standard G-99.

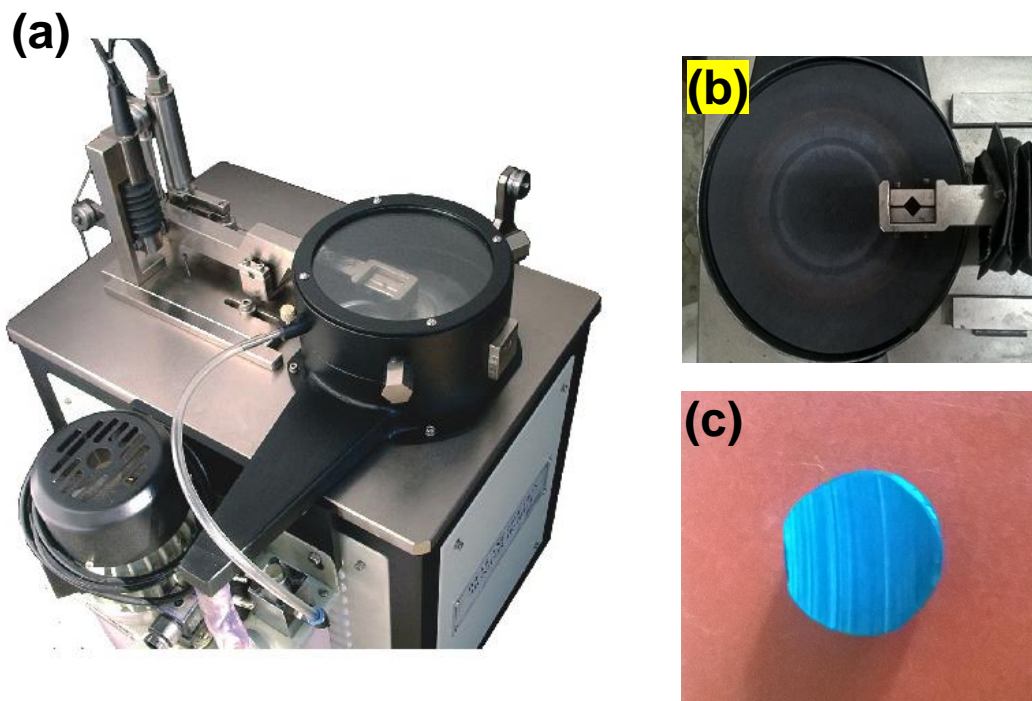


**Figure 3.17. Sliding wear and friction machine (Ducom, Model: TR20LE, India) used for tribological properties measurement, (b) disc and (c) pin specimens used for evaluation**

This instrument has a rotating disc against which a pin material is pressed with a known normal force. The instrumentation and data acquisition provide the information like the speed of the disc, wear in microns and frictional force. The COF ( $\mu$ ) between pin specimens and rotating disc can be continuously recorded through a frictional force transducer (accuracy: 0.1 N) attached to the sliding wear machine. The sliding wear studies of pair materials are commonly evaluated using pin-on-disc configuration. The

pin-on-disc sliding method has more advantages than other wear-friction techniques, and it determines the coefficient of friction and wear properties of dry or wet lubricated surfaces of a variety of bulk materials and coating surfaces with its parent material. The set up contains a cylindrical pin with a flat surface and a circular rotating disk placed at a perpendicular with respect to the cylindrical flat pin surface. This method has some important precautions while testing to ensure an accuracy of the measurements. They are surface finish, cleanliness before and after testing, flat and parallelism of the specimens, sliding speed and applied loads.

Wear tests are performed using sintered  $Mg_2Si$  as a pin material, slides against C-600 emery paper under a different load (10, 30, 50 N) and variable sliding speed (1, 4 and 7 m/s) conditions. The variable sliding speeds were chosen by wind speed simulation in actual hostile conditions [120]. The total sliding distance of 500 meters in each experiment was achieved with varying time. The experiments were repeated three times, and weight loss of a pin was measured using a weighing balance with an accuracy of 0.0001g. The wear rate is calculated using the equation (2) as explained in the article [121,122],  $WR = WL/(\rho \times L)$ . Here,  $W$  = weight loss of a pin (Kg);  $\rho$  = density ( $Kg/m^3$ );  $L$  = sliding distance(m). The wear coefficient is calculated using the generalized Archard Equation (3),  $K = (V \times H)/(P \times L)$ . Here,  $V$  = volume loss of a pin ( $m^3$ );  $H$  = Hardness of the pin (Pa);  $P$  = Load (N);  $L$  = sliding distance (m). The COF ( $\mu$ ) between pin specimen and Disc is recorded through a frictional force transducer for the sliding distance up to 500 m. The friction and wear properties were evaluated under dry sliding conditions as a function of sliding speed and applied normal loads. The worn surface analysis of wear test pin material and disc are carried using field emission scanning electron microscope. The type of wear and wear mechanism of the couple or pairs are analyzed using microstructural studies with elemental mapping analysis.

# CHAPTER 4

Chapter 4 reports the reactive sintering synthesis of undoped and single-doped n-type  $\text{Mg}_2\text{Si}$ , employing spark plasma sintering process. A substantial enhancement in the material's figure-of-merit (ZT)  $\sim 0.56$  was observed, which is due to an enormous increase in its electrical conductivity. The conducting grain boundaries mechanism is proposed to explain these results, wherein the inter-granular electronic conductivity is facilitated by doping elements at grain boundaries, which is supported by microstructural evidence. This chapter also reports the significant enhancement in figure-of-merit of  $\text{Mg}_2\text{Si}$  by a double-doping approach using a combination of Bi, Pb, and Sb as doping elements. The addition of any of the two-doping element combination (Bi, Pb, and Sb) in  $\text{Mg}_2\text{Si}$  increases the electrical conductivity by more than three orders of magnitude, irrespective of the doping elements, although a corresponding decrease in Seebeck coefficient is observed in comparison to undoped  $\text{Mg}_2\text{Si}$ . Irrespective of the combinations of double doping of the elements (Bi, Pb, and Sb), a figure-of-merit (ZT)  $\sim 0.7$  at 873 K is obtained.

## **4.1. Single doped n-type Magnesium Silicide**

### **4.1.2. Introduction**

Green power generation using thermoelectric technology is mainly focussed on the development of thermoelectric materials that are crust abundant for mass production, non-toxic and also thermally stable at the servicing temperatures. Magnesium Silicide ( $\text{Mg}_2\text{Si}$ ) is one such compound that satisfies the above criteria and therefore is a potential thermoelectric material. The material is a covalent semiconductor crystallizing in the cubic anti-fluorite structure. However, experiments reveal that  $\text{Mg}_2\text{Si}$  is a poor thermoelectric material with  $\text{ZT} = 0.1$ . Although, undoped

Mg<sub>2</sub>Si exhibits a small  $ZT$  ( $\approx 0.1$ ), a trace amount of doping improve the  $ZT$  significantly, with significant contribution due to a substantial increase in material's electrical conductivity)[123–130]. Further, the atomic structure of the doping elements and the chemical bonding energy modify the transport properties of the doped Mg<sub>2</sub>Si [123,124,126–129,131–143].

In general, heavily doped degenerated semiconductors behave like metallic systems and their electrical conductivity is expected to decrease at high temperatures due to lattice thermal vibrations. However, such a variation is not observed in the doped Mg<sub>2</sub>Si systems [123,125,128,132]. In these doped systems, at higher temperatures, electrical conductivity appears as an independent temperature quantity [123,132], suggesting a decoupling of the electronic and phonon degrees of freedom. The reported literature indicate that the enhancement of figure-of-merit ( $ZT$ ) in doped Mg<sub>2</sub>Si systems follows not from the material's band structure, but has a probable origin at the grain boundaries [144–146], or may pertain to the case of metallic nano-inclusions [147]. In the present study, a small amount of elemental doping was performed to understand the source of high electrical conductivity and subsequent changes in the thermoelectric transport properties of Mg<sub>2</sub>Si. The single-step reactive spark plasma sintering was employed to process undoped and doped Mg<sub>2</sub>Si. The synthesized Mg<sub>2</sub>Si compounds were investigated using X-ray diffraction for the structural analysis, Transmission electron microscopy for the determination of its microstructure, measurement of temperature dependent variation of thermoelectric transport quantities such as Seebeck coefficient and electrical and thermal conductivities for the thermoelectric performance.

#### **4.1.2. Experimental details**

The proper stoichiometric amount of high purity Mg, Si, and Pb powders were taken and milled in a stainless-steel ball mill with 15:1 ball to powder ratio in an inert

argon atmosphere. The resulting mixed powders filled in a graphite die and punch in the inert glove box and then synthesized in spark plasma sintering at optimized process parameters of 950 -1000 K in vacuum for 10min at a uni-axial pressure of 60MPa. Rectangular samples ( $5 \times 5 \times 2$  mm) were sized from the center of the sintered samples and for X-ray and microstructure analysis. The mirror finish polishing of the samples was performed using fine grade alumina paste in Buehler Disc polisher. The phase structure analysis was performed using monochromatic Copper K-alpha radiation using Rigaku-Miniplex X-ray diffractometer. The microstructural analysis of undoped and doped-Mg<sub>2</sub>Si was carried out using a high-resolution transmission electron microscopy (HRTEM, model: Tecnai G2 F30 STWIN, 300 kV). HRTEM specimen preparation was carried out by using mechanical polishing and subsequent ion beam milling. The mechanical thinning of disc specimen thickness of  $\sim 100$   $\mu\text{m}$  was performed to size about  $\sim 30$   $\mu\text{m}$  by employing a dimple grinder. Ion milling was carried out to make the sample as a beam transparent by using a system at 7 kV and low angle milling. The mild thinning of the sample was performed employing Ar<sup>+</sup> ions for a few minutes. Rectangular samples were sized from the center of the synthesized material for electrical transport properties. The Seebeck coefficient ( $\alpha$ ) and electrical conductivity ( $\sigma$ ) were measured by four probe method using Ulvac-Riko apparatus (Model: ZEM-3) up to 873 K. A disc sample of  $\varnothing$  12.7mm was used for thermal diffusivity measurement employing laser flash apparatus (Make: LINSEIS, Model: LFA 1000). The specific heat ( $C_p$ ) was estimated by Sapphire differential scanning calorimetry method using Netzsch DSC 404 F1. Finally, thermal conductivity ( $\kappa$ ) was calculated from the relation, diffusivity ( $\alpha$ )  $\times$  specific heat ( $C_p$ )  $\times$  density ( $\rho$ ). Figure 4.1 shows the photographs of Spark Plasma Sintering (SPS) technique and reactive sintered specimens of Magnesium Silicides.

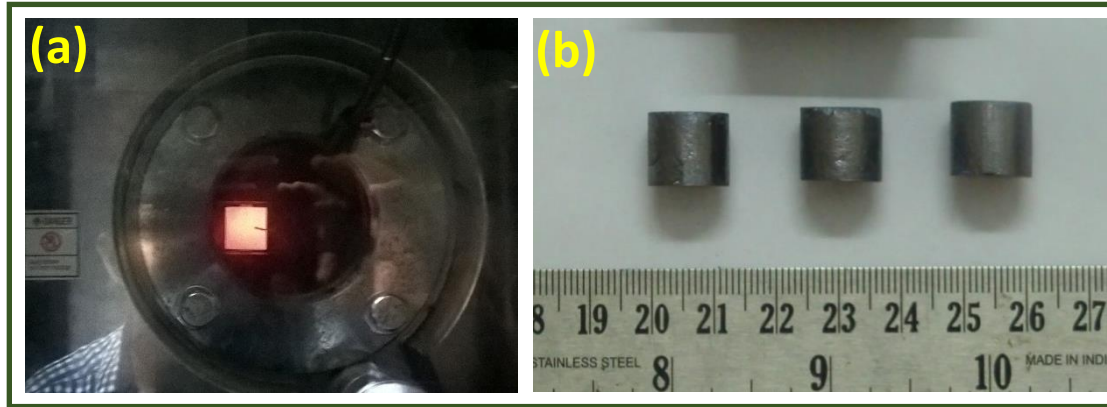


**Figure 4.1.** The photograph showing (a) SPS processing zone while sintering, and (b) SPS synthesized n-type doped  $Mg_2Si$  pellets.

#### 4.1.3. X-ray diffraction Analysis

Figure 4.2 shows the XRD patterns of the as-synthesized and Pb doped  $Mg_2Si$ . The XRD pattern reveals a crystal structure with lattice constants  $\sim 0.636$  nm of the sintered material, which is in good agreement with the available JCPDS data file (No. 00-035-0773).

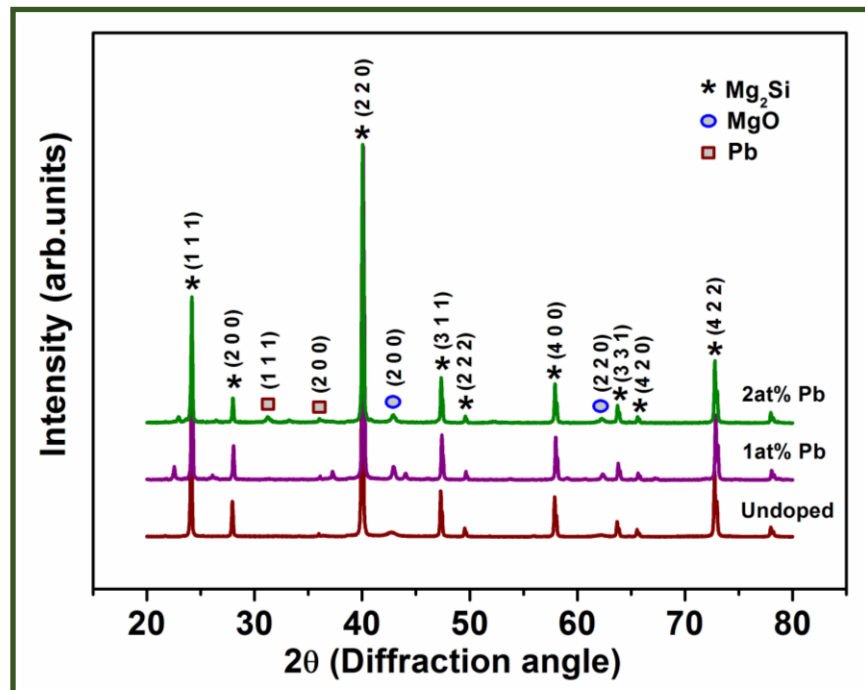


**Figure 4.2.** X-ray powder diffraction pattern of spark plasma sintered undoped, 1at% and 2 at % doped n-type  $Mg_2Si$



XRD analysis shows the trace amounts of MgO presence, which is evolved as a by-product of the Mg sintering process. Even though the sintering process is carried out in high vacuum, a trace amount of MgO is present in the sample due to high volatile nature of Mg. Williamson–Hall method determined the average crystallite size of sintered material was found to be ~55 nm.

#### **4.1.4. Microstructural analysis**

Microstructural investigations of undoped Mg<sub>2</sub>Si and Pb doped-Mg<sub>2</sub>Si were performed using HRTEM, which led to numerous exciting structural features. It was delineated that the undoped Mg<sub>2</sub>Si displays random grain size distribution between 50 to 100 nm uniformly distributed throughout in the microstructure (Figure 4.3(a)). The microstructure of the grains appears globular with an emergence of sub-grains having diffused boundaries between them. Further magnified the image of individual grains reveal that the sub-grains separated with an ultra-fine short length interfaces without any significant contrast related to that of surrounding grains (Figure 4.3(b)). The size of sub-grains varies between 5 to 10 nm. However, the atomic scale imaging on grains encompassing several such sub-grains indicated that the grains consisted of well-defined crystallographic planes of FCC lattice by our XRD and earlier reports. Figure 4.3(c) shows that the grains are constituted of 220 planes (d-spacing  $\equiv$  0.22 nm) of a cubic structure. It was also noted that the sub-grain boundaries are generally continuous in the alignment of crystallographic planes with very little disturbance at the interfaces. As an illustrative example, Figure 4.3(d) shows that the 220 planes are present throughout the grain with a nominal irregularity of atomic planes at the interfaces (surrounded by a set of dotted lines) between the two sub-grains. It is also reflected that the 200 planes (d-spacing  $\equiv$  0.31 nm) having an angular separation of about 45° with the 220 planes is present, which is an obvious angular relationship between the two

coexisting planes (220 and 200) in a cubic structure. It was seen that the grains and sub-grains are overlapped quite often leading to a complex microstructure at an atomic scale. In Figure 4.3, such an interesting arrangement of 220 set of atomic planes with an intrusion of 311 planes (d-spacing = 0.19 nm) in a localized region is clearly indicated in the micrograph (Figure 4.3). It is further observed that the overlap of different planes leads to an evolution of moiré patterns (the region marked by a white dashed line and labeled as A in Figure 4.3). A fast Fourier transform (FFT) of these atomic planes constituting the grain microstructure further delineates the presence of 220 and 311 planes in reciprocal space (inset in Figure 4.3).

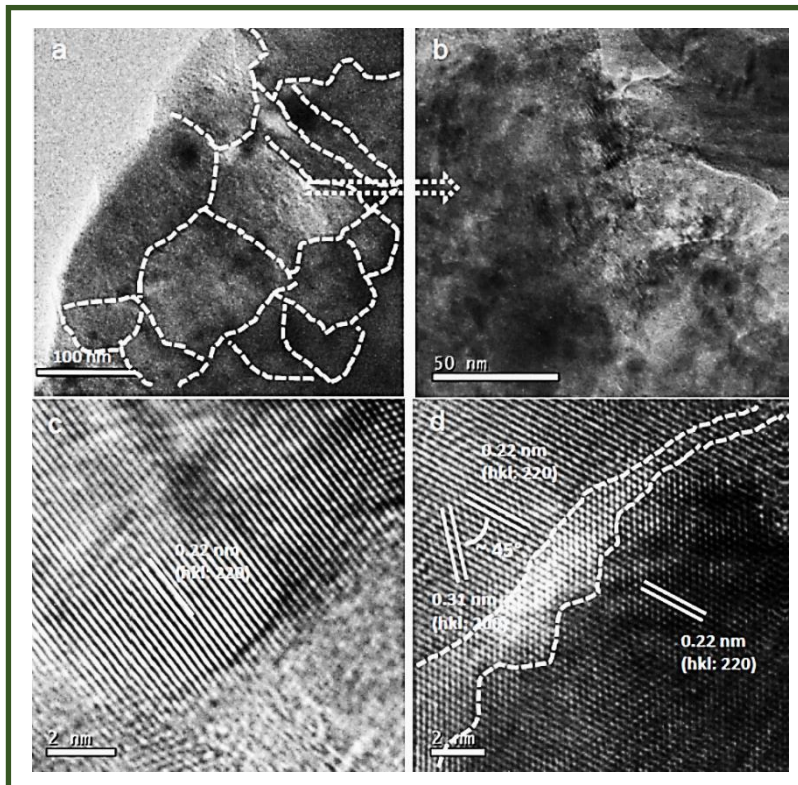


**Figure 4.3. HR-TEM microstructures of SPS processed magnesium silicide exhibiting (a) the grains distribution, (b) a magnified view of Mg<sub>2</sub>Si grains, (c) an atomic lattice scale image, and (d) a grain boundary**

Figure 4.4 exhibits a set of high-resolution electron micrographs recorded from the Pb doped-Mg<sub>2</sub>Si system, which suggests some subtle changes, as compared to

undoped-Mg<sub>2</sub>Si. The grain sizes noticed in case of Pb doped-Mg<sub>2</sub>Si specimen are relatively finer with a minimum grain size of  $\approx 20$  nm (Figure 4.4(a)), and the largest size  $\approx 70 - 80$  nm. Moreover, the sub-grain interfaces within individual grains are quite visible with an average size of sub-grains  $\approx 5 - 10$  nm (Figure 4.4(b)). The grain boundary, as marked between the two grains (magnified regions I and II of Figure 4.4(a)), reveals that there is no significant distortion, porosity or any other type of defect at the grain boundary (Figure 4.4(b)). Atomic-scale imaging performed at a triple boundary junction (marked with three arrows) collectively on few sub-grains shows the presence of the planes 111 (d-spacing  $\equiv 0.36$  nm) and 200 (d-spacing  $\equiv 0.31$  nm). The sub-grain boundaries marked with a set of arrows distinguishes these ultra-fine features among each other (Figure 4.4(c)).

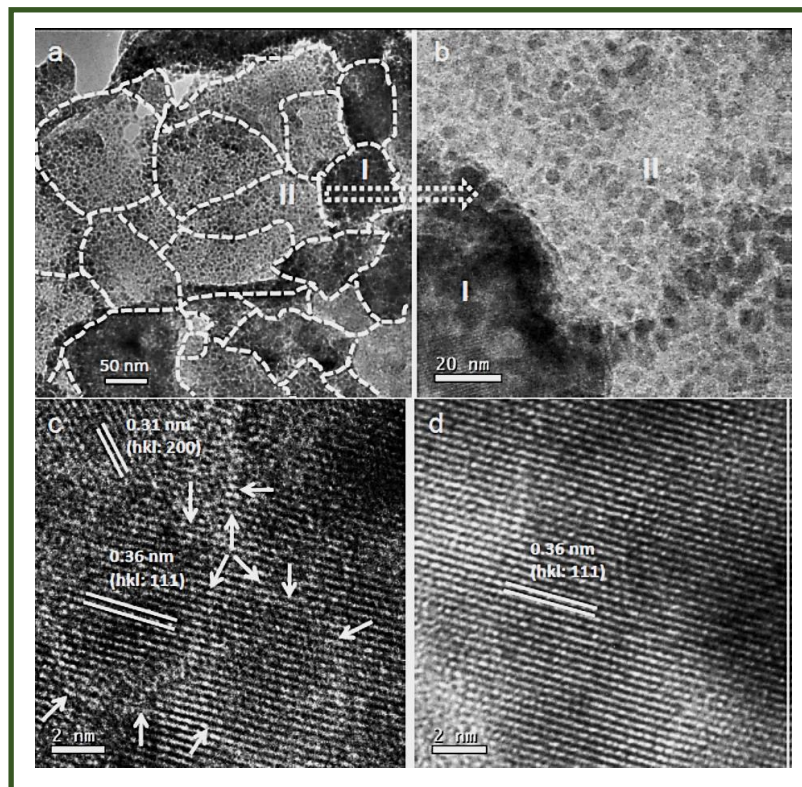


**Figure 4.4.** HR-TEM microstructures of single element doped Mg<sub>2</sub>Si exhibiting (a) grains distribution, (b) a magnified view of Mg<sub>2</sub>Si grains and subgrains, (c) an atomic lattice scale image at a junction, and (d) Doped Mg<sub>2</sub>Si grain at atomic scale

It is also noticeable that except some minor disruptions at the sub-grain boundaries interfaces, there is a continuity of crystallographic planes throughout the grains (Figure 4.4(d)) without any orientation differences between the two sub-grains. In most of the cases, the grains are crystalline with uniformity in the crystallographic planes (Figure 4.4(d)).

Although for the Pb doped system, the sub-grain size is almost same as in undoped  $\text{Mg}_2\text{Si}$ , it is evident from the HRTEM analysis that the boundaries around sub-grains are quite distinct in the former compared to undoped  $\text{Mg}_2\text{Si}$ . Evidence of distinct boundaries around sub-grains is presumably due to composition variation in and around sub-grains. Although there is no detailed electron spectroscopy carried out to determine the composition of ultra-thin short length sub-grain boundaries. It is known that such metallurgical phenomena are possible in case of the samples where a parent composition ( $\text{Mg}_2\text{Si}$ ) is doped with an element (Pb) in such a way that the excess Pb in the form  $\text{Pb}/\text{Mg}_2\text{Pb}$  decorates the boundaries around the grain-matrix to have a uniform stable microstructure.

A thorough TEM examination of the Pb doped  $\text{Mg}_2\text{Si}$  has led some evidence of trapping of  $\text{Mg}_2\text{Pb}$  inclusions of dimensions approximately 5 to 6 nm (labeled as A with marked white dashed line) in the  $\text{Mg}_2\text{Si}$  matrix in Figure 4.5. In addition to the variations in the crystallographic configurations, in and around sub-grain boundaries, the disparity in the compositional patterning of sub-grain boundaries would lead to sub-grain structure more prominent in case of Pb doped  $\text{Mg}_2\text{Si}$ . These observations evidence to grain boundary accumulation of Pb (or  $\text{Mg}_2\text{Pb}$  phases), thereby opening inter-granular conducting paths, substantiating the enormous increase in electrical conductivity in Pb doped  $\text{Mg}_2\text{Si}$  system, which is consistent with the brick-layer model of electronic conduction discussed earlier [144–146].

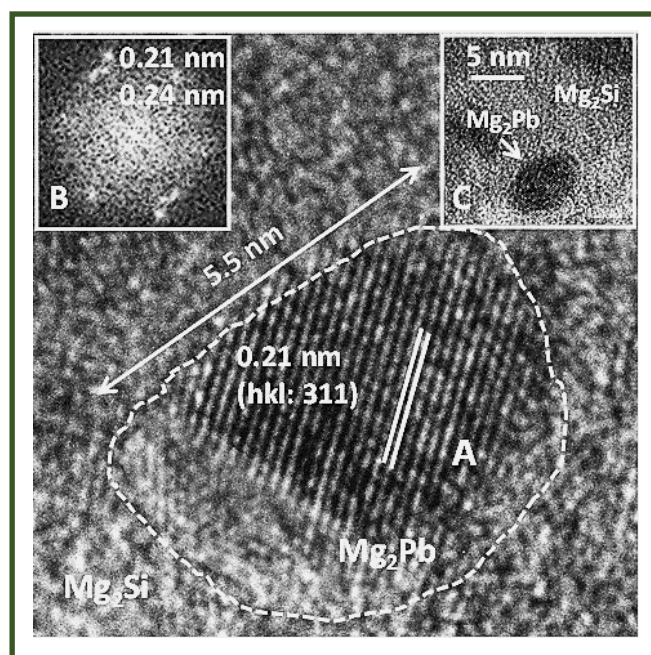


**Figure 4.5.** HR-TEM microstructure of single doped  $\text{Mg}_2\text{Si}$  material showing the evidence of  $\text{Mg}_2\text{Pb}$  particles in the  $\text{Mg}_2\text{Si}$  matrix. FFT (inset (b)) reveals the cubic  $\text{Mg}_2\text{Pb}$  crystal structure. Inset(c) reveals  $\text{Mg}_2\text{Pb}$  nano-particle at low magnification microstructure.

#### 4.1.5. Thermoelectric properties

##### 4.1.5.1. Electronic transport properties

Figure 4.6(a-d) shows the thermoelectric transport properties of undoped and Pb doped  $\text{Mg}_2\text{Si}$  concerning to temperature increase. It is apparent from this figure that irrespective of nature of the dopant, the overall characteristics of the temperature dependence of their thermoelectric transport parameters appears qualitatively similar. However, substitution of Pb at Si site of  $\text{Mg}_2\text{Si}$ , resulting in significant enhancement of electrical conductivity (Figure 4.6(a)). The improvement in electrical conductivity ( $\sigma$ ) by three orders of magnitude for 2 at% of Pb dopant more than the undoped system (at 300 K) not related to the conventional electrical conduction mechanisms. Such an enormous increase in electrical conductivity with respect to the undoped  $\text{Mg}_2\text{Si}$  system is observed not only for Pb doping but has been reported for all other dopants in  $\text{Mg}_2\text{Si}$

except Te [131]. It may be further noted from Figure 4.6(a) that, in comparison with the earlier reports in the literature of electron doping, the electrical conductivity of Pb ( $\approx 18 \times 10^3$  S/m at 823 K) is found to be much higher than Te doped Mg<sub>2</sub>Si ( $\approx 6.4 \times 10^3$  S/m at 823 K) [131], however, lower than that of Sb and Bi-doped Mg<sub>2</sub>Si ( $\approx 80 \times 10^3$  S/m at 860 K) [123,132]. Findings from our XRD and EDAX measurements suggest that there is no excess Mg or Si non-stoichiometry in our Pb doped Mg<sub>2</sub>Si system. The large increase in conductivity, in the present studies, could have two origins: (i) Segregation of Pb at the grain boundaries and (ii) formation of isostructural, isoelectronic and metallic Mg<sub>2</sub>Pb phases which act as nano-inclusions in the Mg<sub>2</sub>Si semiconducting matrix. The latter enhances the transport properties by band bending effects, due to the mismatch in their respective Fermi energies. The negative polarity of Seebeck coefficient (Figure 4.6(b)), at all temperatures, for both, undoped and Pb doped Mg<sub>2</sub>Si, indicates an *n-type* conduction in this thermoelectric material. The magnitude of Seebeck coefficient of our Pb doped Mg<sub>2</sub>Si decreases with Pb doping, which can be supported with the inverse relation of Seebeck coefficient with increasing carrier concentration, as given by the Cutler-Mott equation [120].

#### **4.1.5.2. Thermal transport properties**

The temperature dependence of the total thermal conductivity (Figure 4.6(c)), which confirms only a minimal reduction in the magnitude of thermal conductivity with Pb doping in Mg<sub>2</sub>Si. Decomposing thermal conductivity ( $\kappa$ ) into its electronic and lattice contributions using the Lorenz number  $L = 2.45 \times 10^{-8} \text{ W}\Omega\text{K}^{-2}$ , an increase in electronic thermal conductivity has been found with the increase in total thermal conductivity for Pb doped Mg<sub>2</sub>Si, in comparison with the undoped counterpart. This observation implies a decrease in lattice thermal conductivity ( $\kappa_{\text{lat}}$ ) for the Pb doped system. This decrease in  $\kappa_{\text{lat}}$  is quite expected, as with Pb doping increases the

distribution of heavy and light atoms in the system. However, the assumption of a constant value of Lorentz number, for both undoped and Pb doped  $\text{Mg}_2\text{Si}$ , may not be very appropriate. Typically, the Lorentz number ( $L$ ) in degenerate semiconductors has a strong dependency on materials parameters, such as dimensionality, hybridization, doping concentration and the position of Fermi energy in the materials electronic structure [148–151].

#### 4.1.5.3. Figure-of-merit (ZT)

The calculated figure-of-merit and power factor are shown in figure 4.6. The power factor for  $\text{Mg}_2\text{Si}$  is  $7.2 \times 10^{-5} \text{ W/mK}^2$  at 823 K, while after 2 at% Pb it enhances to  $163 \times 10^{-5} \text{ W/mK}^2$  at 623 K.

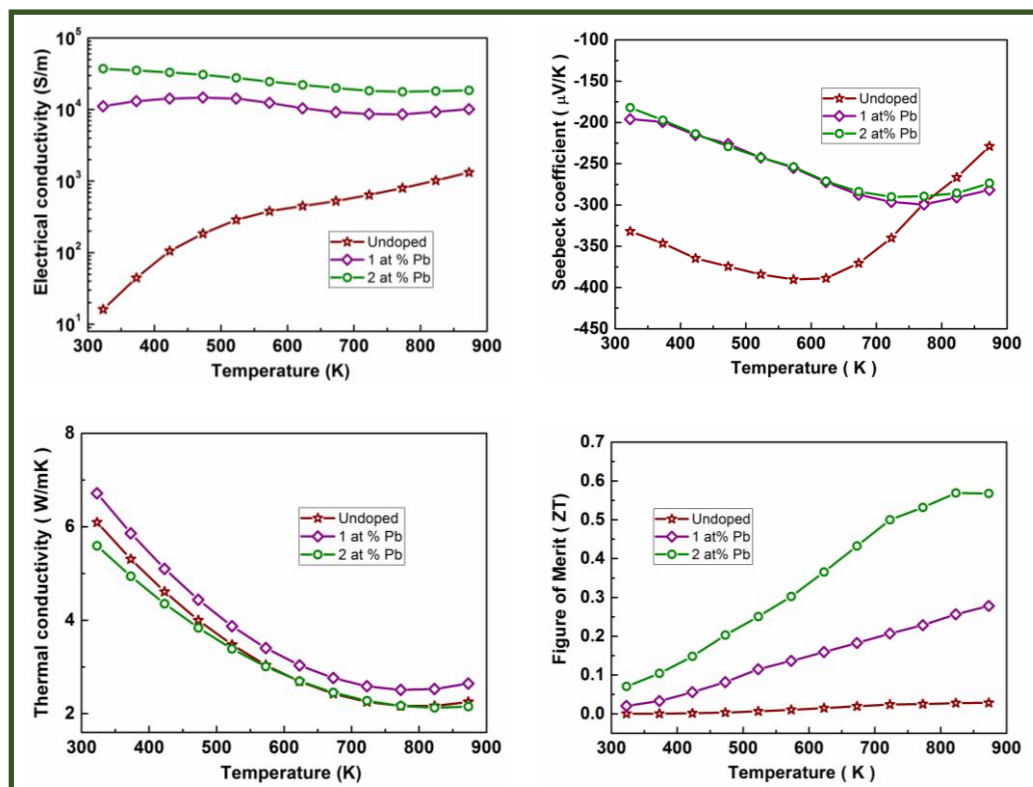


**Figure 4.6.** Thermoelectric properties of undoped and single doped  $\text{Mg}_2\text{Si}$ . (a) electrical conductivity, (b) Seebeck coefficient, (c) thermal conductivity, (d) figure-of-merit (ZT).

There is a decrease in Seebeck coefficient value with Pb doping, albeit it is the significant improvement in electrical conductivity that plays a critical role in the enhancement of power factor by order of magnitude. Figure 4.6(d) shows the dimensionless figure-of-merit ( $ZT$ ) for undoped and Pb doped  $Mg_2Si$  samples. It is observed that the figure-of-merit ( $ZT$ ) of all the Pb doped  $Mg_2Si$  increase with increasing temperature. An optimum  $ZT$  of 0.56 is obtained at 873 K for 2 at% Pb doped  $Mg_2Si$ , which is similar to Sb-doped  $Mg_2Si$  but lower than Bi-doped  $Mg_2Si$ . As evident from the temperature dependence of thermoelectric properties (Figure 4.6), the key factors that govern the enhancement of figure-of-merit follows from the material's composite-like structure.

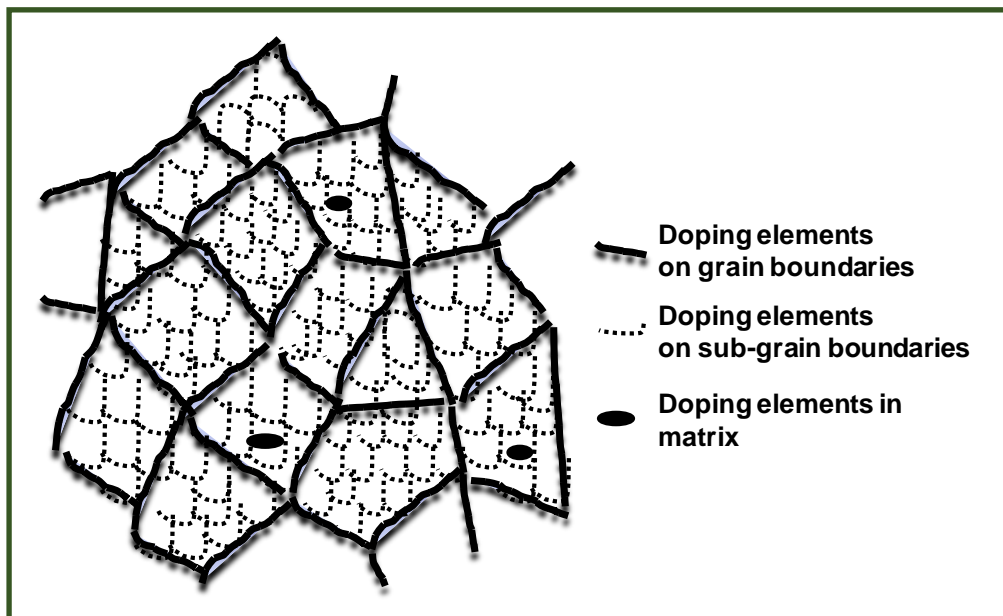


**Figure 4.7. Schematic representation of grain & grain boundary model of synthesized doped  $Mg_2Si$**

A detailed characterization of the structure of a doped  $Mg_2Si$  system using electron microscopy reveals the presence of homogeneous grains and subgrains of varying size across the sample, as per schematic model is shown in Figure 4.11. The doping elements are tending to segregate to the grain boundaries (GBs), due to the low



solubility in the matrix materials [152,153]. The dopant is at such a high concentration, and it forms a second phase, which could lead grain boundaries as donors of electrons. The variations in the crystallographic configurations, in and around sub-grain boundaries, the disparity in the compositional patterning of sub-grain boundaries would lead to sub-grain structure more prominent in doped Mg<sub>2</sub>Si. The grain boundary accumulation of doping elements makes opening inter-granular conducting paths, leads to an enormous increase in electrical conductivity in the doped Mg<sub>2</sub>Si system, which is consistent with the brick-layer model of electronic conduction [154]. Further, the process of adding dopants to nanocrystalline materials is a well-recognized way of mitigating the effect of coarsening[152,153,155]. Dopant atoms act as strong barrier walls, migrating to grain boundaries and neutralizing the free energies[153]. The process of adding selective dopants to nanocrystalline materials is a one of the best way of controlling the coarsening effects, able to retain the grain growth [152,153,155]. Further, the nanocrystalline structure is preserved by strong grain boundary barriers, improve the mechanical properties of the materials, leads to additional benefit for the development of Mg<sub>2</sub>Si based thermoelectric materials.

#### **4.1.6. Conclusions**

In the present study, Magnesium Silicide was synthesized using a single-step reactive spark plasma sintering technique, by the addition of Pb doping at different atomic percentage levels. A significant figure-of-merit (*ZT*) enhancement,  $\approx 0.56$  at a temperature of 873 K, is achieved in single doping approach. Although a decrease in thermal conductivity and Seebeck coefficient values is observed for Pb doping in Mg<sub>2</sub>Si, a significant improvement in the thermoelectric figure-of-merit is gained. The enhancement in figure-of-merit (*ZT*) for the case of single Pb doping in Mg<sub>2</sub>Si is mainly due to the increase in its electronic conductivity. Also, the Pb doped Mg<sub>2</sub>Si exhibits an

increase in its electronic conductivity at par with dopants with electron donors. A detailed cross-examination of the materials microstructure, using HRTEM, evidence to Pb (or Mg<sub>2</sub>Pb) phases at the grain boundaries, facilitating inter-granular conductivity and thereby suggesting an electronic conducting mechanism. The present study has proposed the importance and role of grain boundaries in doped Mg<sub>2</sub>Si systems, which are potential thermoelectric materials.

## **4.2. Double doped n-type Magnesium Silicide**

### **4.2.1. Introduction**

The specific conversion efficiency of Mg<sub>2</sub>Si and the earth's crust abundance of constituent elements, and hence their reduced material cost, benefits over the other thermoelectric material. Doping of Mg<sub>2</sub>Si with different elements, both *n-type* and *p-type*, was reported to improve the figure-of-merit. Investigations on Mg<sub>2</sub>Si have shown that the group VA periodic table elements doping in Mg<sub>2</sub>Si show the improved thermoelectric properties compared to other elements, including rare earth materials. In the present study, processing of *n-type* double-doped Mg<sub>2</sub>Si was performed by proper mixing of Mg, Si, Bi, Sb, and Pb in the suitable chemical stoichiometric weight using a reactive spark plasma sintering technique. The sintering conditions, such as applying pressure, holding temperature, the rate of heating, and holding duration, were optimized to deliver a dense single-phase material.

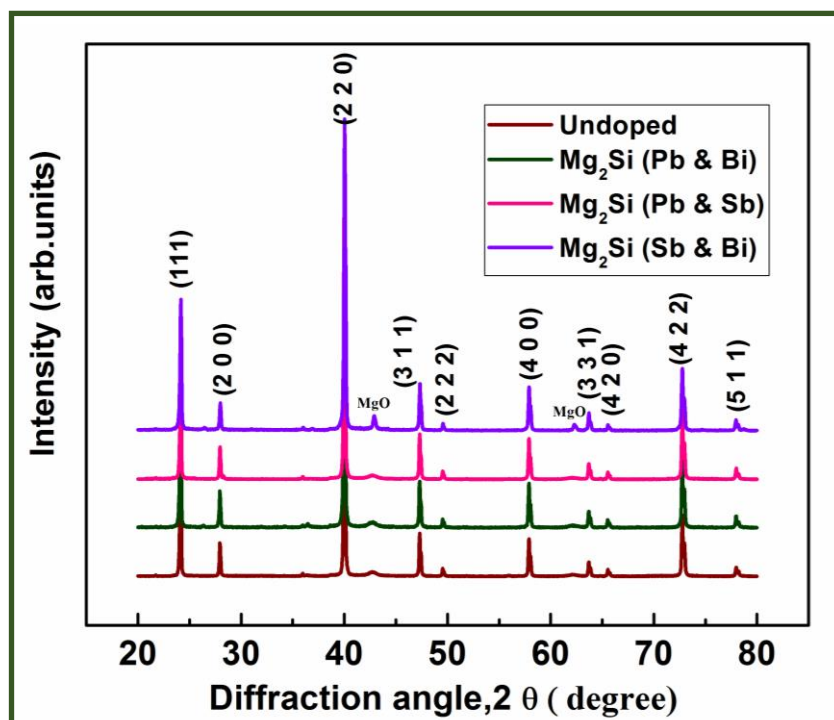
The synthesized double-doped Mg<sub>2</sub>Si samples were analyzed using X-ray diffraction, electron microscopy attached with energy dispersive spectroscopy, for determination of its phase purity, chemical stoichiometric composition, and microstructure. The thermoelectric properties of these double-doped Mg<sub>2</sub>Si were carried out using Linseis LFA 1000 and Ulvac-ZEM 3. The transport properties of synthesized double-doped Mg<sub>2</sub>Si materials were correlated with the undoped Mg<sub>2</sub>Si. It was

confirmed that doping of any two of the elements Sb, Bi, and Pb to Mg<sub>2</sub>Si improved its electrical conductivity, albeit a reduction in the value of Seebeck coefficient.

#### **4.2.2. Experimental details**

The proper chemical stoichiometric proportions of high purity Mg, Si, Pb, Sb and Bi powders were taken and, these powders were mixed in a stainless steel ball mill (Fritsch, Pulverisette-4) ball to powder ratio of 15:1 in an inert argon filled bowls. Loading and unloading of the ball milled mixed powders was carried out in the glove box (Mbraun, MB20) to prevent environmental contamination and oxidation. The resulting alloyed powders are sintered in spark plasma sintering (SPS 725) at 990-1050 K in a vacuum (~ 4 Pa) for 10 minutes at a uni-axial pressure of 60 MPa in a high-strength graphite die. The density value of the sintered samples obtained is more than 99 % of the theoretical value. X-ray diffraction (XRD) analysis was performed using monochromatic Copper-K alpha radiation using X-ray diffractometer (RigaKu-make Miniflex-II). The microstructural analysis of undoped and doped-Mg<sub>2</sub>Si was performed using an electron microscopy and an EDS (Make: Oxford, Model: SDD X-Max) system. The rectangular specimens were sized from the center of the synthesized material using wire cut saw (Model: 515 CE, South Bay Technology) for the Seebeck coefficient and electrical conductivity measurements. The electrical conductivity and Seebeck coefficient were measured by four probe DC method using Ulvac-Riko apparatus (Model: ZEM-3) up to 873 K. A disc sample of  $\varnothing$  12.7mm was used for thermal diffusivity measurement employing laser flash apparatus (Make: LINSEIS, Model: LFA 1000). The specific heat ( $C_p$ ) was estimated by Sapphire differential scanning calorimetry method using Netzsch DSC 404 F1. Finally, thermal conductivity ( $\kappa$ ) was calculated from the relation, diffusivity ( $\alpha$ )  $\times$  specific heat ( $C_p$ )  $\times$  density ( $\rho$ ).

### 4.2.3. X-ray diffraction Analysis



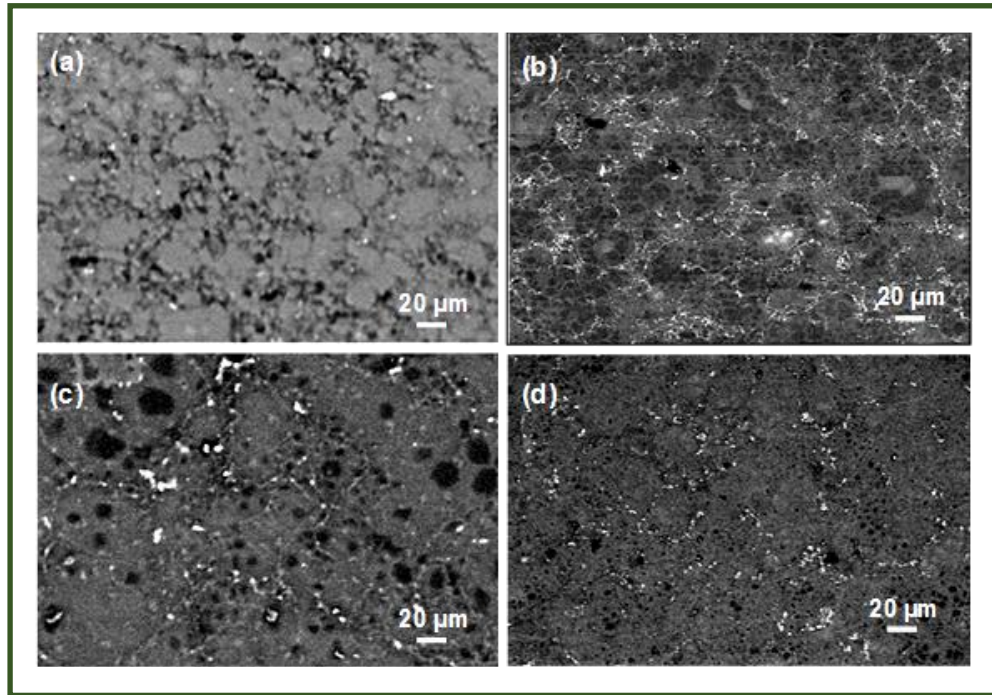
**Figure 4.8.** The X-ray powder diffraction pattern of spark plasma sintered (a) undoped, (b) Pb and Bi-doped, (c) Pb and Sb-doped, and (d) Sb and Bi-doped

Figure 4.7 exhibits the XRD patterns of the spark plasma sintered undoped and double-doped Mg<sub>2</sub>Si. XRD analysis of the samples shows the presence of trace amounts of MgO, which is evolved as a compound of the synthesizing process and has also been reported in previous studies of Mg<sub>2</sub>Si. A trace amount of MgO is present in the sample due to highly volatile and oxygen affinity nature of Mg. Apart from MgO, no other impurities were noticed in XRD patterns.

### 4.2.4. Microstructural analysis

Figure 4.8(a-d) shows the scanning electron microscopy images of spark plasma sintered undoped and double doped Mg<sub>2</sub>Si. The white contrast regions reveal the presence of dopant-rich grain boundaries. The undoped Mg<sub>2</sub>Si image (Figure 4.8(a))

shows the random distribution of grains and grain boundaries with no distinct. The doped  $\text{Mg}_2\text{Si}$  images (Figure 4(b-d)) delineates a fine-grained microstructure with distinct grain boundaries, irrespective of the doping elements.



**Figure 4.9. SEM images of sintered  $\text{Mg}_2\text{Si}$ . (a) undoped, (b) Pb and Sb-doped, (c) Pb and Bi-doped, and (d) Sb and Bi-doped.**

The overall grain size distribution of spark plasma sintered undoped and doped  $\text{Mg}_2\text{Si}$  appears to be uniform. Evidence of distinct boundaries around the grains is possibly due to composition variation in and around sub-grains. The surface morphology of the doped  $\text{Mg}_2\text{Si}$  evidence distinct grain with ultrathin boundaries of different compositional materials. The EDS spectrum analysis confirms that the dopants are partly diffused into the grains and remaining segregated into the grain boundaries. The substantial improvement of electrical conductivity of double-doped  $\text{Mg}_2\text{Si}$  is possibly due to the incorporation of semiconducting dopants, which is organizing the distinct, fine-grained microstructure.

## 4.2.5. Thermoelectric properties

### 4.2.5.1. Electronic transport properties

Figures 4.9 & 4.10 shows the temperature dependence electrical conductivity of double-doped  $Mg_2Si$ . The electrical conductivity of doped  $Mg_2Si$  results in high electrical conductivity which is  $\sim 60$  times higher in comparison to the undoped  $Mg_2Si$  at a temperature of 873 K. At 873 K, the electrical conductivity value of double-doped increases from 1327 (undoped) to 60000 S/m (Pb & Sb), shows metallic conduction behavior. Furthermore, the electrical conductivity of double-doped  $Mg_2Si$  is found to be much higher than that of single doped  $Mg_2Si$  with Te, Al & Y [125,128,131]. One can observe the metallic conductivity behavior occurs in the double-doped  $Mg_2Si$ , whereas undoped  $Mg_2Si$  shows the semiconducting behavior. The metallic inclusions in  $Mg_2Si$  participate in the substantial improvement of electrical conductivity of double-doped  $Mg_2Si$  system.

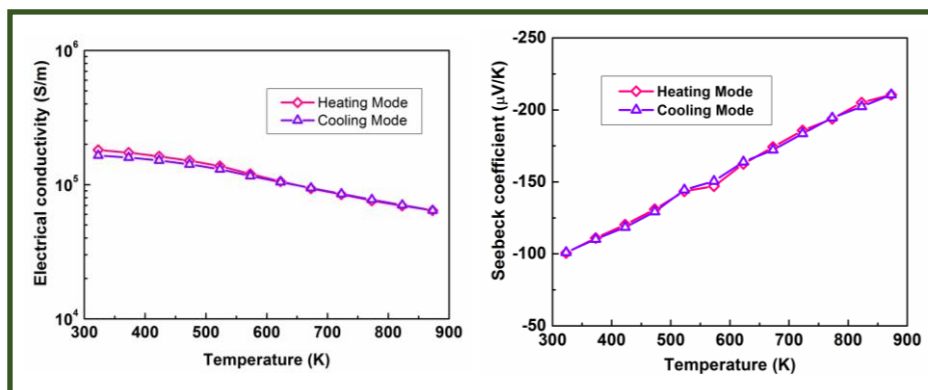


**Figure 4.10. Temperature dependence of (a) the electrical conductivity and (b) the Seebeck coefficient of double-doped  $Mg_2Si$  during heating and cooling.**

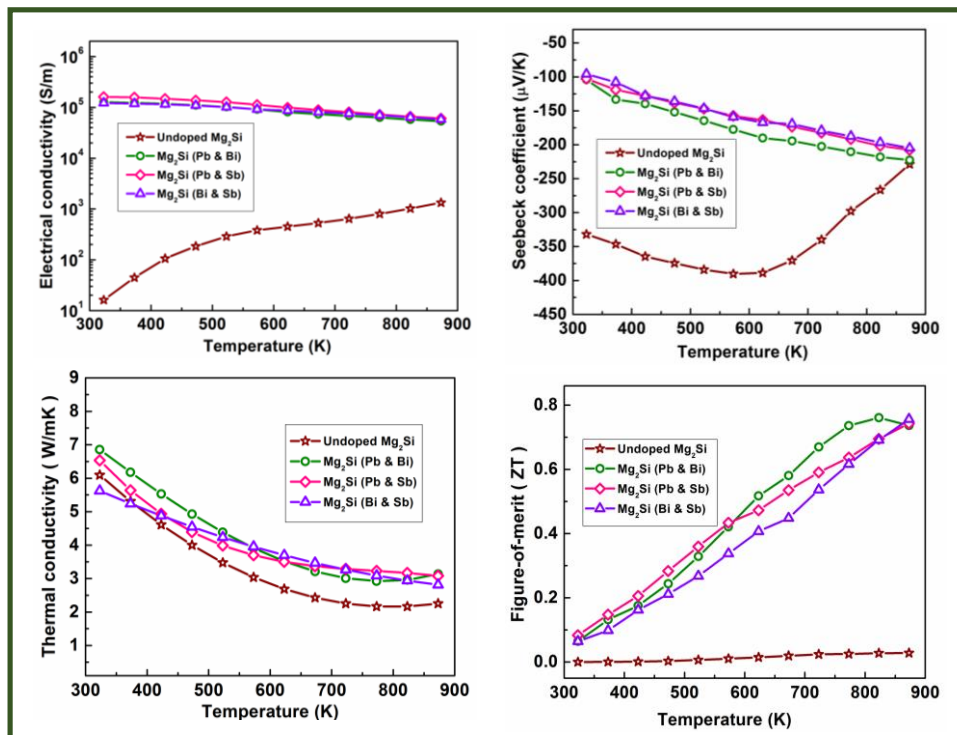
### 4.2.5.2. Thermal transport properties

Figure 4.10(c) shows the thermal conductivity of undoped and double-doped  $Mg_2Si$  as a function of temperature. At 323 K, the thermal conductivity value in undoped  $Mg_2Si$  is ( $\sim 6$  W/mK) is a lesser value than that of double-doped  $Mg_2Si$  ( $\sim 7$

W/mK). At 873 K, the thermal conductivity value in undoped  $Mg_2Si$  is ( $\sim 2.2$  W/mK) is comparably lower than that of double-doped  $Mg_2Si$  ( $\sim 3$  W/mK). It was observed that the small addition of semiconducting dopants does not alter the thermal transport properties of  $Mg_2Si$ .

#### 4.2.5.3. Figure-of-merit

Figure 4.10(c) shows the temperature dependence power factor of undoped and double-doped  $Mg_2Si$ . The power factor of undoped  $Mg_2Si$  indicates the peak value of  $6.9 \times 10^{-5}$  W/mK<sup>2</sup> at 873 K and double-doped  $Mg_2Si$  shows a peak value of  $262 \times 10^{-5}$  W/mK<sup>2</sup>. While there is a decrease in Seebeck coefficient ( $\alpha$ ) value, the high order increase in electrical conductivity ( $\sigma$ ) offers a substantial enhancement of power factor ( $\alpha^2\sigma$ ). The results confirm that nearly a similar power factor value is gained from the Pb, Sb & Bi double-doping combination  $Mg_2Si$ .



**Figure 4.11.** Temperature dependence of undoped and double-doped  $Mg_2Si$  (a) electrical conductivity, (b) Seebeck coefficient, (c) thermal conductivity, (d) figure-of-merit (ZT).

Figure 4.10(d) exhibits the calculated values of the figure-of-merit ( $ZT$ ) for undoped and double-doped  $Mg_2Si$  samples. For the undoped and double-doped  $Mg_2Si$ , the value of figure-of-merit increases with increase in temperature, in the measured range 323 K- 873 K. At 873 K, the value of  $ZT$  increases from  $\sim 0.03$  for the undoped sample to  $\simeq 0.7$  for Pb & Sb-doped  $Mg_2Si$ . The double doping in  $Mg_2Si$  studies confirms the enhancement of  $ZT$ . This improvement is attributed due to electronic contribution in double-doped  $Mg_2Si$ .

#### **4.2.6. Conclusions**

The double-doped  $Mg_2Si$  was synthesized employing in-situ reaction, spark plasma sintering technique by using Bi, Pb and Sb combination as doping elements in the appropriate stoichiometric ratio. The phase crystal structure, chemical composition, elemental distribution, and surface morphology of the double-doped  $Mg_2Si$  was performed employing X-ray diffraction, electron microscopy, and energy dispersive spectroscopy analysis. The substantial improvement of the thermoelectric figure-of-merit of  $Mg_2Si$  was obtained by double-doping Bi, Pb, and Sb combination as doping elements. Elemental doping of any two of these three materials to  $Mg_2Si$  improves the electrical conductivity by more than three orders of magnitude, irrespective of the doping elements used. However, an equivalent reduction in the Seebeck coefficient value is obtained in comparison with an undoped  $Mg_2Si$  counterpart. The significant thermoelectric figure-of-merit of  $\sim 0.7$  at 873 K is gained irrespective of three elements combination used for double-doping in  $Mg_2Si$ ; this is primarily because of improvement of the electrical conductivity.



# CHAPTER 5

Chapter 5 deals with the facile synthesis of Al-doped MnSi<sub>1.73</sub>, a HMS phase (p-type), employing a single-step plasma assisted reactive sintering process, which consumes only a few minutes as compared to long processing hours using conventional manufacturing techniques. In spite of using this simple and cost-effective material synthesis technique, a figure-of-merit (ZT) ~ 0.65 was observed in Aluminium doped MnSi<sub>1.73</sub>. This Chapter also reports the synthesis of nanostructured HMS with enhanced thermoelectric performance, employing melt spinning combined with spark plasma sintering technique. Employing this methodology, which is both efficient and scalable, an unprecedented figure-of-merit (ZT) ~ 0.8 at 800 K was realized in Al-doped MnSi<sub>1.73</sub>, synthesized at optimized process parameters. The phase purity, elemental distribution, morphology, and structure was examined using X-ray diffraction, high-resolution electron microscopy and energy dispersive spectroscopy, based on which the thermoelectric performance of p-type MnSi<sub>1.73</sub> has been discussed.

## 5.1. Bulk p-type Higher Manganese Silicides

### 5.1.1. Introduction

Higher Manganese Silicides (HMS) are an inimitable family of intermetallic compounds that are regarded as potential thermoelectric materials, due to their earth-abundant and environmentally-friendly constituent elements coupled with high oxidation resistance. In addition, HMS are the excellent *p-type* compatible counterpart to the *n-type* Mg<sub>2</sub>Si-based thermoelectric material thereby leading to efficient thermoelectric generators [43–45,75,156,157]. However, HMS synthesis is having the difficulties due to its thin line of composition variation in the Mn-Si phase diagram [106]. The Mn & Si sublattices form a chimney ladder composition of the tetragonal

crystal structure with almost equal  $a$  lattice parameters and unusually long  $c$  lattice parameters [104,158]. A narrow variation in Mn-Si composition exhibits a several HMS phases, such as,  $\text{Mn}_4\text{Si}_7$  ( $\text{MnSi}_{1.75}$ ),  $\text{Mn}_{27}\text{Si}_{47}$  ( $\text{MnSi}_{1.74}$ ),  $\text{Mn}_{15}\text{Si}_{26}$  ( $\text{MnSi}_{1.73}$ ), and  $\text{Mn}_{11}\text{Si}_{19}$  ( $\text{MnSi}_{1.72}$ ) [103,105]. The HMS phases are Nowotny Chimney-ladder phases and show tetragonal crystal structure with same  $a$ -axis and an elongated  $c$ -axis (Figure 5.1), and hence differentiation of phases is challenging [103,105]. The unique structural complexity nature of higher manganese silicide offered by long lattice periods (four distinct NCL tetragonal phases with same  $a$  lattice and different  $c$  lattice parameters 1.75, 4.81, 6.53 and 11.8 nm), would be beneficial for lowering lattice thermal conductivity without disturbing the electrical conductivity. The band gaps ranging from 0.4 to 0.9 eV have been reported with a small difference in composition and thus alter the electronic transport properties of the processed HMS. Microstructural point of view, the grain size reduction of HMS offers a reduction of thermal conductivity nearly half of the value to the bulk counterpart.

The several studies on HMS were reported employing liquid metallurgy processing routes, arc melting [50–52,110], and melt spinning [107,109,159]. The powder metallurgy route of HMS synthesis employing mechanical alloying followed by powder compaction was reported, either using hot pressing or spark plasma sintering (SPS) [108,111–115,160]. However, experimentally it is challenging to control the particular composition of HMS phase due to the low vapor pressure of Mn and loss of Si during processing associated with melting temperature difference. Also, HMS is not the eutectic composition in Mn-Si phase diagram and therefore to synthesize the precise HMS composition is challenging, employing melting processes. During the synthesis of HMS, the high-temperature melting in liquid metallurgy process and extended hours of ball milling and long durations of sintering in powder metallurgy process impart to a

different chemical stoichiometry of final synthesized HMS. Thus, the compositional control in HMS experiences its variation in phase structure, which accounts for the large scatter in their reported thermoelectric properties.

The doping with Al [109], Ge [51], Cr [111], CNTs [115], SiGe [50] and double/triple doping (Ge, Mo, W, Al) [161] on HMS was also reported and showed an enhancement in thermoelectric properties. The high melting point of constituent elements (Mn ~ 1510 K & Si ~ 1685 K), the high vapor pressure of Mn and compositional control in the final product are the major challenges for bulk scaling up HMS at the industrial level. The SPS process sinter the material at lower temperatures than conventional methods and in shorter duration since the powders are heated rapidly by the spark plasma, which has a surface activation effect on the powders being sintered. SPS is a uniaxial pressure associated reaction sintering process, and hence rapid sintering rates over bulk sample volumes can be achieved [71,162].

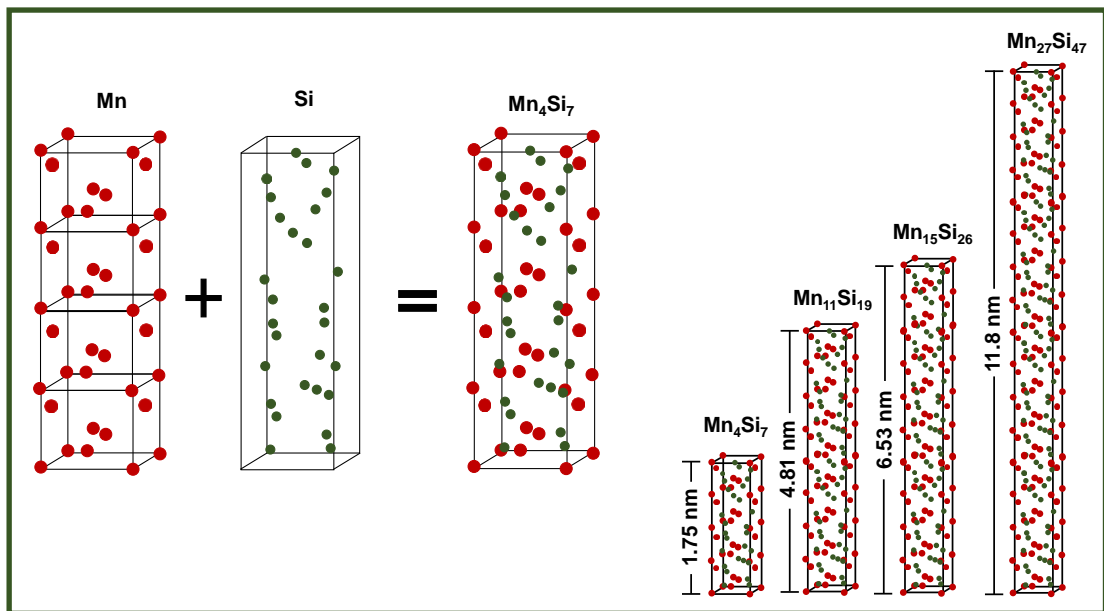


**Figure 5.1. Crystal structures of higher manganese silicides showing different tetragonal phases  $Mn_4Si_7$ ,  $Mn_{11}Si_{19}$ ,  $Mn_{15}Si_{26}$ , and  $Mn_{27}Si_{47}$ , with same lattice constant 'a' of ~ 0.552 nm and different lattice constants 'c' of ~ 1.75, 4.81, 6.53 and 11.8 nm, respectively**

In the present study, the undoped and Al-doped HMS ( $\text{MnSi}_{1.73}$ ), was synthesized using a single-step reactive sintering process employing Spark plasma sintering (SPS). The low thermal conductivity ( $\sim 1.7 \text{ W/mK}$ ) exhibits an excellent thermoelectric performance of the sintered HMS, which gains from the low crystallite value (120-150 nm) of the material, synthesized using the spark plasma reactive assisted sintering process. In this process, the in-situ reaction between the Mn and Si powders and their consequent sintering occurs in a single step, and therefore the synthesis consumes only small-time duration as compared to long hours processing duration employing conventional fabrication techniques. The synthesized HMS samples were characterized for crystal structure, chemical composition and microstructure using X-ray diffraction (XRD), high-resolution electron microscopy and energy dispersive spectroscopy (EDS).

### **5.1.2. Experimental details**

High purity Mn, Si, Al powders were blended in proper weight and stoichiometric proportion in a ball mill. The mixed powders were unloaded in the inert atmosphere glove box (Model: MB20, Make: Mbraun, Germany) to avoid oxidation and other environmental contamination. The well-mixed powders were filled in the high strength graphite die and sintered using reactive spark plasma sintering (Model: SPS-725, Make: Japan) at 1173 K for 10 minutes applying 60 MPa uniaxial pressure under vacuum. Archimedes principle determined the SPS processed materials' density. The XRD analysis was performed using monochromatic  $\text{Cu-K}\alpha$  radiation using Rigaku-make XRD (Miniflex-II). FESEM (Make: Zeiss, Germany, Model: SUPRA V40) attached with EDS was employed to study the surface morphology and chemical composition of the SPSed HMS samples. The HR-TEM (Tecnai G2 F30 STWIN, 300

kV) was used to characterize the atomic scale microstructural features of the sintered HMS samples.

Rectangular samples of  $\text{MnSi}_{1.73}$  were machined from the center of the sintered samples for the evaluation of Seebeck coefficient and electrical conductivity, using Ulvac-ZEM3 apparatus. A disc sample of  $\varnothing$  12.7mm was used for thermal diffusivity measurement employing laser flash apparatus (Make: LINSEIS, Model: LFA 1000). The specific heat ( $C_p$ ) was estimated by Sapphire differential scanning calorimetry method using Netzsch DSC 404 F1. Finally, thermal conductivity ( $\kappa$ ) was calculated from the relation, diffusivity ( $\alpha$ )  $\times$  specific heat ( $C_p$ )  $\times$  density ( $\rho$ ).

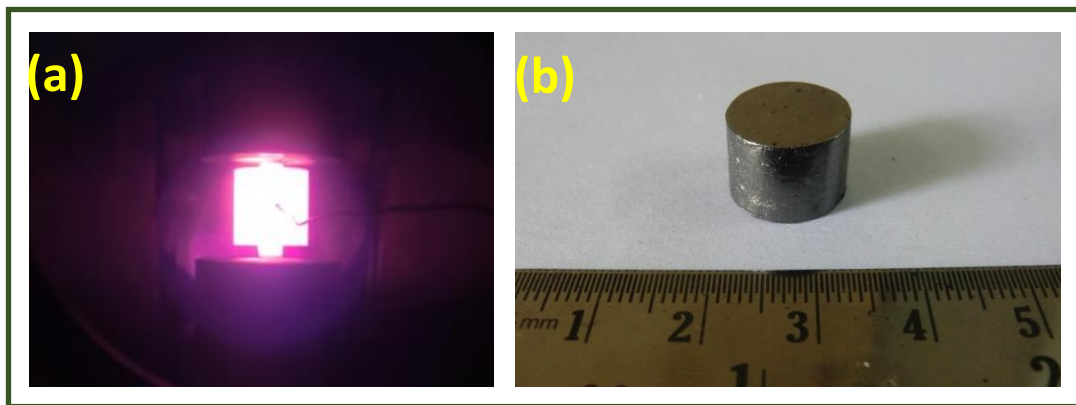


**Figure 5.2.** The photograph showing (a) SPS processing zone while sintering, and (b) SPS synthesized p-type doped  $\text{MnSi}_{1.73}$  pellets.

### 5.1.3. X-ray diffraction Analysis

X-ray diffraction analysis was performed on the synthesized material on a Rigaku diffractometer with Cu  $K\alpha$  radiation of wavelength 1.54 Å at a scan speed of  $4^\circ \text{ min}^{-1}$  with a  $2\theta$  range of  $20\text{--}80^\circ$ . The recorded XRD patterns, shown in Figure 5.3, revealed that higher manganese silicide phase ( $\text{Mn}_{15}\text{Si}_{26}$ ) and the values are close agreement with the reported JCPDS data file (No. 00-020-0724). The lattice parameters of tetragonal structure ( $a = 0.55$ ,  $b = 0.55$ , and  $c = 6.55$  nm) are similar to the HMS

phase ( $\text{Mn}_{15}\text{Si}_{26}$ ). Addition of Al does not make the apparent change in the lattice parameters. The small peak in XRD analysis shows the presence of primary Si-phase, but it is devoid of metallic cubic-MnSi phase, which is an unexpected compound in the synthesis of HMS [112–114] and is identified to degrade the thermoelectric properties.

#### 5.1.4. Microstructural analysis

Figure 5.4 & 5.5 shows the scanning electron microstructures, and corresponding elemental mappings of SPS processed HMS and Al-doped HMS, respectively. The microstructure distinguishes the difference occurred in the both sintered materials.

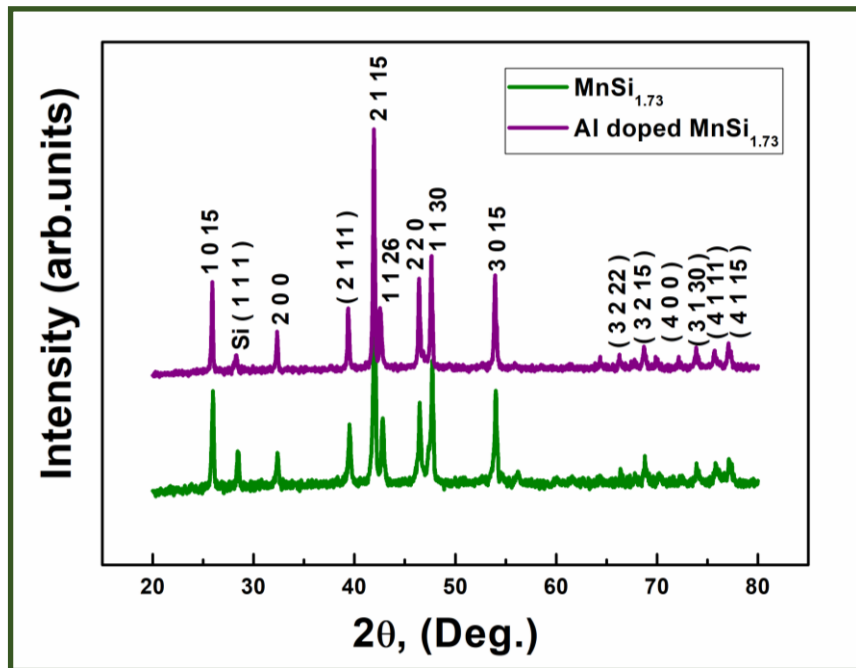


**Figure 5.3. X-ray powder diffraction pattern of spark plasma sintered undoped and Al-doped  $\text{MnSi}_{1.73}$**

The primary silicon particles are visible in Figure 5.4, and Electron Dispersive Spectroscopy (EDS) analysis evidences the existence of primary silicon with HMS phase. The element-specific EDS mappings confirm that the primary Si phase is rich in the HMS sample. Similarly, the presence of  $\sim 10 \mu\text{m}$  primary silicon particles in HMS

matrix was reported by Sadia & Gelbstein [108], in hot pressed specimens. The elemental maps of the synthesized  $\text{MnSi}_{1.73}$  sample show an almost even dispersion of Mn, Si & Al (Figure 5.5) and the inset shows the EDS spectrum of the elements. These results suggest that the chemical composition of the sintered HMS sample is near similar to the HMS stoichiometry. There are no apparent grain and grain boundaries visible in the present microstructural analysis.

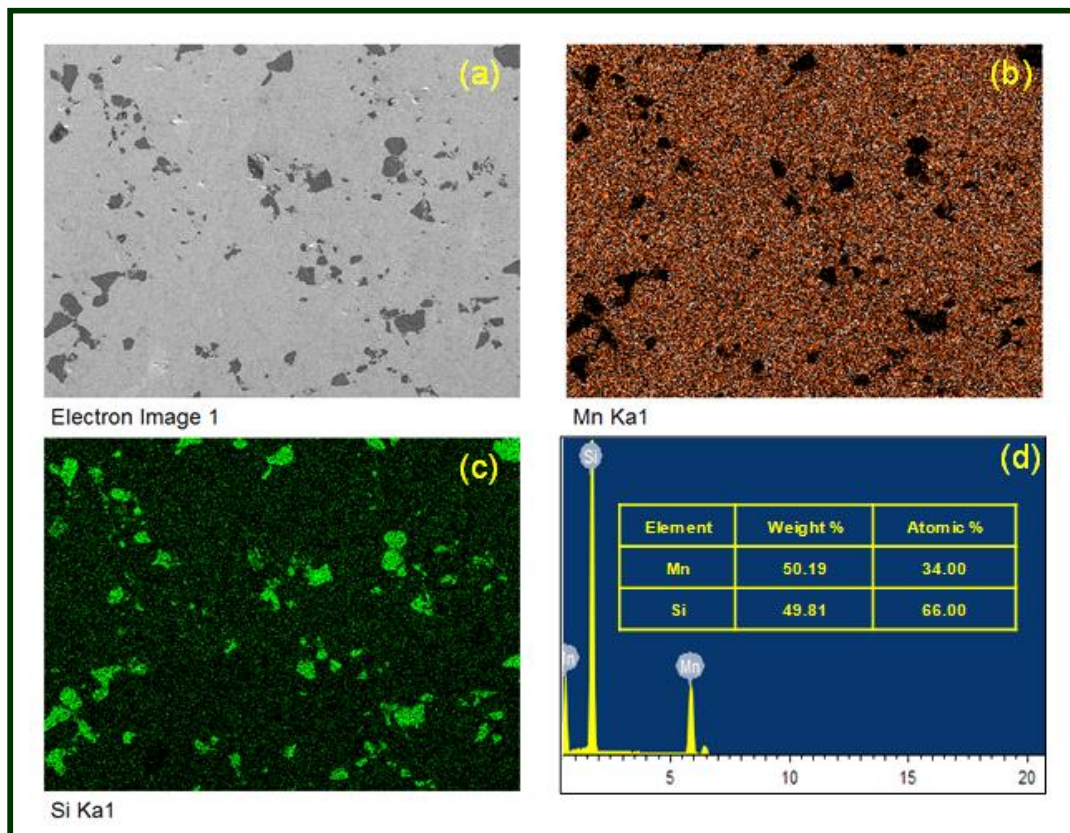


**Figure 5.4. SEM images of (a) SPS processed HMS ( $\text{MnSi}_{1.73}$ ), and showing the individual elemental maps of (b) Mn, (c) Si and (d) EDS spectrum.**

However, Si-rich HMS phase with primary Si particles shows the similarity of the earlier studies on HMS [108]. The examination of the structure of the material evidences  $\text{Mn}_{15}\text{Si}_{26}$  HMS phases irrespective of the compositions used, and the elemental mapping shows the uniform distribution of Mn & Si in the SPS processed material. The small variation in initial stoichiometric alters the microstructural features

and transport properties of the sintered material. The fast reaction kinetics with enhanced diffusion process of the SPS technique imparts the quick and rapid formation of higher manganese silicide phase ( $Mn_{15}Si_{26}$ ). Further, FESEM microstructure analysis confirms the existence of an extra primary Si-phase, but it is devoid of the metallic cubic-MnSi phase, which is an unexpected compound in the synthesis of HMS [112–114] and is identified to degrade the thermoelectric properties.

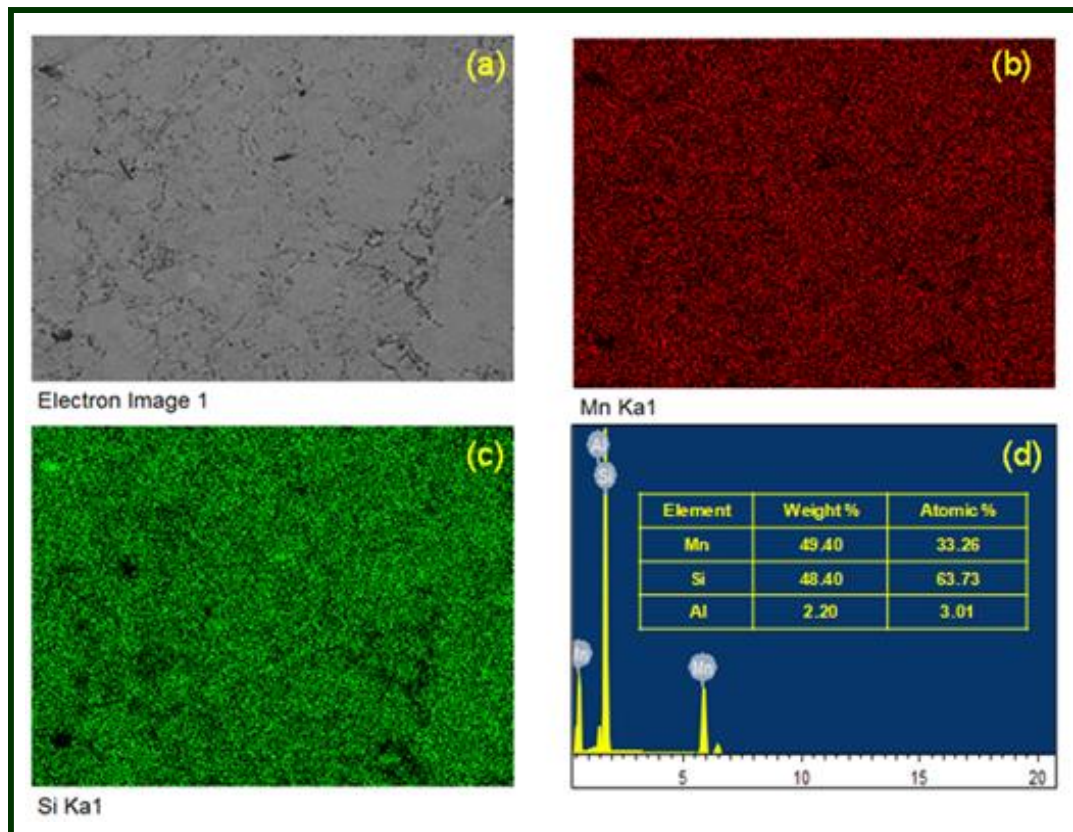


**Figure 5.5.** SEM images of (a) SPS processed Al-doped HMS ( $MnSi_{1.73}$ ) sample, and showing the individual elemental maps of (b) Mn, (c) Si and (d) EDS spectrum

HR-TEM analysis was performed on the synthesized  $MnSi_{1.73}$  sample to elucidate the microstructural features in real and reciprocal space. Figure 5.6(a) shows a TEM microstructure, which exhibits the ultrafine microstructure with grains in the range  $\sim 120 - 150$  nm. It is inferred that the individual grains show excellent crystallinity, which is apparent from the TEM microstructures (Figure 5.6 (b) & (c)).

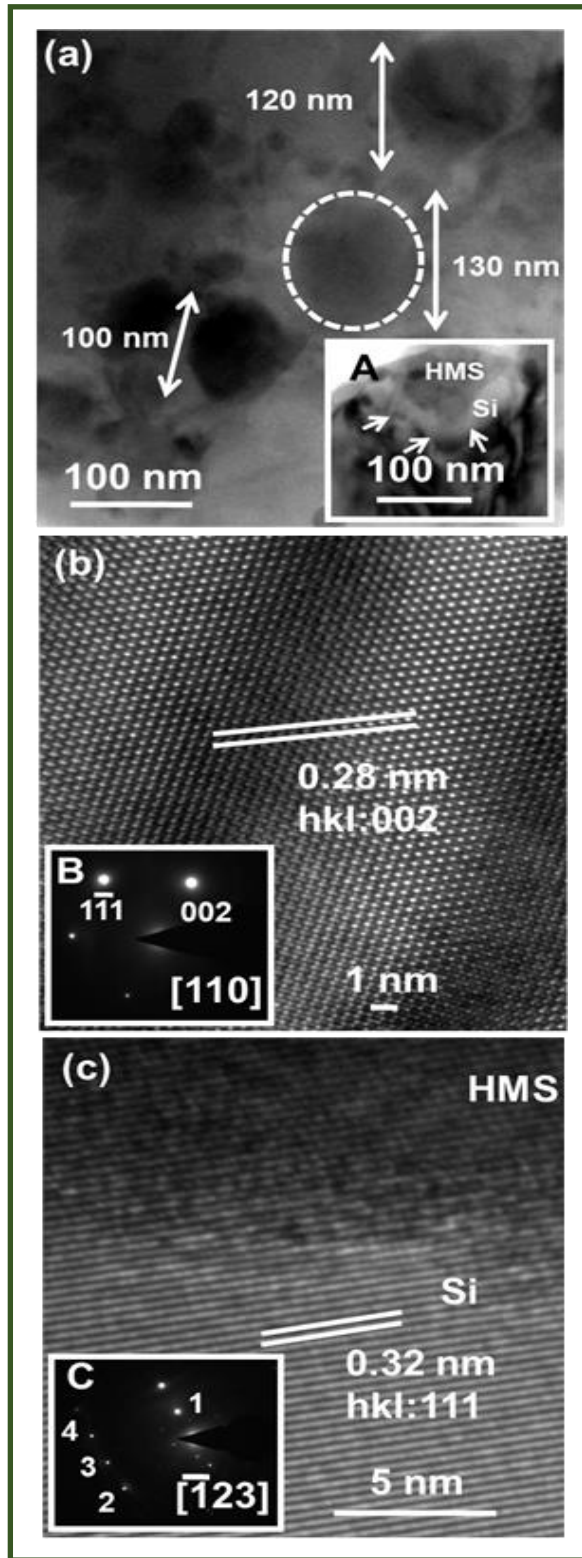


Figure 5.6 (b), which shows the image of a typical 130 nm grain in lattice scale (encircled region with dotted line in Figure 5.6 (a)), evidences of atomic planes along hkl:002 with atomic spacing of 0.28 nm of the tetragonal structure of  $\text{MnSi}_{1.73}$  ( $\text{Mn}_{15}\text{Si}_{26}$ , tetragonal, space group:  $\bar{I}4\bar{2}d$ , lattice parameters:  $a=0.55$ ,  $b=0.55$ ,  $c=6.56$  nm, JCPDS no.: 00-020-0724). The inset in Figure 5.6(b) reveals a selected area electron diffraction pattern (SAEDP) captured along  $[110]$  zone axis of a tetragonal phase structure of  $\text{MnSi}_{1.73}$  sample. A set of planes, hkl: 002 and  $1\bar{1}1$  are also marked on the selected area electron diffraction pattern in the reciprocal space. The lattice image (Figure 5.6(c)) shows the existence of extra Si, surrounding the HMS grains. The inset in Figure 5.6(a) elucidates a microstructure of a  $\text{MnSi}_{1.73}$  grain with the existence of primary Si (light grey contrast around the periphery marked with dotted lines). An atomic-scale image (Figure 5.6(c)) exhibits distinct atomic planes of Si with the planar spacing of 0.32 nm (hkl:111, Si cubic crystal structure) stacked along at the interface of  $\text{MnSi}_{1.73}$ . The SAEDP captured from a rich region of Si along  $[\bar{1}23]$  zone axis elucidates a crystal structure of Si with important diffracted planes, hkl:  $\bar{1}\bar{1}\bar{1}$ ,  $\bar{2}\bar{4}\bar{2}$ ,  $\bar{3}\bar{3}\bar{1}$ ,  $\bar{4}\bar{2}\bar{0}$ , marked on an inset C in Figure 5.6(c)). The HRTEM analysis confirms the formation of HMS ( $\text{MnSi}_{1.73}$  phase) with grain sizes ~120-150 nm, with a small amount of primary Si, although devoid of cubic MnSi phase.

### **5.1.5. Thermoelectric properties**

#### **5.1.5.1. Electronic transport properties**

Figure 5.7(a) & 5.8(a) show the electrical conductivity values of the synthesized undoped and Al-doped  $\text{MnSi}_{1.73}$  concerning temperature variation. The Seebeck coefficient (Figure 5.7(a) & 5.8(a)) increases with increasing temperature from ~134  $\mu\text{V/K}$  at 323K & ~128  $\mu\text{V/K}$  at 323K. The highest value of Seebeck coefficient was found to be ~ 236  $\mu\text{V/K}$  at 773 K & ~ 211  $\mu\text{V/K}$  at 773 K, respectively.



**Figure 5.6.** HR-TEM microstructures of Al-doped HMS ( $\text{MnSi}_{1.73}$ ) revealing (a) grains distribution, (b) atomic scale image, and (c) atomic scale image of HMS with extra primary silicon. Insets: (A) Si and HMS grain, (B) diffraction pattern of HMS grain, and (c) diffraction pattern of silicon.

Beyond the 773 K, slight decrease trend is observed, attributed to electrons excitation across the band gap. The observed temperature dependence Seebeck coefficient is quite similar in behavior and magnitude to the HMS reported studies [50,51,107,109,111–114]. The positive values of Seebeck coefficient observed in the complete temperature range show the p-type conduction in the synthesized HMS material. The electrical conductivity (Figure 5.7(a) & 5.8(a)) shows a constant decrease with temperature increase and saturate at high temperatures ( $\sim 2 \times 10^4$  S/m for undoped &  $\sim 3 \times 10^4$  S/m for Al-doped). This behavior is characteristic of degeneration in semiconductor, and the values are close to the reported doped HMS phase earlier with Al [109], Ge [51] and CNT[115]. Figure 5.7(c) & 5.8(c), which shows the electronic part (power factor ( $\alpha^2 \sigma$ )) of the processed HMS sample, exhibits the power factor value  $\sim 1.12 \times 10^{-3}$  W/mK<sup>2</sup> at 873 K for undoped and  $\sim 1.28 \times 10^{-3}$  W/mK<sup>2</sup> at 873 K for Al-doped HMS, which is equivalent to earlier reported studies [51,112].

#### **5.1.5.2. Thermal transport properties**

Figures 5.7(b) & 5.8(b) shows the temperature dependence of the total thermal conductivity of undoped and Al-doped HMS. It is evident from the figures that the thermal conductivity confirms the value of  $\sim 2.6$  W/mK for undoped and  $\sim 1.7$  W/mK for Al-doped HMS, at 873 K. The lattice thermal conductivity, as shown in Figure 5.7(b) & 5.8(b) was calculated from the total thermal conductivity by subtracting the electronic contribution, considering the Lorentz number  $2.45 \times 10^{-8}$  W $\Omega$ K<sup>-2</sup>. It is evident from the figure that the lattice thermal conductivity has a significant role for total thermal conductivity reduction, which mostly can be achieved by numerous type of microstructural modifications in the material, including refining its crystallite size. The thermoelectric materials, such as, PbTe [163], PbSeTe [164] and Si [165], thermal transport takes place by phonons of mid and long wavelength [1,2,166,167]. Therefore

the mesoscale structures are anticipated to perform a leading role in reducing the lattice part conductivity, owing to scattering of phonons [28,167]. The synthesized HMS  $\text{MnSi}_{1.73}$  samples, the crystallite size was obtained to be 120-150 nm range, (from HR-TEM studies).

Thus, the decrease in thermal conductivity in the spark plasma sintered samples could mainly be attributed to the phonons scattering of mid and long wavelength by the mesoscale crystallites, which provide a high density of grain boundaries making to a large amount of grain boundaries participation in the scattering process. The low crystallite size (~ 120-150 nm) in the synthesized  $\text{MnSi}_{1.73}$  samples can be attributed to their processing employing reactive spark plasma sintering, which is recognized to produce material compounds with low crystallite sizes [162,168]. During SPS, a rapid sintering rate is applied to the powdered green compact under pressure so that the sample spends little time in the low-temperature regime, where non-densifying mechanisms, such as surface diffusion are active.

During SPS, spark plasma generation, and consolidation takes place under the axial force to facilitate the material consumes less time in the low-temperature, where non-densifying mechanisms, such as surface diffusion are active, and proceeds quickly to higher temperatures where densifying mechanisms, such as grain boundary or volume diffusion are dominant.[28]. The quite number of literature on the synthesis of materials using spark plasma reaction sintering wherein low crystallite size ~ 100-200 nm has been obtained [28,162,168].

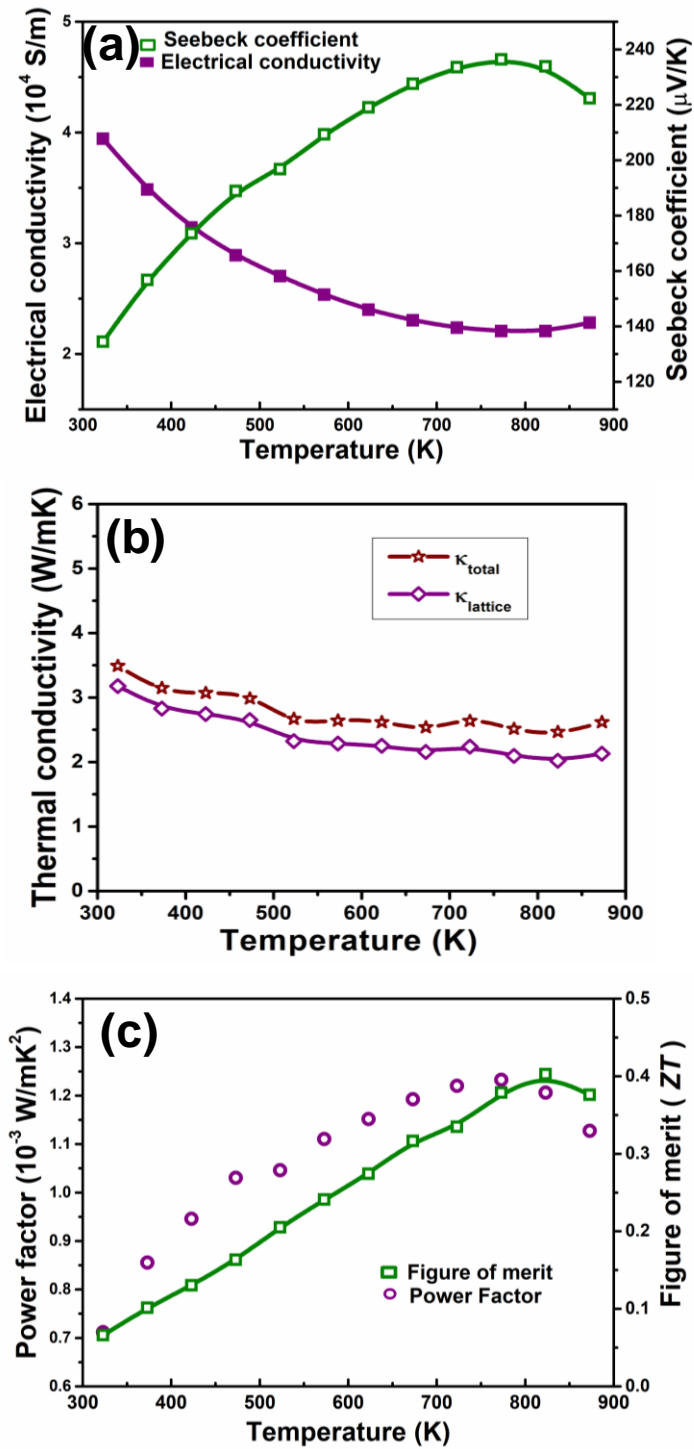


Figure 5.7. Temperature dependence of the thermoelectric properties of the synthesized undoped MnSi<sub>1.73</sub> sample (a) Seebeck coefficient and electrical conductivity, (b) total and lattice thermal conductivity, (c) power factor and thermoelectric figure-of-merit.

### 5.1.5.3. Figure-of-merit

Figure 5.7(c) & 5.8(c) shows the dimensionless figure-of-merit (ZT) for SPS processed undoped, and Al-doped HMS materials. The figure-of-merit of both samples, increase with increasing temperature and high ZT is observed at 873 K. The calculated value of ZT ( $\alpha^2\sigma/\kappa$ ) for the synthesized undoped  $\text{MnSi}_{1.73}$  sample, as shown in Fig 4(c) shows a ZT  $\sim 0.4$  at 873 K. The calculated value of ZT for the SPS sintered Al-doped  $\text{MnSi}_{1.73}$  sample, as shown in Figure 5.8(c) shows a ZT  $\sim 0.65$  at 873 K. The increased value of ZT in HMS was reported in this study, although using a single-step reaction assisted spark plasma sintering process, which consumes a few minutes compared to quite a lot of processing duration required using other material synthesizing processes employed for thermoelectric HMS. The excellent thermoelectric properties in the sintered  $\text{MnAl}_{1.73}$  sample is mainly due to its low thermal conductivity ( $\sim 1.7$  W/mK), which originates from the low crystallite size (120-150 nm) in the  $\text{MnAl}_{1.73}$  sample, synthesized using reactive spark plasma sintering.

### 5.1.6. Conclusions

The undoped and Al-doped  $\text{MnSi}_{1.73}$  were synthesized employing plasma assisted sintering, wherein the in-situ reaction between the Mn and Si powders and their subsequent compaction performed in a single step and a less time consumption as compared to quite long duration hours required for synthesizing the same HMS material using conventional techniques. The phase composition, surface morphology and atomic-scale structure of the HMS ( $\text{MnSi}_{1.73}$ ) was performed using X-ray diffraction, electron microscopy attached to energy dispersive spectroscopy. The increased figure-of-merit (ZT),  $\sim 0.65$  at 873K, was gained in Al-doped  $\text{MnSi}_{1.73}$  employing simple and cost-effective material synthesis method.

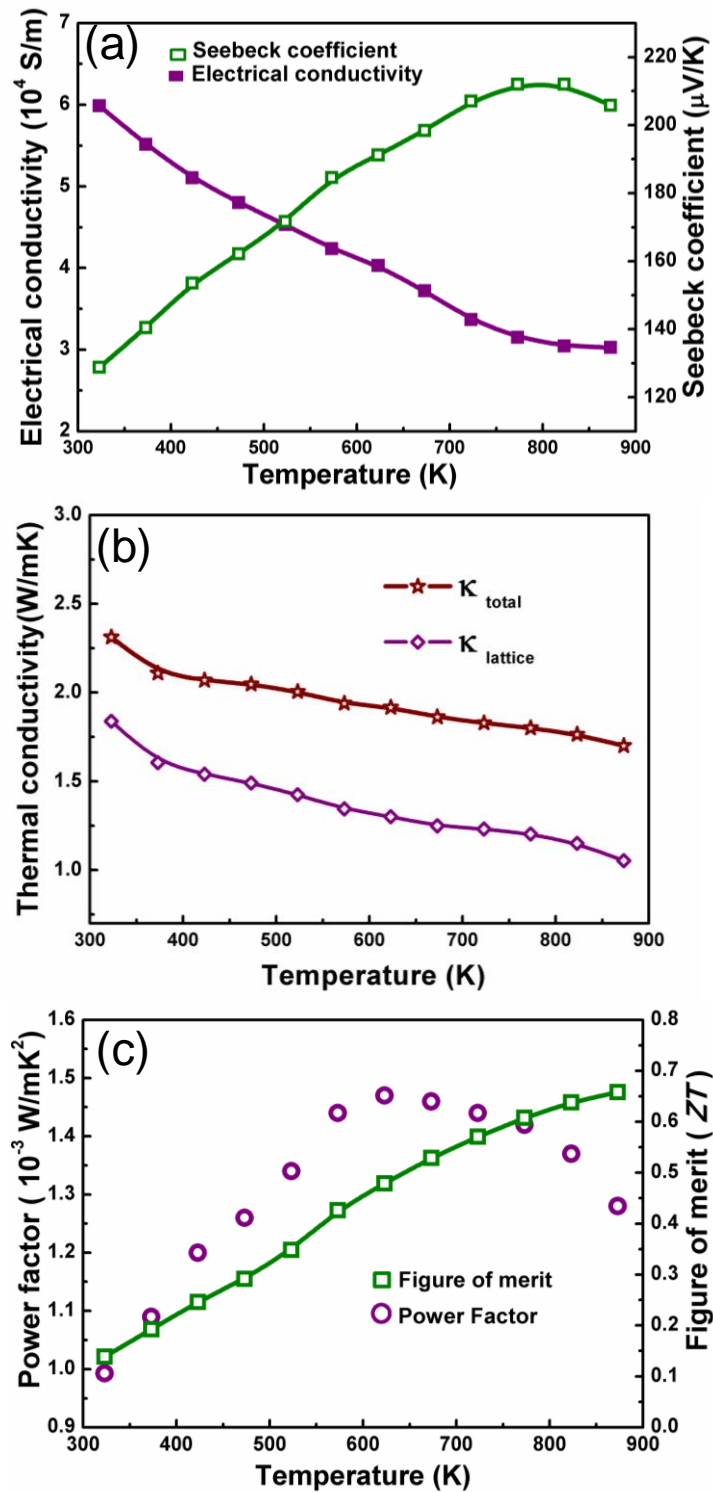


Figure 5.8. Temperature dependence of the thermoelectric properties of synthesized Al-doped MnSi<sub>1.73</sub> sample (a) Seebeck coefficient and electrical conductivity, (b) total and lattice thermal conductivity, (c) power factor and thermoelectric figure-of-merit.

## 5.2. Nanostructured p-type Higher Manganese Silicides

### 5.2.1. Introduction

The low figure-of-merit (ZT) of Higher Manganese Silicides (HMS) is the primary obstacle for realizing a solid n-Mg<sub>2</sub>Si/p-MnSi<sub>1.73</sub> thermoelectric device, which is well-known for harnessing heat energy into electrical energy, owing to its thermal and chemical stability, and crust abundance and eco-friendly nature. Magnesium silicides (n-type) are extensively studied; however, there are only limited numbers of investigations on higher manganese silicides (p-type), due to their complex Nowotny structure and a thin line of composition variation in the Si & Mn binary phase diagram [106]. Various approaches have been attempted to enhance the thermoelectric properties of *p-type* MnSi<sub>1.73</sub>, which include, doping or substitution of elements and the use of different material processing techniques. Despite intense research, the figure-of-merit of *p-type* MnSi<sub>1.73</sub> is still restricted to ~ 0.6. Recently, the microstructural engineering and non-equilibrium synthesis employing novel material processing techniques lead to enhance the material's thermoelectric performance. The studies have shown the introduction of high-density interfaces and grain boundaries employing nano/ultrafine grain structure enhance the phonons scattering significantly. This mechanism offers a reduction in thermal conductivity without disturbing the electrical conductivity, resulting in an improved figure-of-merit [28,169]. Synthesis of nanowires and nanoribbons of higher manganese silicides using chemical vapor deposition (CVD) is reported by Higgins et al. [102]. However, no specific thermoelectric properties study on these synthesized HMS. The lowest thermal conductivity has been observed in nanostructured HMS employing ball milling combined hot press technique by Zamanipour et al.[170] The MnSi<sub>1.73</sub> have been manufactured using mechanical alloying, liquid metallurgy, such as Arc Melting, Vacuum Induction melting based



techniques. However, these processes lead to a stoichiometry difference and the development of undesirable by-product cubic metallic MnSi phase due to extended hours of ball milling.

Melt spinning is a rapid solidification technique, which provides high & rapid cooling to the materials, producing nanoscale features in its microstructures. This method is employed to fabricate the materials that involve very high cooling rates to synthesize, amorphous, nano and ultrafine grain structured materials [30,118,119]. Till date, this technique has been used in a wide range of materials including pure metals, alloys and limited thermoelectric compounds [107,109,159]. It has been observed that combined melt spinning with spark plasma sintering (MS-SPS) of Bi<sub>2</sub>Te<sub>3</sub> produces bulk nanostructure and increases figure of merit about 73% [171]. The figure-of-merit has been observed to increase by almost 50% in MS-SPS of (BiSb)<sub>2</sub>Te<sub>3</sub> nanocomposites [172]. The MS-SPS of Yb<sub>0.2</sub>Co<sub>4</sub>Sb<sub>12+y</sub> material refines the matrix grain size about ~ 150nm and disperses nanoscale second phase [173]. Further, all the reported studies on thermoelectric materials by MS-SPS significantly reduce the thermal conductivity, which attributes to enhance the figure of merit [171–175]. Recently, enhanced power factor has been observed in melt spinning combined solid state reaction of Mg<sub>2</sub>Si<sub>0.3</sub>Sn<sub>0.7</sub> by Zhang et al. [176]. In the present study, higher manganese silicide (Al-doped HMS) was synthesized employing a melt spinning and spark plasma sintering (MS-SPS) by optimizing the cooling rates. This technique outcomes the anticipated compositional control and furthermore present nanostructure crystals in the processed MnSi<sub>1.73</sub> melt-spun ribbons. This approach leads to an increased figure-of-merit  $ZT \sim 0.82$  at 800 K in Al-doped MnSi<sub>1.73</sub>, using the melt-spinning process at a cooling rate  $\sim 2 \times 10^7$  K/s, followed by rapid spark plasma assisted sintering (SPS). This good thermoelectric performance originates from the nanograined structure of higher manganese silicide

phase; obtained using the synthesis of melt spinning combined with rapid spark plasma assisted sintering process. The nanoscale features exhibit a low thermal conductivity value of  $\sim 1.5$  W/mK at 800 K, resulting in an enhanced ZT. The microstructural characteristics of higher manganese silicide at different melt spin wheel speeds have been investigated, based on which the enhancement of thermoelectric performance is discussed.

### **5.2.2. Experimental details**

The arc melted ingots of Al-doped HMS approximately 5 g was taken in the hexagonal Boron Nitride Crucible. The melt-spinning experiment was carried out in Melt Spinner unit (Model: Melt spinner HV, Make: Edmund Buhler) at different surface wheel speeds. The surface speed of the wheel chosen was  $\sim 15$  m/s, 23 m/s, and 30 m/s. Initially, the entire chamber is evacuated with a diffusion pump and purged with argon three to five times. The molten alloy is injected by inert argon gas, through the split type nozzle over the water-cooled copper wheel. The melt was expelled at the pressure of 0.05 MPa through a rectangular slit (0.2 mm x 10 mm) on a rotating water-cooled copper wheel ( $\varnothing 250 \times 60$  mm) keeping a wheel- to-slit distance of 0.4 mm. The metal solidified in the water-cooled copper wheel and thrown out in the form of small strips. The supercooled ribbons/strips were collected from the chamber and pulverized for spark plasma sintering. These powders were subjected to rapid spark plasma sintering at a heating rate of 100 K/min using SPS-725, at 1073 K for 10 min at uni-axial pressure 60 MPa in a die and punch ( $\varnothing 12.7$  mm) keeping vacuum atmosphere. Archimedes principle determined the SPS processed materials' density. The XRD analysis was performed using monochromatic Cu-K $\alpha$  radiation using Rigaku-make XRD (Miniflex-II). Scanning Electron Microscopy showed the microstructure analysis of melt-spun ribbons and sintered HMS sample (Zeiss, Supra V40) attached with

Energy Dispersive Spectroscopy. A detailed microstructural analysis of ribbons/flakes and MS+SPS sintered specimens was carried out employing high-resolution transmission electron microscopy (Tecnai G2F30 STWIN). Rectangular samples of  $\text{MnSi}_{1.73}$  were machined from the center of the synthesized samples for the determination of Seebeck coefficient and electrical conductivity, using Ulvac-ZEM3 apparatus. A  $\varnothing$  12.7mm disc sample was used for laser flash diffusivity measurement employing Thermal constant Analyzer (Make: LINSEIS, Model: LFA 1000). The specific heat ( $C_p$ ) was estimated by Sapphire differential scanning calorimetry method using Netzsch DSC 404 F1. Finally, thermal conductivity ( $\kappa$ ) was determined from the relation, diffusivity ( $\alpha$ )  $\times$  specific heat ( $C_p$ )  $\times$  density ( $\rho$ ). The Hall measurements were carried out by using HEMS system, Nanomagnetics Instruments, with a field strength of  $\pm 1$  T.

The benefits of rapid solidification technique have been used to synthesize the  $\text{MnSi}_{1.73}$  HMS-phase by varying the cooling rates (solidification rate), which has controlled by the surface speed of the water-cooled copper wheel during solidification. Figure 5.9 describes the pictorial representation of process methodology to synthesize the bulk nanostructured Al-doped HMS in the present study.

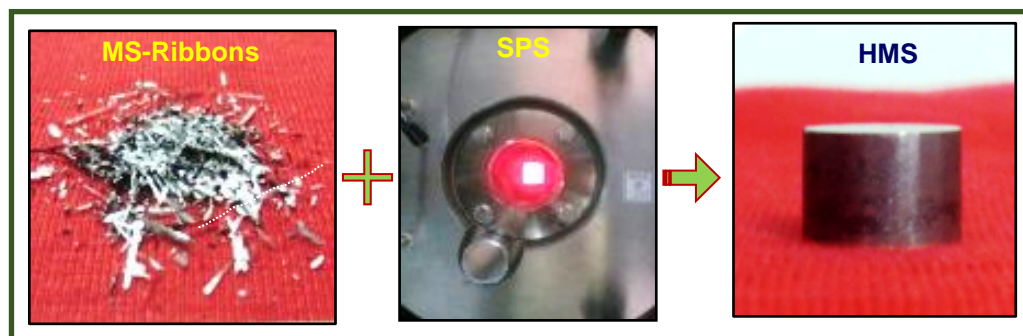


**Figure 5.9.** The photograph showing the process flow of bulk nanostructured Al-doped HMS synthesis, employing Melt spinning (MS) and Spark plasma sintering (SPS)

Figure 5.10 shows the thickness of the melt-spun ribbons ( $s$ ) and cooling rate ( $dT/dt$ ), as a function of the wheel surface speed. Figure 5.11 reveals that the increasing the wheel surface speed from 15 to 30 m/s results the decrease in ribbon thickness from 35 to 10  $\mu\text{m}$ . The power relationship for the present data is found to be  $s \propto V_s^{-1.5}$  and is reasonably good agreement with the reported values of  $s \propto V_s^{-1.3}$  [177] and  $s \propto V_s^{-1.231}$  [178].

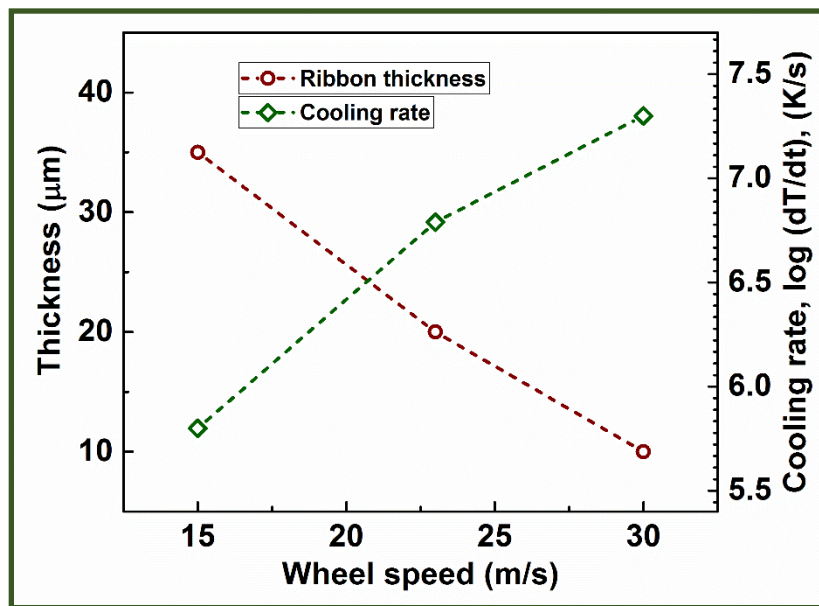


**Figure 5.10. Variations of Ribbon thickness and cooling rate, at different wheel speeds (15,23 & 30 m/s) during Melt spinning process**

The average cooling rate was calculated using the relation  $dT/dt = (h \times \Delta T)/(s \times \rho \times C_p)$ , where ' $h$ ' is coefficient of heat transfer,  $\Delta T$  is the temperature difference between the molten material and wheel, ' $\rho$ ' is the density, ' $C_p$ ' is the specific heat and  $s$  is the thickness of the melt-spun ribbons. The cooling rates are estimated employing the above equation  $\sim 7 \times 10^5$ ,  $5 \times 10^6$  and  $2 \times 10^7$  K/s for wheel speeds 15, 23 and 30 m/s, respectively. The calculated cooling rate as a function of wheel speed is plotted on a logarithmic scale in Figure 5.11. Increasing the wheel speed leads to lower the thickness of melt-spun ribbon and higher the cooling rate extensively. The macroscopic effect of higher cooling rate is discussed microscopically using electron microscope

evidence. Turnbull reported that the growth of large metal crystals into their supercooled melts is very rapid and usually limited only by the solidification rate at which they diffuse from the interface [179]. Evidence of distinct grain structures in both processed materials is due to different solidification rates imparted by the wheel speeds. The rapid heat of solidification from the interface in the material prepared with higher speed (30 m/s) leads to a significant amount of grain/grain boundaries accumulation. Table 5.1 shows the various process parameters employed in the melt spinning process and their corresponding resulted in values of crystallite size.

**Table 5.1. The crystallite sizes and transport parameters of the melt-spun combined spark plasma sintered higher manganese silicides processed at different wheel speeds.**

Wheel speed (m/s)	Thickness of melt-spun ribbons ( $\mu\text{m}$ )	Cooling rate (K/s)	Average crystallite size (nm)		Carrier concentration ( $10^{21} \text{ cm}^{-3}$ )	Mobility ( $\text{cm}^2/\text{VS}$ )	Effective mass
			Melt-spinning	Melt-spinning + spark plasma sintering			
15	35	$7 \times 10^5$	36	40	0.69	3.52	$4.7m_e$
23	20	$5 \times 10^6$	34	38	0.83	3.02	$5.2 m_e$
30	10	$2 \times 10^7$	25	29	1.94	1.53	$9.2 m_e$

The wheel speed greater than 30 m/s led to high rate of cooling but resulted in the undesired amorphous crystal structure in the processed ribbons/flakes. On the other hand, wheel speed lower than 15 m/s leads to a meager rate of cooling of the molten material, which resulted in the formation of cubic metallic MnSi phase and quite larger grain size in the processed materials, which are not suitable for realizing high figure-of-

merit. Therefore, the materials produced by using wheel speeds in the range of 15-30 m/s employing melt spinning technique.

### 5.2.3. X-ray diffraction analysis

The X-ray diffraction pattern of the MS-SPS processed HMS sample at cooling rates (Figure 5.11(a)), suggest that for all cooling rates, the HMS as the primary phase with the existence of trace amount of silicon phase. However, XRD pattern notably confirms that is devoid of the metallic MnSi phase(cubic), which is an unavoidable by-product of the sintering of HMS and is identified to degrade its thermoelectric properties [112–114]. XRD analysis provides the crystallite sizes of as-melt spun HMS employing Williamson-Hall method, found to be ~ 36, 34, 25 nm corresponding to the cooling rates of  $7 \times 10^5$ ,  $5 \times 10^6$  and  $2 \times 10^7$ , respectively (Table 5.1). The average crystallite sizes of MS-SPS material were determined to be ~ 40, 38, 29 nm corresponding to the cooling rates of  $7 \times 10^5$ ,  $5 \times 10^6$  and  $2 \times 10^7$ , respectively. (Table 5.1). Figure 5.11(b), which shows the XRD of MS-SPSed HMS(MnSi<sub>1.73</sub>) material, confirms that the phases of MnSi<sub>1.73</sub> and primary silicon and the nanoscale features, introduced during melt-spinning at all wheel speeds (cooling rates), are retained post-SPS leading to a negligible grain growth during sintering. Figure 5.11(c), exhibits a significant broadening of the main major peak of HMS phase at different wheel speeds. This peak broadening is attributed to the more number of crystallites formation with nanocrystallite boundaries in the synthesized material. The XRD pattern of the MS-SPS processed HMS suggests the formations of MnSi<sub>1.73</sub> are almost similar to the JCPDS 00-020-0724. The XRD analysis confirms the existence of an additional primary silicon phase. It was noted from the XRD analysis that the nanoscale microstructure resulting from high cooling rates aids in controlling the phase of HMS, but also suppresses the formation of MnSi-phase identified as unfavorable for its thermoelectric properties.

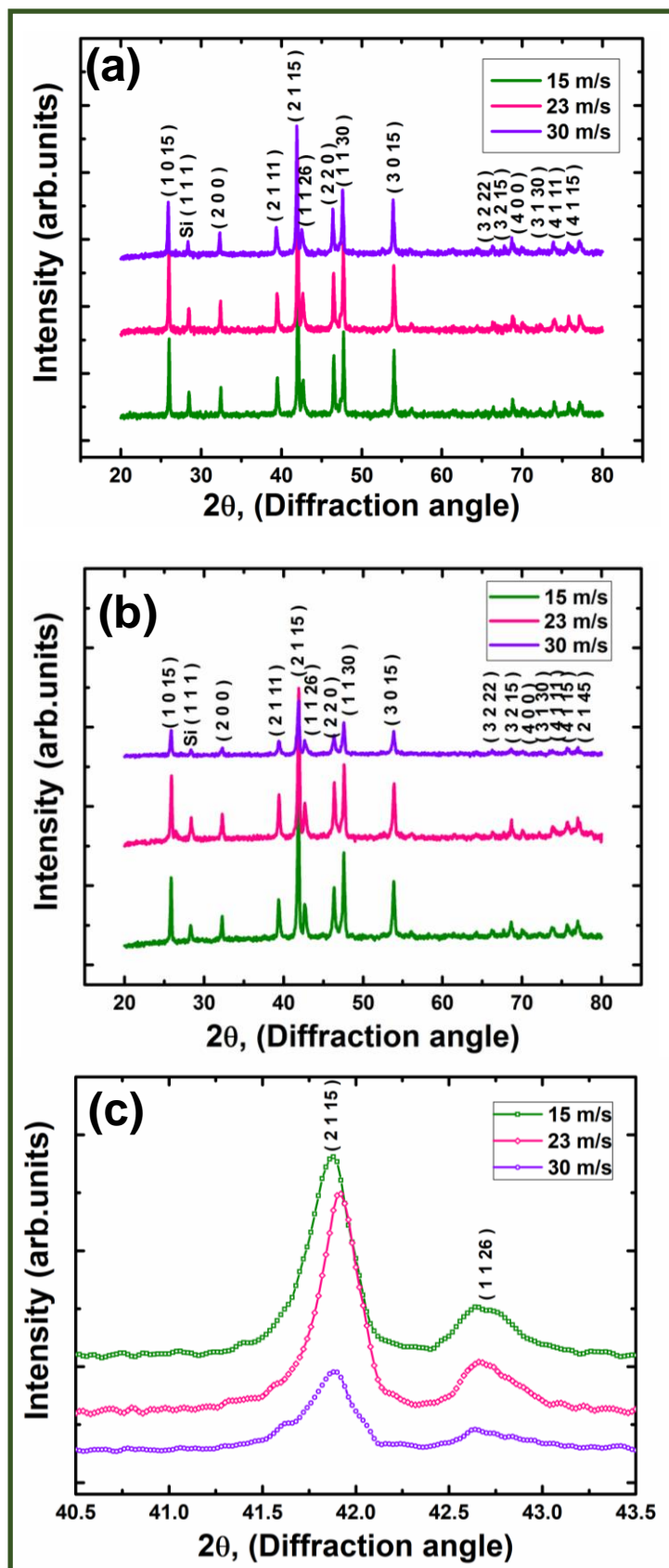


Figure 5.11. X-ray diffraction pattern of processed HMS samples (a) melt-spun flakes/ribbons (b) melt-spinning combined spark plasma sintered HMS and (c) peak broadening, at a different wheel speeds

#### 5.2.4. Microstructural analysis

Figure 5.12 shows the melt spun processed higher manganese silicide microstructures corresponding to 15, 23 and 30 m/s wheel speeds. Initially, the material (Figure 5.12(a)) composed of large grains with an average size of  $\sim 3\mu\text{m}$ . Figure 5.12(A) exhibits the distribution of the HMS grains at a surface wheel speed of 15 m/s. The aspect ratio of the grains is very high, and the grain sizes are falling between 400 nm and 20  $\mu\text{m}$ . The surface wheel speed at 23 m/s, equiaxed grains are generated by increased levels of cooling rate concerning wheel speed. The material (Figure 5.12(b)) composed of equiaxed grains with a grain size of  $\sim 2.5\mu\text{m}$ . Figure 5.12(B) exhibits the grain distribution of HMS at a surface wheel speed of 23 m/s, spreads from minimum 600 nm to maximum 7  $\mu\text{m}$  grain size. Figure 4c shows the microstructure of the melt spun HMS at a surface wheel speed  $\sim 30$  m/s, revealing extremely fine and fully equiaxed grains. From the microstructure (Figure 5.12(c)) and grain distribution curve (Figure 5.12(C)), the average size was observed to be  $\sim 500$  nm and the grain sizes falling between 130 nm to 2  $\mu\text{m}$ . Figure 5.13 shows the scanning electron microstructures and corresponding elemental mappings of melt-spun ribbons processed at 30 m/s. The existence of Al in the sample is confirmed by Electron Dispersive Spectroscopy (EDS) analysis, which is not revealed by XRD analysis. The individual elemental mapping shows the uniform distribution of Mn & Si in melt spinning processed ribbons. Findings from our energy dispersive spectroscopy (EDS) measurement suggest that there is no difference in the stoichiometry of melt spun processed higher manganese silicide ribbons (Inset (Figure 5.13)). Turnbull reported that the growth of large metal crystals into their supercooled melts is very rapid and usually limited only by the solidification rate at which they diffuse from the interface



[179]. Evidence of distinct grain structures in the melt spun HMS material are due to different solidification rates imparted by the wheel speeds.

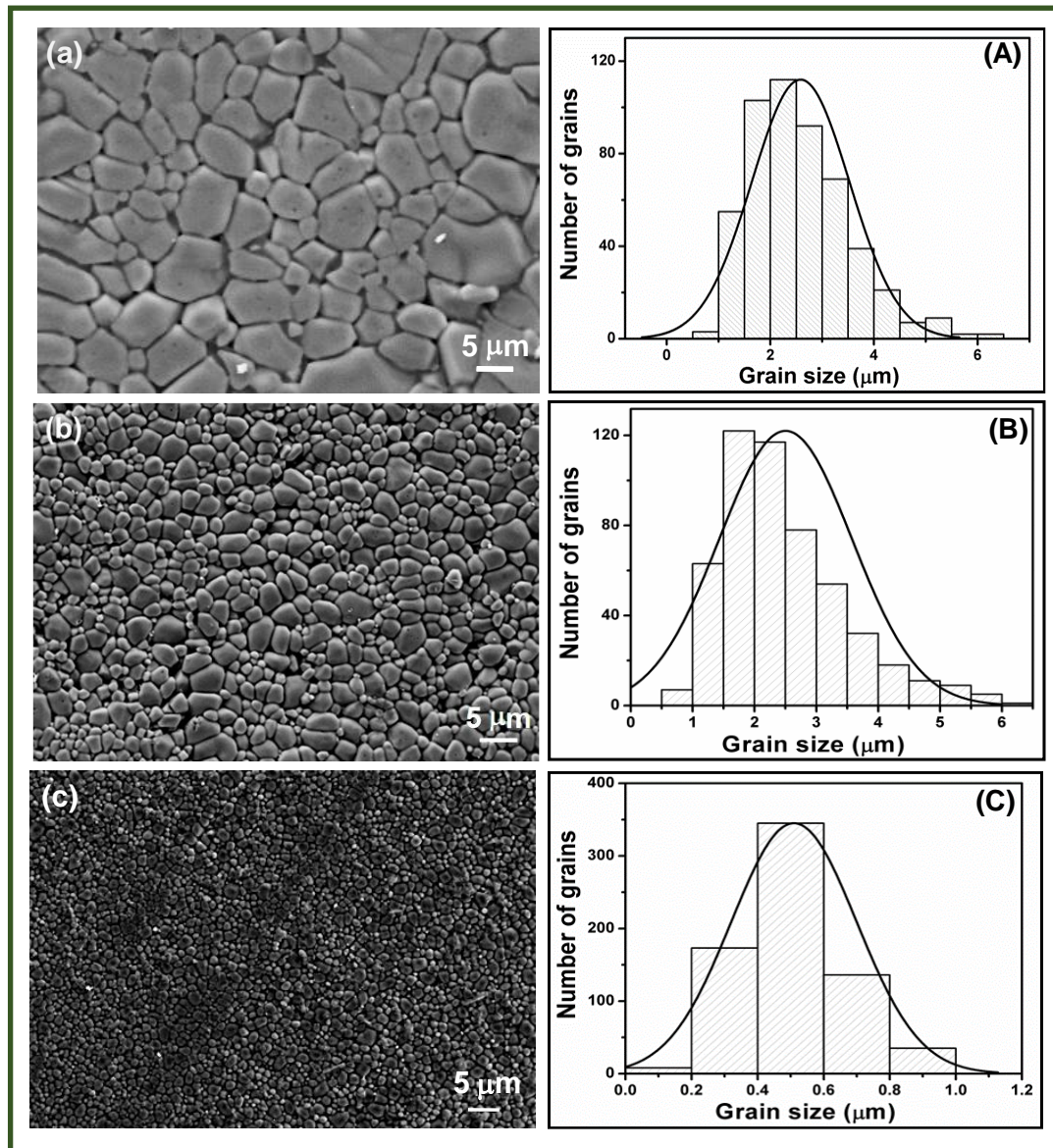


**Figure 5.12. SEM micrographs of the melt-spun processed HMS ribbons/flakes and corresponding grain distributions, at different wheel speeds (a) 15 m/s, (b) 23 m/s and (c) 30 m/s**

Figure 5.13 shows the surface morphology (Figure 5.13(a)), EDS (inset) and the individual element maps (Figure 5.13(b-d)) of the melt-spun HMS ribbons, processed at a surface wheel speed of  $\sim 30$  m/s. The EDS results confirm an even distribution of the Mn, Si, and Al in the spark plasma sintered HMS sample.

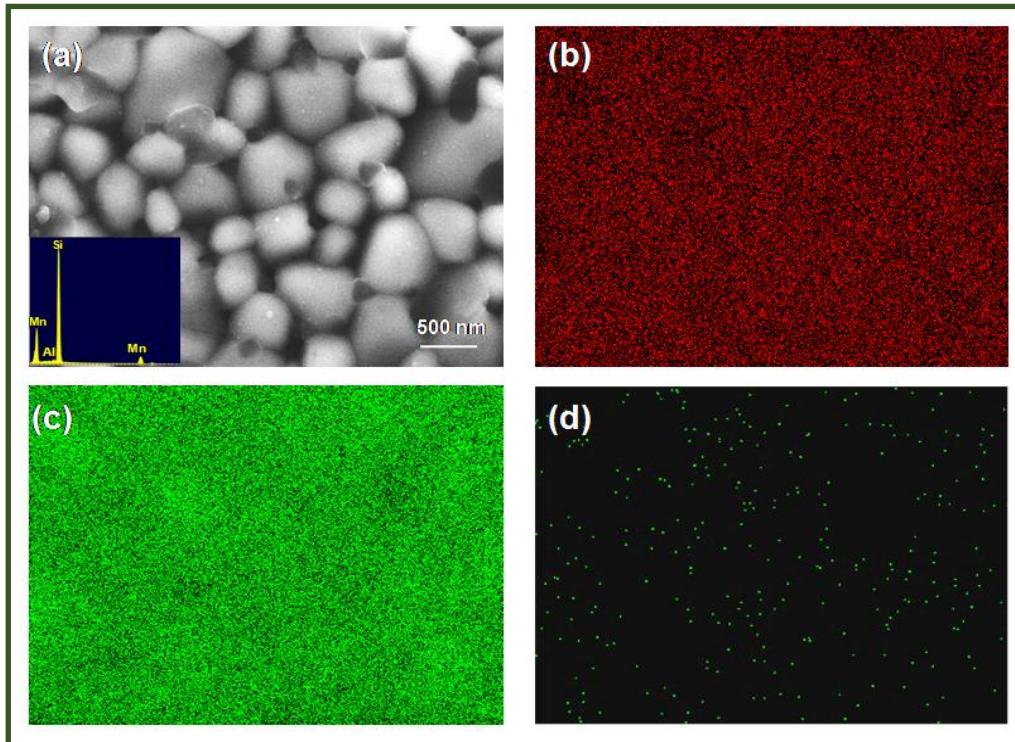


**Figure 5.13.** (a) SEM micrographs of Melt-spun ribbons and its EDS spectrum (inset); (b), (c) and (d) individual elemental maps of melt-spun HMS

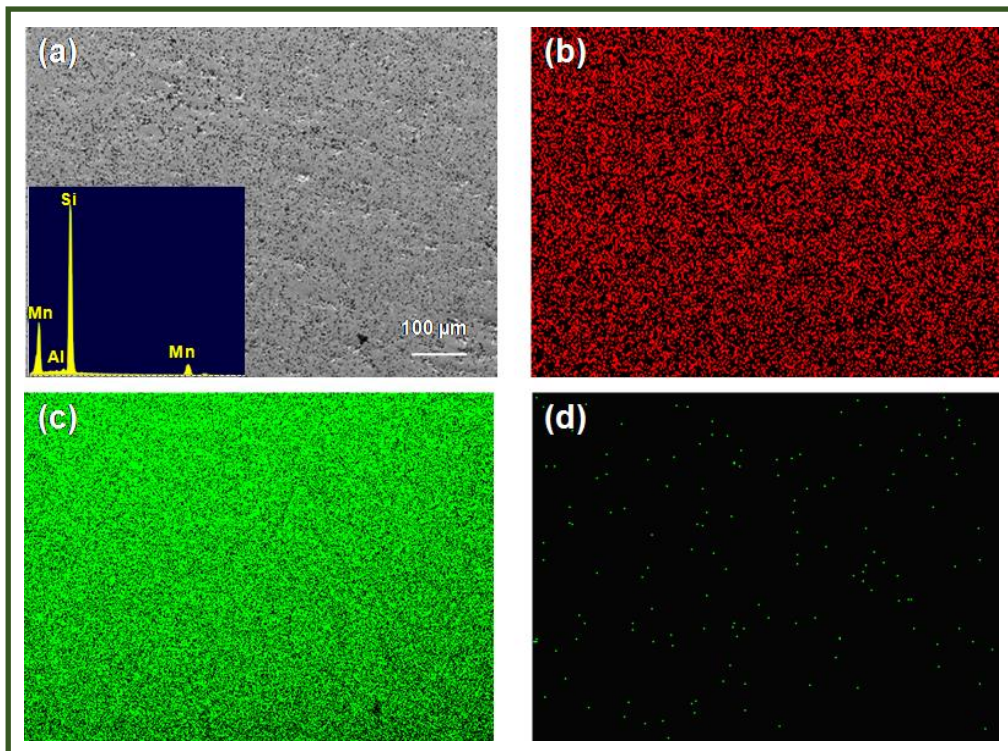


**Figure 5.14.** (a) SEM micrographs of spark plasma sintered HMS and its EDS spectrum (inset); (b), (c) and (d) individual elemental maps of the SPS processed HMS

Figure 5.14 shows the surface morphology (Figure 5.14(a)), EDS (inset) and the individual element maps (Figure 5.14(b-d)) of the MS-SPSed HMS material, processed at a surface wheel speed of  $\sim 30$  m/s. The EDS results confirm an even distribution of the Mn, Si, and Al in the spark plasma sintered HMS sample.

HRTEM was performed to explain the nanoscale features in melt-spun, and MS-SPS processed HMS material both in real and reciprocal space (Figure 5.15). A nano-grained microstructure of melt-spinning processed HMS ribbons was observed throughout the material (Figure 5.15(a)) with the grains sizes of  $\sim 20$  to  $50$  nm. A selected area electron diffraction pattern (SAEDP) showed numerous Debye rings in reciprocal space (inset A in Figure 5.15(a)), which correlated with the HMS-phase ( $\text{Mn}_{15}\text{Si}_{26}$ , tetragonal crystal structure, space group:  $I\bar{4}2d$ , lattice constants:  $a = 0.55$ ,  $c = 6.56$  nm, JCPDS file no.: 00-020-0724). The planes in the SAEDP indicated as 1, 2 and 3, correspond to hkl:  $2\ 1\ 15$ ,  $1\ 1\ 30$ ,  $3\ 0\ 15$  with the spacings of  $0.22$ ,  $0.19$ ,  $0.17$  nm, respectively. Figure 5.15(b) delineates a magnified view encompassing few grains and Moiré patterns evolved during rapid solidification during material synthesis. A line contrast encircled by a white dotted line in grain (Figure 5.15(b)) at high magnification reveals the existence of grain boundary with  $\sim 0.22$  nm inter-atomic separation (inset B in Figure 5.15(b)). However, the rest of the grain with an arrow shows clear atomic-scale image constituted of inter-atomic planes spacing of  $0.22$  nm (inset C in Figure 5.15(b)). Figure 5.15(c&d), delineates the microstructural features of MS-SPSed HMS material. In general, a compound microstructure throughout in the specimen has been observed at the nanoscale (Figure 5.15(c)). A magnified view of region G in Figure 5.15(c) shows a small length of a grain boundary with a semi-coherent appearance and with a thickness of about  $1$  nm. Further, both sides of the boundary (inset D in Figure 5.15(c)) show the presence of two sets with  $0.22$  and  $0.19$  nm inter-atomic spacings.

Moreover, quite a lot of tiny crystals overlap observed in the microstructure (region G in Figure 5.15(c)), and a large moiré patterns networking has been generated, and  $\sim 0.17$  nm atomic planes also are noticed underneath the moiré patterns (inset E of Figure 5.15(c)). A marked circle region labeled as H in Figure 5.15(c), resolved at an atomic scale, confirms that the region (Figure 5.15(d)) is constituted of atomic planes, hkl: 2 1 15 and 3 0 15 with the spacings of 0.22 and 0.17 nm. Further, at high magnifications, the existence of excess primary silicon in the microstructure with a size  $\sim 3 - 6$  nm. The ultrafine scaled primary silicon inclusion of size about 5 nm in the matrix of HMS (as indicated in Figure 5.15(e) has been displayed in Figure 5.15(f). The atomic planes stacked along Si (hkl:111) with a  $\sim 0.32$  nm inter-planar spacing are indicated in Figure 5.15(f).

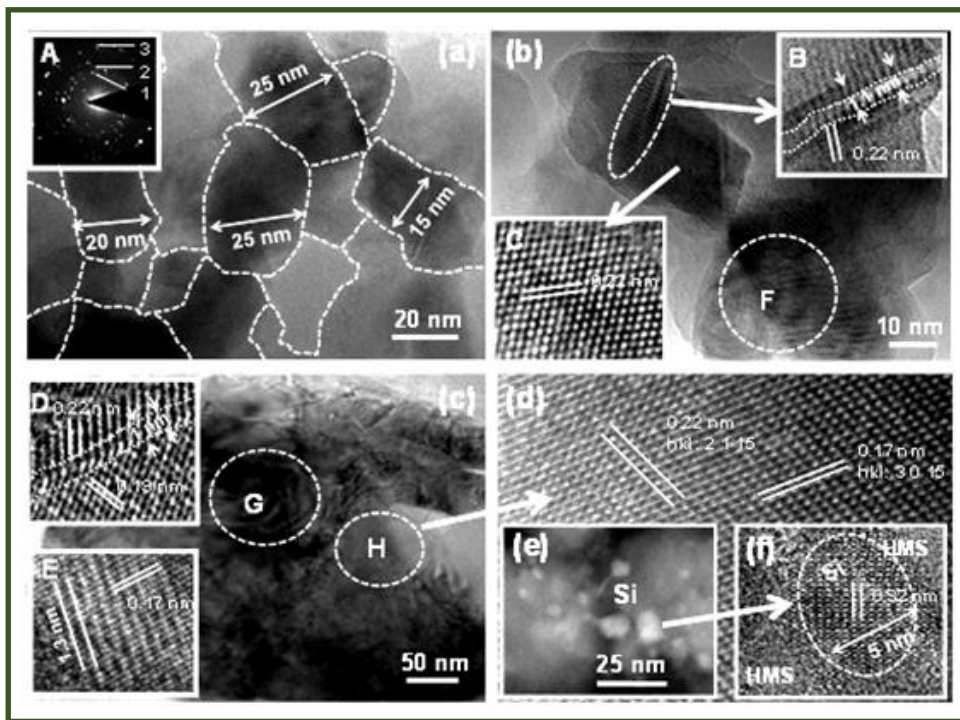


**Figure 5.15.** HR-TEM microstructures of MS-SPS HMS (a) grains distribution of melt-spun ribbons, (b) magnified view of the grains, (c) a complex microstructure of melt-spin & spark plasma sintered sample, and (d) atomic scale image of (c) showing the planes, (e) Silicon nanoparticles and (f) atomic scale image of a nano-sized Si. Insets: (A) electron diffraction pattern of HMS grains, (B) grain boundaries, and (C) atomic scale image, (D) atomic scale image of a grain boundary, and (E) Moire fringes and a set of atomic planes

## 5.2.5. Thermoelectric properties

### 5.2.5.1. Electronic transport properties

Figure 5.16(a–c), which exhibits the thermoelectric transport properties of the melt spinning combined with spark plasma sintered HMS, confirms that the behavior of electrical conductivity, Seebeck coefficient, and thermal conductivity is comparable to the studies reported by others, although with different values. Figure 5.16(a) shows that the electrical conductivity exhibits an anticipated reduction and lastly a minor increase at higher temperatures, which could be linked to the bipolar conduction. This graph also confirms that electrical conductivity increases with increasing the cooling rate via surface wheel speed, which showed an inverse dependence of electrical conductivity on the grain size (Table 5.1 and Figure 5.11). This electrical conductivity increase with the decrease in grain size could be credited to the improvement of the carrier concentration. It is been described that nano-sized particles with electrical conductivity larger than the matrix could lead to overall increase in electrical conductivity via enhancement of carrier concentration, subjecting to the size and spacing of the nanoparticles in the semiconductor matrix [180,181]. In the current situation, the occurrence of silicon nano-sized particles in the  $\text{MnSi}_{1.73}$  matrix (Fig. 2 and 3) in the same way could origins to local compositional fluctuations and lattice-size variation in the microstructure consequently rearranging the Fermi level and concentration of the carriers. Figure 5.16(b) shows that the temperature dependence of Seebeck coefficient for the melt spinning combined spark plasma sintered  $\text{MnSi}_{1.73}$ , which confirms that Seebeck coefficient values primarily increases with increasing temperature and after attaining the highest value it lastly exhibits a declining trend above 800 K, which could be linked to the thermal excitation of the carriers. The highest value of Seebeck coefficient ( $\alpha \sim 250 \mu\text{V/K}$ ) is observed for the synthesized

HMS sample at a cooling rate of  $2 \times 10^7$  K/s employing the wheel speed of 30 m/s. The positive Seebeck coefficient values over the full experimented temperature range, reveals the p-type conduction in the melt-spinning followed by spark plasma sintered HMS samples.

#### **5.2.5.2. Thermal transport properties**

Figure 5.16 (b), which shows the temperature dependence of thermal conductivity in melt-spinning combined spark plasma sintered  $\text{MnSi}_{1.73}$  samples, exhibits a reduction with increasing temperature trailed by a minor increase at the temperatures above 800 K at all cooling rates via surface wheel speeds and is this behaviour is comparable to that described previous reports in  $\text{MnSi}_{1.73}$ . The thermal conductivity exhibits a strong inverse dependence on the wheel speed and a very low value of thermal conductivity value  $\sim 1.5$  W/mK was observed at the highest surface wheel speed of 30 m/s, which is the low thermal conductivity value of reported thus far for HMS. This lowest value of thermal conductivity originates from the nanoscale features resulting via high cooling rate during melt-spinning. The high surface wheel speed imparts the higher cooling rate of the molten material (Table 5.1) leading to a substantial amount of undercooling of the molten HMS material, which offers a significant refinement of the grains. The microstructure of the melt-spinning combined with spark plasma sintered HMS material composes of nano-scale crystallite (20-40 nm) with excess silicon (3-9 nm), which imparts high-density grain boundaries in a widespread nano-scale range, leading to huge nano-scale grain boundaries contributing the scattering of phonons. It is well known that heat-carrying phonons in thermoelectric semiconductors lie in a wide band of wavelengths, however, in HMS it has recently been reported that most of the heat is conducted by low-wavelength phonons [40,182]. In the present context, the nanocrystallite boundaries in the synthesized  $\text{MnSi}_{1.73}$  material cover a widespread

dimensional range which scatters low-to-mid wavelength phonons resulting in a very low thermal conductivity value. The lattice thermal conductivity ( $\kappa_L$ ) (estimated by subtracting the electrons contribution ( $\kappa_e$ ), determined from electrical conductivity using the Wiedmann–Franz relation, from the thermal conductivity), shown in Figure 5.16(d) evidently confirms that the total thermal conductivity has a substantial contribution from its lattice thermal conductivity part. Therefore, the decrease in thermal conductivity in the synthesized HMS samples could largely be attributed to large scattering of phonons by the  $\text{MnSi}_{1.73}$  matrix (20-40 nm) and Silicon (3-9 nm) nano-sized crystallites, which impart high-density grain boundaries in the widespread low-to-mid nano-scale dimensions.

### **5.2.5.3. Figure-of-merit**

Figure 5.16(c) exhibits the temperature dependence of the power factor ( $\alpha^2\sigma$ ) for melt-spinning combined with spark plasma sintered  $\text{MnSi}_{1.73}$  materials at different cooling rates via surface wheel speeds, which confirms that the maximum power factor is observed in samples at the cooling rate  $2 \times 10^7$  K/s employing highest surface wheel speed of 30m/s. The  $ZT$  versus temperature shown in figure 5.16(c), shows that a highest  $ZT \sim 0.82$  at 800 K was observed in  $\text{MnSi}_{1.73}$  rapid plasma assisted sintered material, melt-spinning processed at a high cooling rate via surface wheel speed 30 m/s, which is  $\sim 26\%$  higher value than the reported value so far in  $\text{MnSi}_{1.73}$ . A high  $ZT$  results from the improved power factor and a significantly reduced thermal conductivity originating from a nanograined microstructure, composing of the  $\text{MnSi}_{1.73}$  phase (20-30 nm) with homogeneously distributed Silicon (3-9 nm) nano-sized particles, due to fast cooling rate solidification using melt-spun at enhanced high surface wheel speed. The nano features in SPSed  $\text{MnSi}_{1.73}$  materials, which are preserved post sintering, impart a high density of nano-scale boundaries at different dimensional scales.

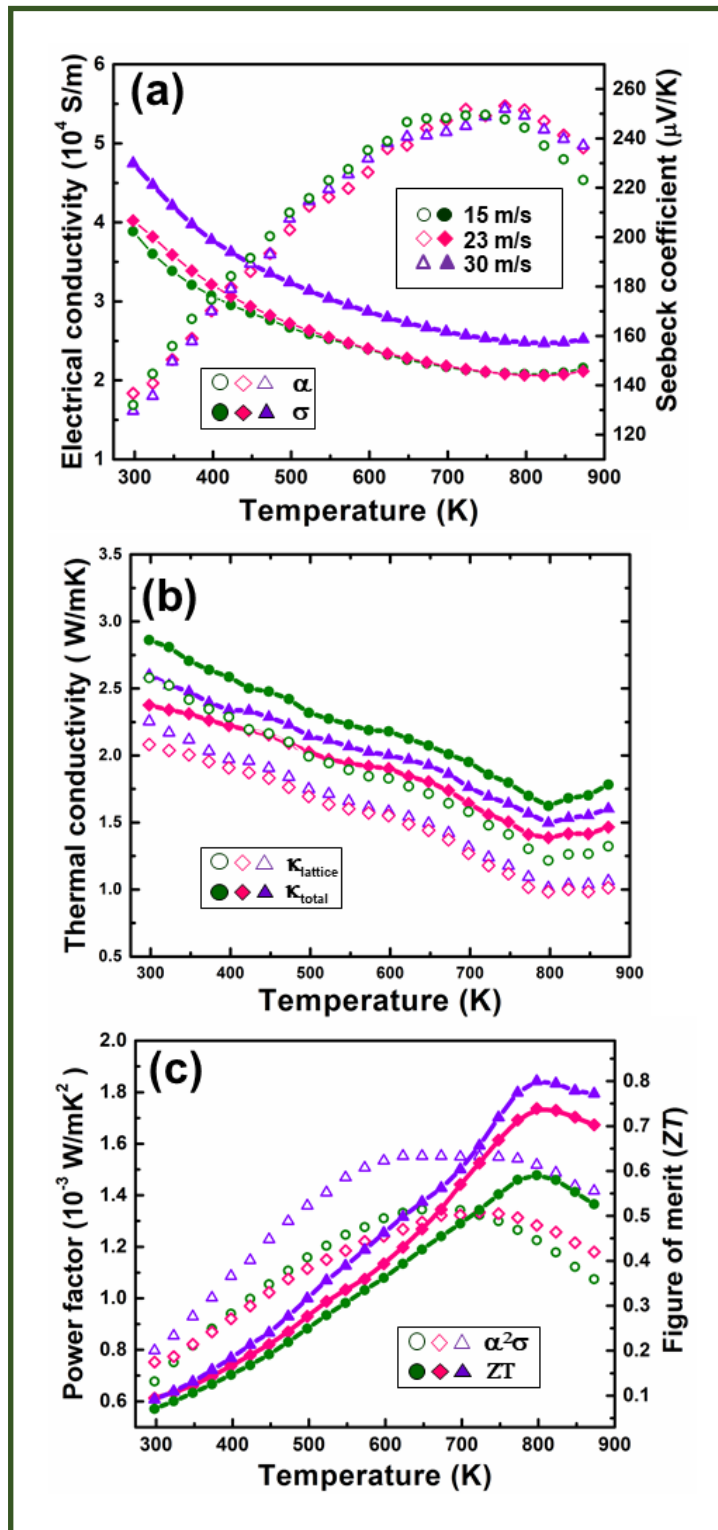


Figure 5.16. Thermoelectric properties of melt-spinning combined with spark plasma sintered HMS (a) Seebeck coefficient and electrical conductivity, (b) total and lattice thermal conductivity, (c) power factor and figure-of-merit.



They scatter the phonons in a widespread spectrum low-mid wavelengths resulting a low value of thermal conductivity  $\sim 1.5$  W/mK, which mainly contributes to the improvement of figure-of-merit. The high cooling rate results in the nanoscale microstructure in the  $\text{MnSi}_{1.73}$  and also offers the favorable compositional control, both of which are desirable for enhancing the thermoelectric performance.

### **5.2.6. Conclusions**

The benefits of rapid solidification technique using melt-spinning have been exploited to significantly improve the thermoelectric properties of *p-type* Aluminium doped  $\text{MnSi}_{1.73}$ , which significantly improves the microstructure and aids an improved control on the phase composition of  $\text{MnSi}_{1.73}$ , which are identified to enhance its thermoelectric properties. The highest ZT  $\sim 0.82$  at 800 K was obtained in melt-spinning combined with spark plasma sintered  $\text{MnSi}_{1.73}$ , melt-spun at a high cooling rate of  $\sim 2 \times 10^7$  K/s. This extraordinary thermoelectric property in the processed  $\text{MnSi}_{1.73}$  resulting from an ultrafine-grained microstructure due to high cooling rates of solidification, which composing of  $\text{MnSi}_{1.73}$  matrix (20-30 nm) with additional Silicon nanoparticles (3-9 nm) homogeneously distributed in the matrix. The  $\text{MnSi}_{1.73}$  matrix and Silicon with nanocrystallite boundaries, at different dimensional scales, scatter the wide-ranging spectrum of low and medium scale wavelength phonons and therefore exhibiting in a low-value thermal conductivity, which mainly contributes to the improvement of ZT. Therefore, the nanostructured features of HMS as a result of the high cooling rate of solidification, the control of phase composition and devoid of the metallic cubic-Mn-Si phase offers a significant improvement in thermoelectric properties in the melt-spinning combined with spark plasma sintered HMS.

# CHAPTER 6

Chapter 6 describes the mechanical properties of the plasma-assisted reactive sintered *n-type* Mg<sub>2</sub>Si and *p-type* MnSi<sub>1.73</sub>. The mechanical properties are similarly important along with their thermoelectric performance, to circumvent the sudden mechanical failure of their devices during actual operational conditions. The mechanical properties of the synthesized Mg<sub>2</sub>Si result a substantially improved hardness value of  $\sim 5.4 \pm 0.2$  GPa and an elastic modulus  $\sim 142.5 \pm 6$  GPa with a fracture toughness of  $\sim 1.71 \pm 0.1$  MPa $\sqrt{\text{m}}$ . The mechanical properties of the synthesized MnSi<sub>1.73</sub> result a highly enhanced value of hardness  $\sim 16 \pm 1$  GPa and an elastic modulus  $\sim 367 \pm 8$  GPa with a fracture toughness of  $\sim 3 \pm 0.1$  MPa $\sqrt{\text{m}}$ . The friction and wear characteristics of Mg<sub>2</sub>Si have been reported for the first time, to understand the durability of their thermoelectric devices under actual hostile environments. Despite employing a cost-effective material processing technique, superior mechanical properties were achieved in silicide-based thermoelectric materials.

## 6.1. Introduction

Thermoelectric devices convert heat energy into electrical energy using solid state materials without any moving parts. Thermoelectric devices have drawn considerable attention in energy harvesting applications due to its simple, stable and robustness. However, thermoelectric device fabrication involves many complications such as *p* & *n-type* compatibility, ohmic contacts of thermoelectric legs, economical synthesis, etc. In addition to the thermoelectric properties of materials, the mechanical performance evaluation is the primary criteria for achieving final device applications. The thermoelectric device operates typically in a profoundly hostile environment like gas & nuclear power plants, industrial furnaces and deserts. The service durability and

reliability are the primary concern in thermoelectric materials/devices development. There are extensive studies available on the thermoelectric properties; however, limited literature is available for mechanical properties evaluation [97–101]. Several design factors are to be addressed regarding the thermoelectric device. However, the strength, hardness and elastic modulus provide one way of opening the door for device development.

Technological compatibility is a significant concern in developing thermoelectric generators/segmented generators. The inherent nature of material synthesis process has its limitations to keep the constituent elements for device fabrication. Hence, the standard system of tensile, compressive test measurements may not be possible for evaluating the mechanical strength of such type of materials/devices. But the demand arises to characterize the mechanical properties measurement, so the micro & nanoscale testing equipment evolves to solve the problem of developing thermoelectric devices. Recently, the mechanical properties evaluation of thermoelectric material was carried out by Vickers microhardness and indentation fracture toughness by measuring the radial crack length [99]. The brittle materials may follow the crack length mechanism whereas ductile materials will not support the radial crack, will lead to wrong interpretation. The grain boundary inclusions and second phase precipitates will impede the growth of crack propagation, especially silicide-based/doped thermoelectric materials [100]. The leg material should withstand various kind of thermal and mechanical stresses under real working conditions, to warrant the structural integrity of silicides thermoelectric modules. The mechanical properties of the material are significantly essential to circumvent the structural failure of their thermoelectric devices during real operational conditions. The mechanical properties such as elastic modulus, hardness, fracture toughness and thermal shock resistance, are

to be examined, before their operational deployment. Although there are reports of the mechanical behavior of thermoelectric materials in the literature, a detailed study of optimization of processing parameters and establish process-structure-properties correlations was lacking. The mechanical properties correlation with microstructures imparts prime importance, to evaluate thermoelectric material for device applications. In the present chapter, the mechanical properties of the synthesized thermoelectric n-Mg<sub>2</sub>Si & p-MnSi<sub>1.73</sub> materials have been studied, wherein Mg<sub>2</sub>Si doped with Bi and Sb, and MnSi<sub>1.73</sub> doped with Al. The mechanical properties, such as elastic modulus, hardness, fracture toughness and thermal shock resistance were studied and correlated with the microstructure of the synthesized material, to understand the failure mechanisms. The improved mechanical performance of synthesized materials was correlated with microstructural features and process parameters optimization. The tribological properties, such as wear and friction were reported, to examine the materials under actual hostile environment. The unique spectrum of mechanical properties investigations on Mg<sub>2</sub>Si & MnSi<sub>1.73</sub> materials were studied for its reliability.

## **6.2. Experimental Details**

The specimens were sized from the synthesized Mg<sub>2</sub>Si & MnSi<sub>1.73</sub> materials with a dimension of  $\varnothing 12.7 \times 2$  mm for hardness and fracture toughness measurements. The microhardness and indentation fracture toughness were performed using a Vickers diamond pyramidal indenter (136°) attached with a microhardness tester (Model: FM-e7, Make: Future Tech, Japan), on polished disc-shaped samples. An electron microscope was employed to measure the imprinted crack parameters an improved accuracy. The nanoindentation test was performed using Berkovich diamond indenter attached with nanoindenter. The cone pyramidal diamond indenter having nominal edge faces 65.3° from the vertical axis, used for the experimentation. The applied loads of 10,

20, 30 and 40 mN with ten iterations for each load variation were chosen. A steady and constant loading & unloading speed has been maintained throughout the experiment. Wear and friction experiments were performed using a pin-on-disc Ducom-TR20LE wear machine. Friction and wear tests were performed for synthesized samples against a SiC paper (600 mesh) pasted firmly to metal disc keeping a sliding speed of ~1, 4 and 7 m/s. The variable sliding speeds were chosen by wind speed simulation in desert conditions [120], where the thermoelectric device is being operated. The wear and friction experiments were performed at applied loads of 10, 30 and 50 N keeping a constant sliding distance of 500 m. The coefficient of friction ( $\mu$ ) of the pin-disc pair was recorded using a frictional force transducer coupled to an equipment. Analysis of the worn surfaces of pin and disc were performed by scanning electron microscope (Zeiss, SUPRA V40, Germany) with an attached Energy Dispersive Spectroscopy (EDS) system.

### **6.3. Microhardness analysis**

Hardness is the resistance of the materials against plastic deformation and perhaps a direct evaluation of the strength of the material. Hardness is the measure of mechanical strength of common engineering materials. Hardness can be interpreted material resistance against plastic deformation, wear & tear and fracture, which depends upon the application of the materials. The atomic-level mechanism associated with a hardness of the material and hardness relationship with microstructure is highly complex. Thus, the systematic mechanical characteristics evaluation of thermoelectric n-Mg<sub>2</sub>Si & p-MnSi<sub>1.73</sub> materials was carried out from micro-level hardness measurements by using diamond square pyramid indenter at different load levels.

The microhardness of the synthesized thermoelectric n-Mg<sub>2</sub>Si & p-MnSi<sub>1.73</sub> materials was performed using Vickers square-based diamond pyramid indenter with angle 136°.

The indentations were made on the polished surface of the specimen by applying loads of ~ 1,3,5 N for 10 seconds. After removing the load, the diagonal of the indentations was measured using an optical microscope. The Vickers hardness (HV) of the material is calculated by using the formula:

$$H_v = \frac{2F \sin \frac{136^\circ}{2}}{d^2} \text{----- (6.1)}$$

where F is the applied load in Kg and d is the diagonal length of the indentation in mm. The hardness values of the sintered materials were plotted in Figure 6.1 with error bars. Figure 6.1(a) shows the Vickers microhardness values of spark plasma sintered Mg<sub>2</sub>Si with three different applied loads (1, 3 & 5 N). The material exhibits the microhardness values of 469±16, 451±10 and 446±5 Hv with load levels of 1, 3 and 5 N, respectively. In Vickers microhardness test, mean diagonal of the indentation is calculated from the surface imprint after the diamond pyramidal indenter loading is removed. The Vickers hardness is obtained by calculating the ratio of applied load to the square mm area of indentation. Figure 6.1(b) shows the Vickers microhardness values of spark plasma sintered MnSi<sub>1.73</sub> with three different applied loads (1, 3 & 5 N). The material exhibits the microhardness values of 1138±62, 1090±32 and 1021±16 Hv with load levels of 1, 3 and 5 N, respectively. No significant variation was found in the resulted microhardness values with load changes, however two-fold increased hardness is observed in *p-type* MnSi<sub>1.73</sub> compared to *n-type* Mg<sub>2</sub>Si. Grain boundary engineering is a strengthening mechanism of materials by decreasing their average grain or crystallite size proposed by Hall-Petch relationship [183]. The relation between hardness and grain size is described mathematically using Hall-Petch equation,

$$H = H_0 + \frac{k_H}{\sqrt{d}} \text{----- (6.2)}$$

where 'H' is hardness, 'H<sub>0</sub>' & 'K<sub>H</sub>' are materials constant

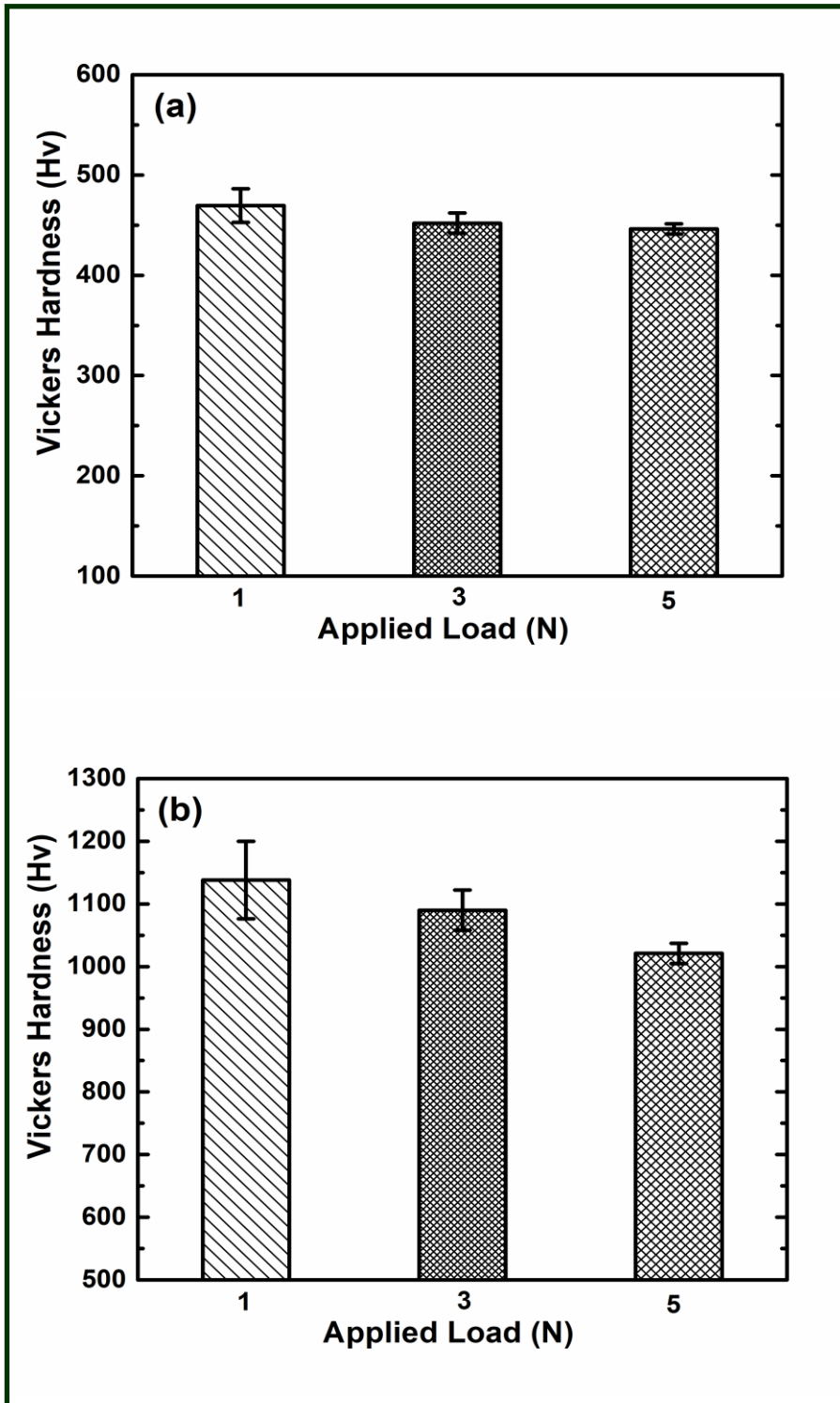


Figure 6.1. Microhardness values of synthesized (a) n-type Mg<sub>2</sub>Si, (b) p-type MnSi<sub>1.73</sub>, at different applied load conditions.

The grain size of the material is controlled by various processing techniques, such as rapid sintering, controlling of the rate of solidification, and severe plastic deformation. In the present study, the SPS process resulted in substantial increase in hardness of n-Mg<sub>2</sub>Si & p-MnSi<sub>1.73</sub>, is due to the grain size refinement. The calculated average crystallite size, by Williamson–Hall method, was ~55 nm in the synthesized *n-type* Mg<sub>2</sub>Si and ~ 200 nm in *p-type* MnSi<sub>1.73</sub> samples. The low crystallite size imposes the more stress to deform the material (or movement of dislocations). It was confirmed that the high hardness values of the spark plasma sintered n-Mg<sub>2</sub>Si & p-MnSi<sub>1.73</sub> materials arising from the grain and grain boundary strengthening mechanism.

#### **6.4. Nanoindentation analysis**

The nanoindentation technique implies applied a load in millinewtons and a depth of penetration in nanometers. Nanoindentation technique is a depth indentation technique, and it is useful to evaluate the mechanical properties of the material at nano/micro-scale level. A milli to micro newton load is applied by a sharp diamond cone indenter to flat polished material specimen. The depth of penetration in the range of nanometers with respect to the applied load is measured. The load-displacement curve (P-H curve) is the general interest from the nanoindentation test and differs from one material to another material [184]. The P-H curve reflects the mechanical properties associated with underlying physical phenomena of the material. The hardness of the material is estimated by using the ratio of the applied load and the contact area at the peak loading. The unloading curve gives a value of elastic modulus using the estimation of the slope. Figure 6.2 shows the load and displacement plot of the synthesized *n-type* Mg<sub>2</sub>Si and *p-type* MnSi<sub>1.73</sub> sample, with applied load range 10- 40 mN. It can be observed that the penetration depth increases with applied loads conditions. The peak value ~ 600 nm at 40 mN for *n-type* Mg<sub>2</sub>Si and for *p-type* MnSi<sub>1.73</sub> ~ 350 nm at 40 mN,



which exhibits the hardness value of Mg<sub>2</sub>Si is lower than that counterpart MnSi<sub>1.73</sub>. The curves exhibit elastic-plastic nature of synthesized silicide materials. No deviations and discontinuities were observed from the P-H curve of synthesized n-type Mg<sub>2</sub>Si and p-type MnSi<sub>1.73</sub>, at the measured load levels (10-40 mN). It can be inferred from the nanoindentation test, the material yield within the elastic-plastic limit at the nanoscale level.

The nanoscale hardness and elastic modulus were determined by using Oliver and Pharr method [185] using the equation 2 & 3,

$$H = \frac{P}{24.5h_p^2} \text{-----} (6.3)$$

$$E = \frac{dP}{dh} \frac{1}{2h_p} \frac{1}{\beta} \sqrt{\frac{\pi}{24.5}} \text{-----} (6.4)$$

where 'P' is applied load, 'h' is displacement of the indenter and 'β' =1.034 for Berkovich indenter.

The calculated hardness values are shown in Figure 6.3(a). The computed hardness value of ~ 5.4 ± 0.2 GPa is comparable to those reported earlier for Mg<sub>2</sub>Si [97,99,100] but inferior to those reported by Wang et al. [98]. The slight variations in the hardness values could attribute to the lower crystallite size (~33 nm) of their Mg<sub>2</sub>Si samples. The elastic modulus of synthesized samples was evaluated from unloading portion of P-H curves (Figure 6.2(a)), according to the procedure described [185][186]. The calculated elastic modulus values are shown in Figure 6.3(b). The computed elastic modulus value of Mg<sub>2</sub>Si (~142.5 ± 6 GPa) is comparatively higher than reported value [100] and similar to those reported by Ishikawa et al. [187].

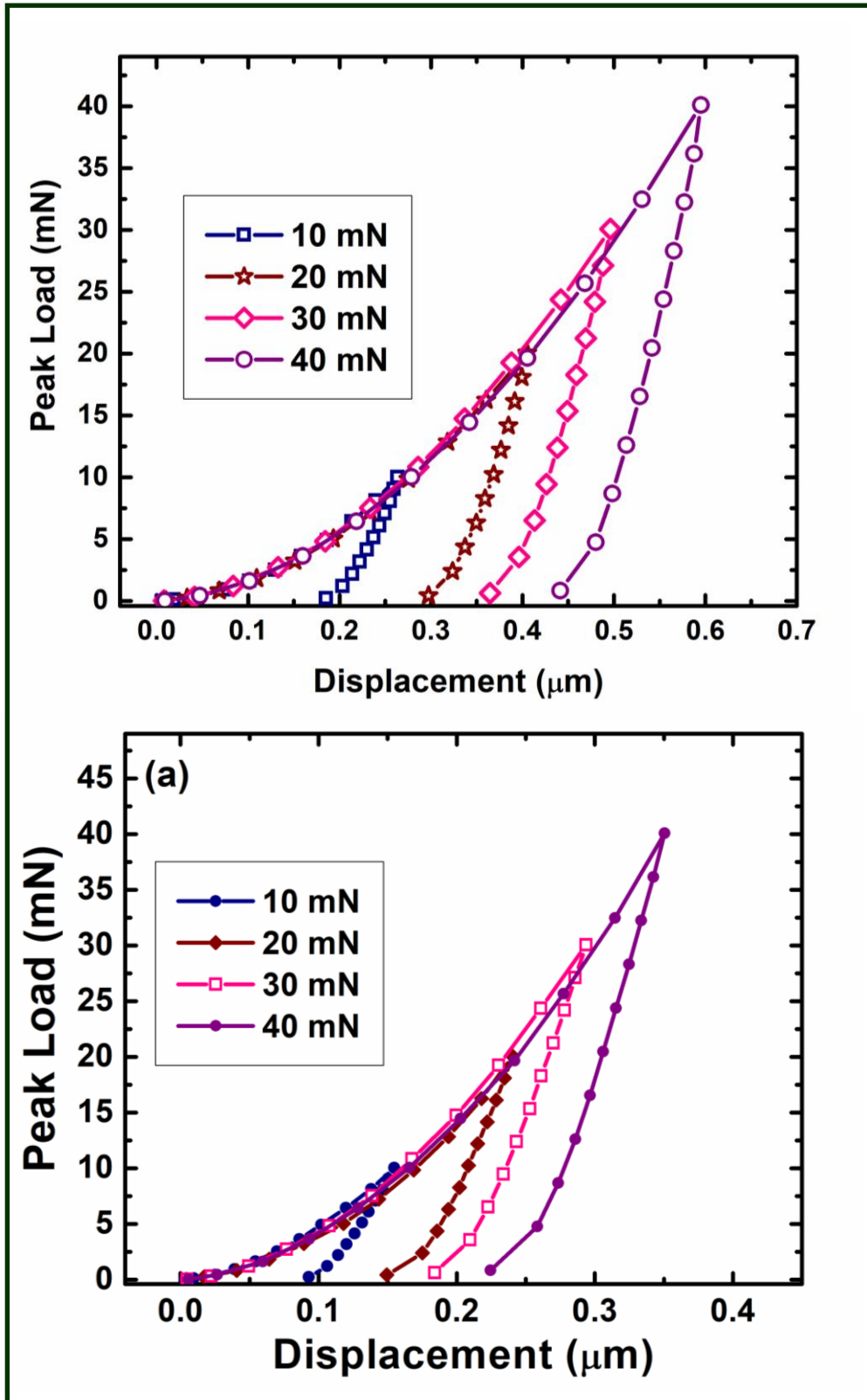


Figure 6.2. A load-displacement (P-H) curves of synthesized (a) n-type  $\text{Mg}_2\text{Si}$ , (b) p-type  $\text{MnSi}_{1.73}$ , at different applied load conditions.

The calculated value of hardness of p-type  $\text{MnSi}_{1.73} \sim 16 \pm 1$  GPa is much higher than n-type  $\text{Mg}_2\text{Si}$ , which can be possibly attributed to the chemical composition and crystal structure and orientation. The average elastic modulus value  $\sim 367 \pm 8$  GPa was calculated from the unloading portion of  $P-H$  curves (Figure 6.2(b)). The nanoindentation technique determined the hardness and elastic modulus of the *p-type*  $\text{MnSi}_{1.73}$  sample, and also it shows the superior mechanical properties to the counterpart material n-type  $\text{Mg}_2\text{Si}$ . Further, the hardness values of the synthesized *n-type*  $\text{Mg}_2\text{Si}$  and *p-type*  $\text{MnSi}_{1.73}$  values are much higher compared with other available thermoelectric materials such as  $\text{Bi}_2\text{Te}_3$  [188], LAST [189],  $\text{PbTe}$  [190] and  $\text{Cu}_2\text{Se}$  [191]. The enhanced mechanical properties in the synthesized  $\text{Mg}_2\text{Si}$  sample mainly arises due to the nano-scale crystallites and distinct grain boundaries, which are introduced by a reactive spark plasma sintering process.

### **6.5. Fracture toughness analysis**

Fracture toughness ( $K_{IC}$ ) or critical stress intensity of the materials expressed by Griffith criterion, relates the mechanical strength, the presence of internal crack/defect. Several techniques available for determining the fracture toughness and its preference depends upon the functional requirement. Indentation fracture technique draws more attention for assessing the toughness measurements of thermoelectric materials, due to its easiness, small specimen size, and less time consumption. Indentation technique is beneficial in evaluating the mechanical properties where the high-end notch specimen preparation is difficult. However, the highly ductile, large grain and single crystal materials are not suitable for evaluation of indentation fracture toughness. An accurate measurement of hardness, elastic modulus and crack length in the material are the essential requirement. The small error in those measurements leads to a wrong interpretation of fracture toughness values.

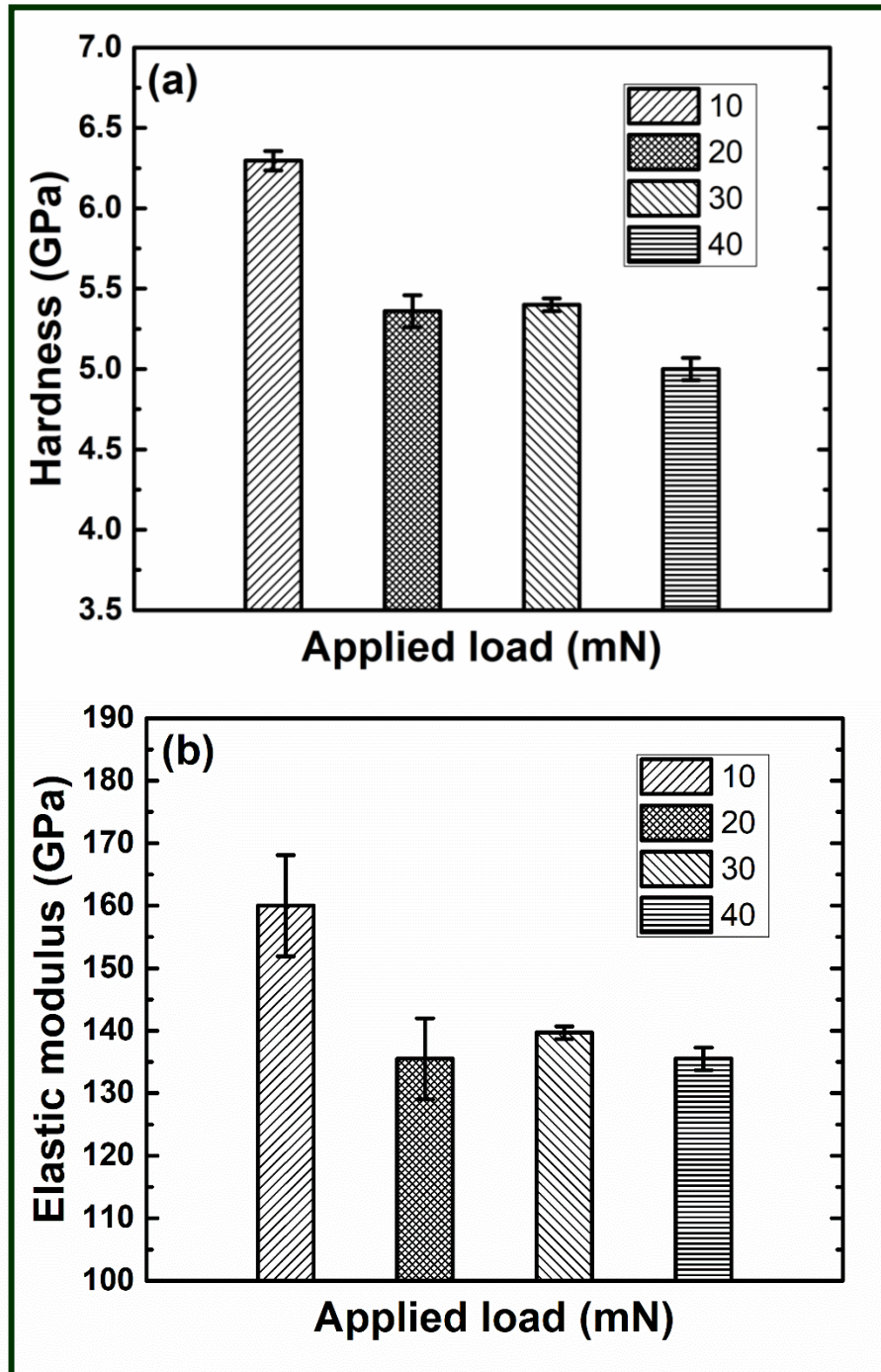


Figure 6.3. Load dependence nanoindentation results SPS synthesized n-type  $Mg_2Si$ : (a) Hardness (GPa) and, (b) Elastic modulus (GPa)

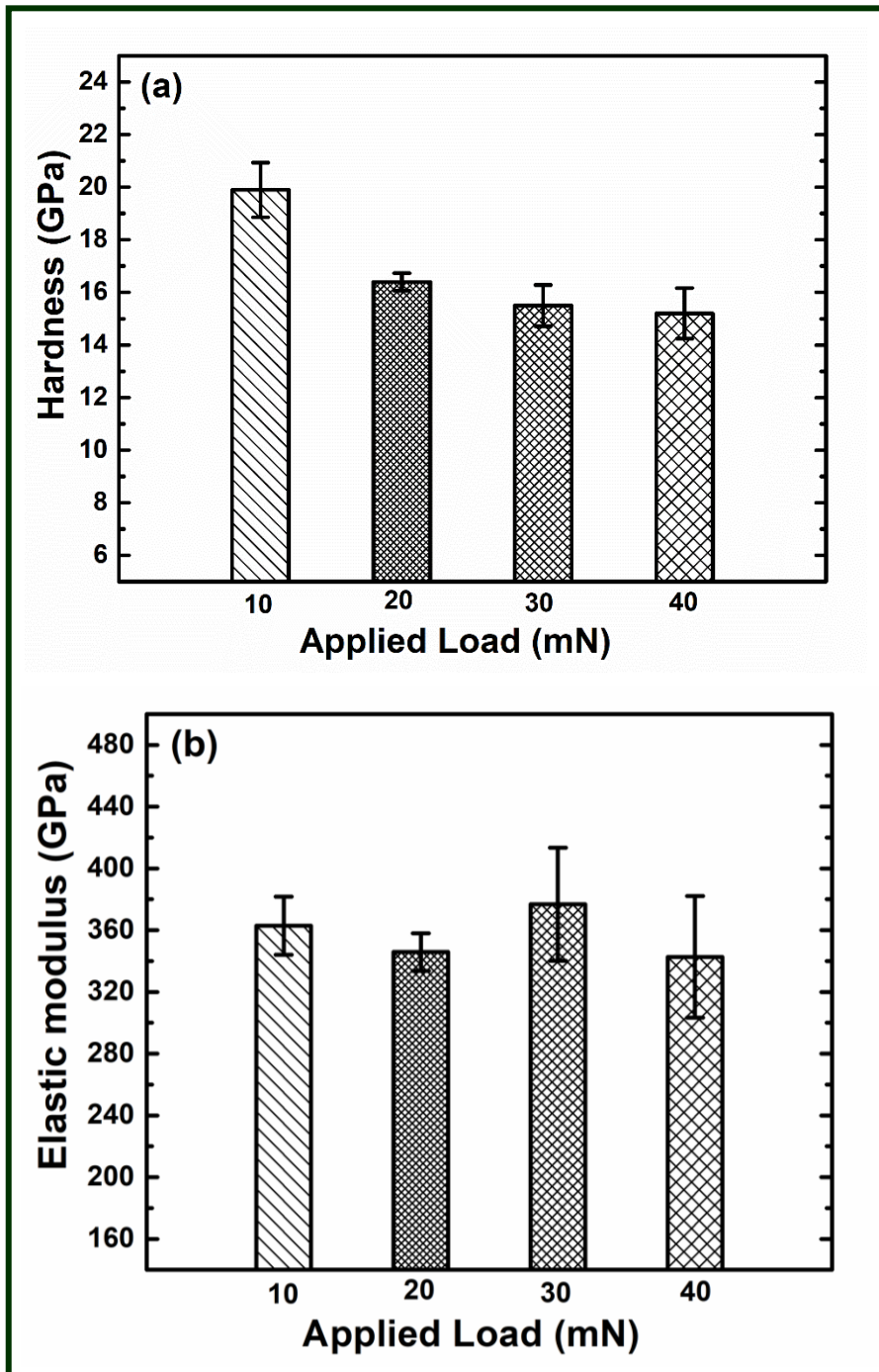


Figure 6.4. Load dependence nanoindentation results SPS synthesized p-type  $\text{MnSi}_{1.73}$ : (a) Hardness (GPa) and, (b) Elastic modulus (GPa)

In the present analysis, fracture toughness was calculated by indentation fracture technique proposed by Niihara et al. [192,193] This method is reported by quite a few researchers recently, for a range of thermoelectric materials. The fracture toughness ( $K_{IC}$ ), is determined by using Vickers indentation crack technique from the equation (2),

$$K_{IC} = 0.0089 \times \left(\frac{E}{H}\right)^{\frac{2}{5}} \times \frac{P}{a l^{1/2}}; \quad 0.25 \leq l/a \leq 2.5 \quad \text{----- (6.5)}$$

where ‘ $P$ ’ is the applied load, ‘ $l$ ’ is the length of the crack, ‘ $a$ ’ is the half-diagonal length of Vickers indentation, ‘ $E$ ’ is the elastic modulus, and ‘ $H$ ’ is hardness value.

The polished samples of n-Mg<sub>2</sub>Si & p-MnSi<sub>1.73</sub> materials were characterized by using a square pyramidal diamond indenter, an applied load of 19.6 N keeping dwell time of 20 seconds. After removal of the load, the produced crack parameters ‘ $a$ ’ & ‘ $l$ ’ were determined using a high-resolution electron microscope for accurate measurement, which is shown in Figure 6.5. For Mg<sub>2</sub>Si, the parameters ‘ $a$ ’ & ‘ $l$ ’ are measured in the range  $4.45\text{-}4.59 \times 10^{-5}$  and  $7\text{-}9.17 \times 10^{-5}$  m, respectively. Based on  $l/a$  ratio proposed by Niihara et al., the fracture toughness value of synthesized n-Mg<sub>2</sub>Si was calculated by using the equation (2). The evaluated indentation fracture toughness value of  $1.71 \pm 0.1$  MPa m<sup>1/2</sup> is higher than that of reported values in Mg<sub>2</sub>Si. Milekhine et al. have reported the fracture toughness values of 0.81–0.97 MPa√m for Mg<sub>2</sub>Si [97], at the same time Ishikawa et al. reported the value of 1.2–1.6 MPa√m [187]. By the addition of SiC nanoparticles, the value of fracture toughness was found to be ~ 1.3 MPa√m by Schmidt et al. [100]. Among them, Wang et al. have reported the maximum value of fracture toughness ~1.67 MPa√m in nanocrystalline Mg<sub>2</sub>Si [98]. The indentation fracture technique is used to evaluate fracture toughness for all reported studies in Mg<sub>2</sub>Si are almost similar. However, the processing route and procedure is different from the one used in the present study.

For  $\text{MnSi}_{1.73}$ , the parameters ' $a$ ' & ' $l$ ' are measured in the range  $1.4\text{-}1.45 \times 10^{-5}$  and  $1.4\text{-}2.5 \times 10^{-5}$  m, respectively. Based on  $l/a$  ratio proposed by Niihara et al., the fracture toughness value of synthesized *p-type*  $\text{MnSi}_{1.73}$  was found to be  $\sim 3 \pm 0.1 \text{ MPa}\sqrt{\text{m}}$ . The calculated fracture toughness value of *p-type*  $\text{MnSi}_{1.73} \sim 3 \pm 0.1 \text{ MPa}\sqrt{\text{m}}$  is 1.8 times higher than that of counterpart n-type  $\text{Mg}_2\text{Si}$ .

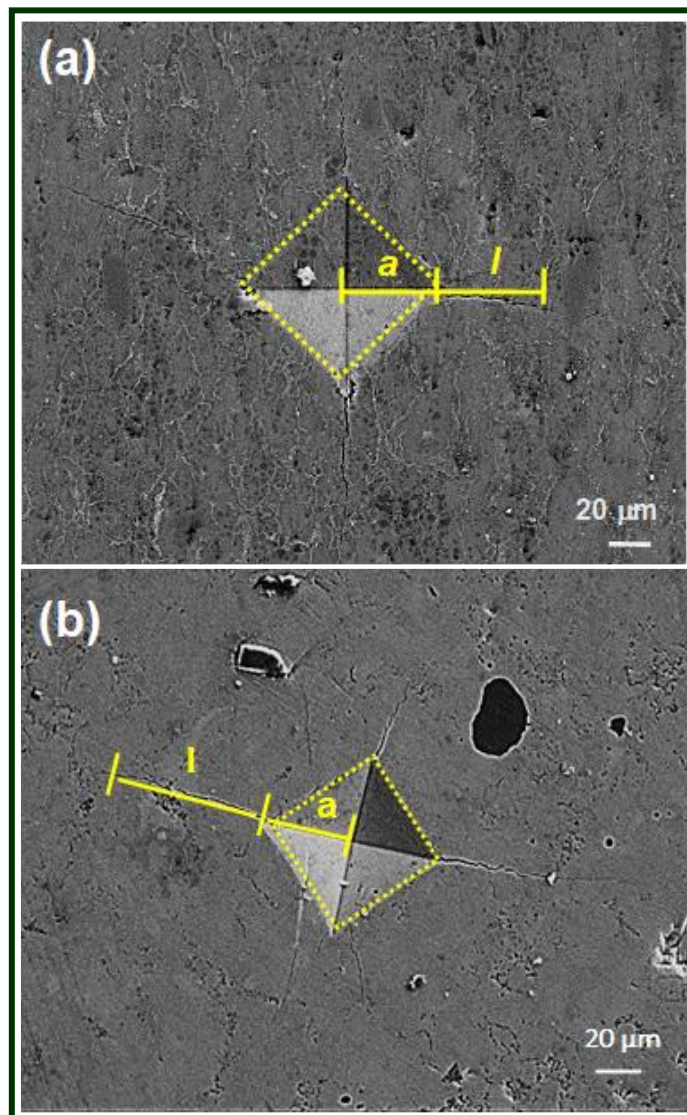


**Figure 6.5.** Electron microscope images of indentation cracks of (a) n-type  $\text{Mg}_2\text{Si}$  and, (b) p-type  $\text{MnSi}_{1.73}$

The high elastic modulus value of MnSi<sub>1.73</sub> enhances the fracture toughness, compared to Mg<sub>2</sub>Si. Further, the fracture toughness values of the synthesized n-type Mg<sub>2</sub>Si and p-type MnSi values are higher compared with other available thermoelectric materials like Bi<sub>2</sub>Te<sub>3</sub> [188], LAST [189], PbTe [190], Cu<sub>2</sub>Se [191]. The application of rapid sintering rate by SPS can significantly impede the grain growth while simultaneously enhancing the sintered density of the product. The SPS processed materials evidence fine grains and sub-grains with grain boundaries of different doping elements. It is inferred that the ultrafine and subgrain/crystallites can impede the crack tip efficiently than coarse grain structure [194,195]. In the present study, the ultrafine grain structure mechanism introduced by SPS process impedes the crack propagation, which results in the enhancement in fracture toughness of the material.

#### 6.6. Thermal shock resistance studies

The thermal shock resistance is considered as vital parameters for designing the thermoelectric modules based on silicide-based materials, as it is equally imparted to mechanical and thermal shocks during the real operational conditions [196,197]. The thermal shock resistance values for *n-type* Mg<sub>2</sub>Si & *p-type* MnSi<sub>1.73</sub> materials are calculated using the equation [196]

$$R_T = \frac{\sigma (1-\nu)\kappa}{\alpha E} \quad \text{----- (6.6)}$$

where ' $R_T$ ' is thermal shock resistance, ' $\sigma$ ' is the fracture strength, ' $\nu$ ' is the Poisson's ratio, ' $\kappa$ ' is the thermal conductivity, ' $\alpha$ ' is the thermal expansion coefficient and ' $E$ ' is the elastic modulus. The thermal shock resistance of *n-type* Mg<sub>2</sub>Si was calculated using the calculated values of  $\sigma$ ,  $E$ ,  $\kappa$  from the experiment and  $\nu$  [99],  $\alpha$  [198] values were taken from the literature. The calculated thermal shock resistance value of *n-type* Mg<sub>2</sub>Si was ~ 300 W/m, which is the highest value reported from Mg<sub>2</sub>Si material and higher



than those reported for other available thermoelectric materials for medium temperature applications [198]. The thermal shock resistance of *p-type* MnSi<sub>1.73</sub> was calculated using the experimentally obtained values of  $\sigma$ ,  $E$ ,  $\kappa$  and  $\nu$ ,  $\alpha$  [187] values were taken from the literature. The calculated value of *p-type* MnSi<sub>1.73</sub> was  $\sim 200$  W/m, which is an inferior to that of the *n-type* Mg<sub>2</sub>Si counterpart.

### 6.7. Friction and wear studies

Friction and wear tests were performed using sintered Mg<sub>2</sub>Si as a pin material, slides against SiC particles embedded disc under a different load (10, 30, 50 N) and variable sliding speed (1, 4 and 7 m/s) conditions. The variable sliding speeds were chosen by wind speed simulation in desert conditions [199], where the thermoelectric device is being operated. The total sliding distance of 500 meters in each experiment was achieved with varying time. The tests were repeated three times, and weight loss of a pin was measured using a weighing balance with an accuracy of 0.0001g.

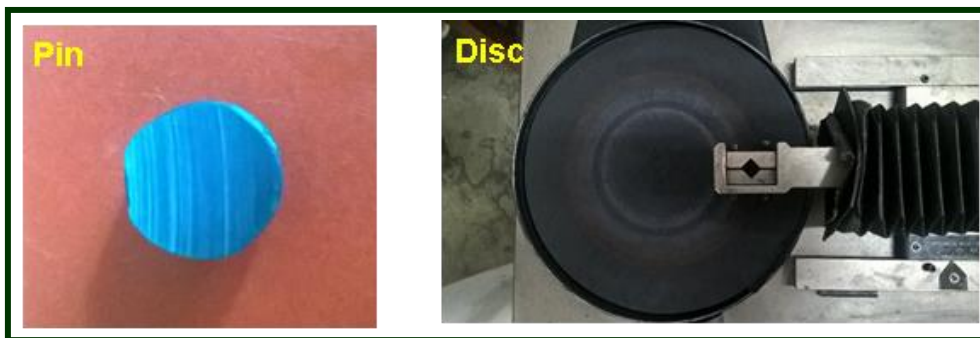


Figure 6.6. Photographs showing the worn-out surfaces of Pin & Disc tribo-pair

wear rate is calculated using the equation (1) as explained in the article [200]

$$\text{Wear rate (WR)} = \frac{\text{Weight loss (W)}}{\rho \times L} \text{ ----- (6.7)}$$

where,  $W$  = weight loss of a pin (Kg);  $\rho$  = density (Kg/m<sup>3</sup>) ;  $L$  = sliding distance( m).

The wear coefficient is calculated using the generalized Archard Equation (2) as explained in the article [201]

$$\text{Wear coefficient (K)} = \frac{V \times H}{P \times L} \quad \text{----- (6.8)}$$

Where,  $V$  = volume loss of a pin ( $\text{m}^3$ );  $H$  = Hardness of the pin (Pa);  $P$  = Load (N);  $L$  = sliding distance (m).

Figure 6.7(a) shows the wear rate values of pin material ( $\text{Mg}_2\text{Si}$ ) at various loads and sliding speed conditions. It can be observed that the wear rate value increases with normal loads and variable sliding speed conditions. It also shows that the wear rate value has increased from  $2.2 \times 10^{-11}$  to  $5.6 \times 10^{-11} \text{ m}^3/\text{m}$ , with the load variation 10 to 50 N at high sliding speed (7 m/s), registering 158% increase. But, at high normal load (50 N), the observed increase in wear rate was 22 % with respect to change in sliding speed conditions (1 to 7 m/s). The highest wear rate value of  $\sim 5.6 \times 10^{-11}$  is observed in highest sliding speed (7 m/s). The results show the linear change in wear rate with respect to change in sliding speed conditions. Figure 6.7(b) shows the wear coefficient values of the material at various sliding speed & loads conditions. Unlike wear rate, significant variation in wear coefficient (K) is not observed with sliding speed variations (1, 4 & 7 m/s). The values of wear coefficients are falling between 0.004 and 0.009, indicates similarity of abrasive, two-body wear mechanism literature values [121]. The observed loss of material due to the sliding wear is negligible at the measured experimental conditions. However prolonged wear conditions lead to catastrophic failure of the component. Thus, the present study shows the importance of wear and sliding speed, while designing the silicide-based thermoelectric device under real working environmental conditions.

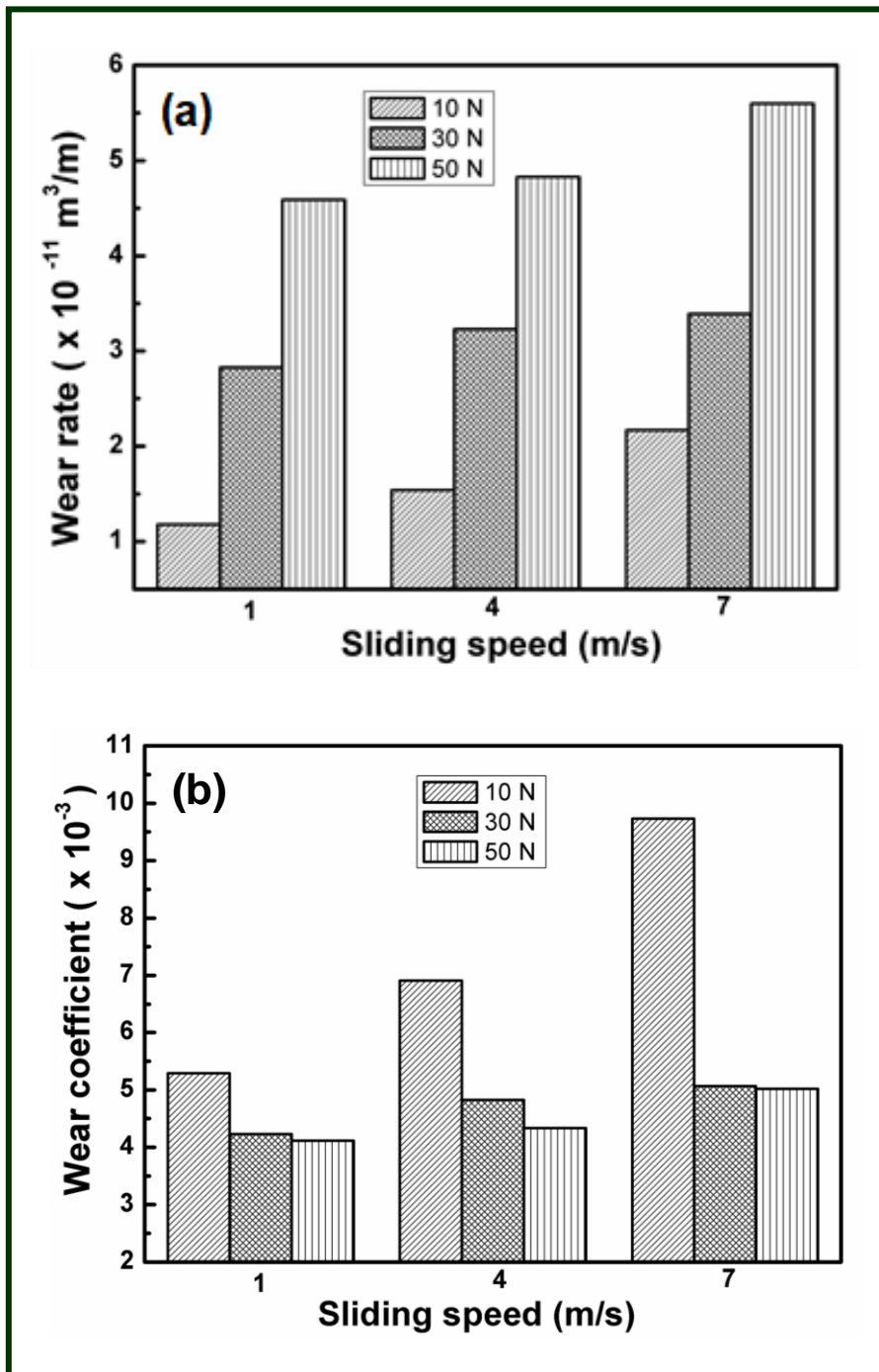


**Figure 6.7. (a) Wear rate and Wear coefficient values, as a function of sliding velocity with 10,30,50 N load conditions**

Figure 6.8 (a-c) shows the COF ( $\mu$ ) with sliding distance for both the variation in normal loads and sliding speed conditions. The continuous measurement of frictional

force was recorded using the friction transducer, and the calculated values of COF versus sliding distance are shown in Figure 6.8. It was clear that slightly higher friction fluctuations were observed at a normal load of 10 N (Figure 6.8(a)) compared to the normal load of 50 N (Figure 6.8(b)). It was clear that the significant fluctuation arises due to the material resistance against shear at lower load & speed conditions. At high speed & load conditions, hard abrasives shearing off the pin material imparts steady & high COF value throughout the sliding distance. However, the observed value of COF (0.3-0.4) with minimum variation shows a better performance of the processed material under experimental conditions. The coefficient of friction observed here is two bodies abrasive mechanism. However, minimal wear loss and fluctuations warrant the better serviceability of the synthesized materials. Also, tribo-pair elements, particularly disc having sharp abrasive particles on the entire surface and their real contact area between two sliding surfaces occur very few times during the actual working conditions. The stabilized COF and low wear loss of the material are due to the ultrafine-grained material synthesized by reactive SPS process.

### **6.8. Worn surface analysis**

In tribo-environment, the sliding of pair elements generates frictional heat, which is responsible for changes in material composition and mechanical performance of the material as a whole and surface level. To predict the phenomena occurring with silicides under wear environment, the worn surface analysis was carried out using SEM and EDS mapping. Figure 6.9 shows the worn surfaces of the pin ( $Mg_2Si$ ) under the maximum value of normal load (50 N) with sliding speed (7m/s) and corresponding maps based on EDS studies of  $Mg_2Si$  worn surfaces. The  $Mg_2Si$  worn surface exhibits the continuous grooves along with sub-crack formation, mostly at grain boundaries (Figure 6.9(a)).

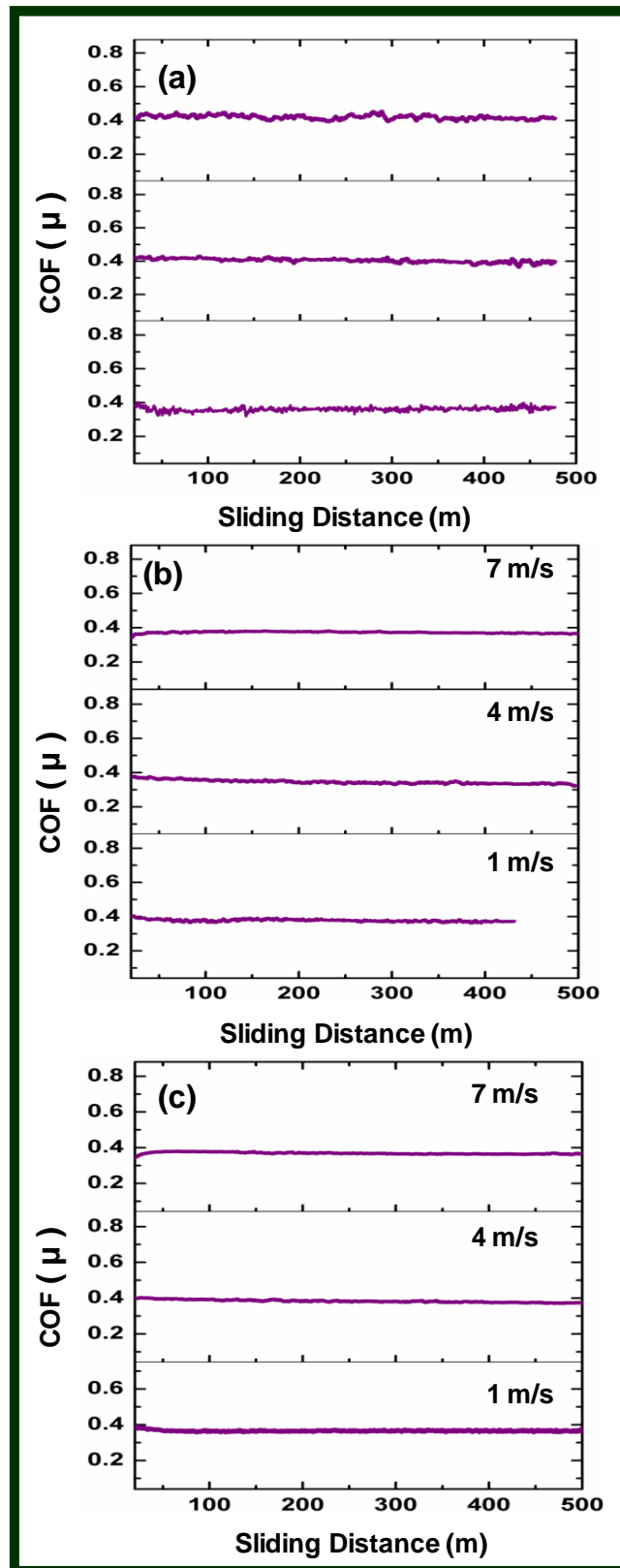
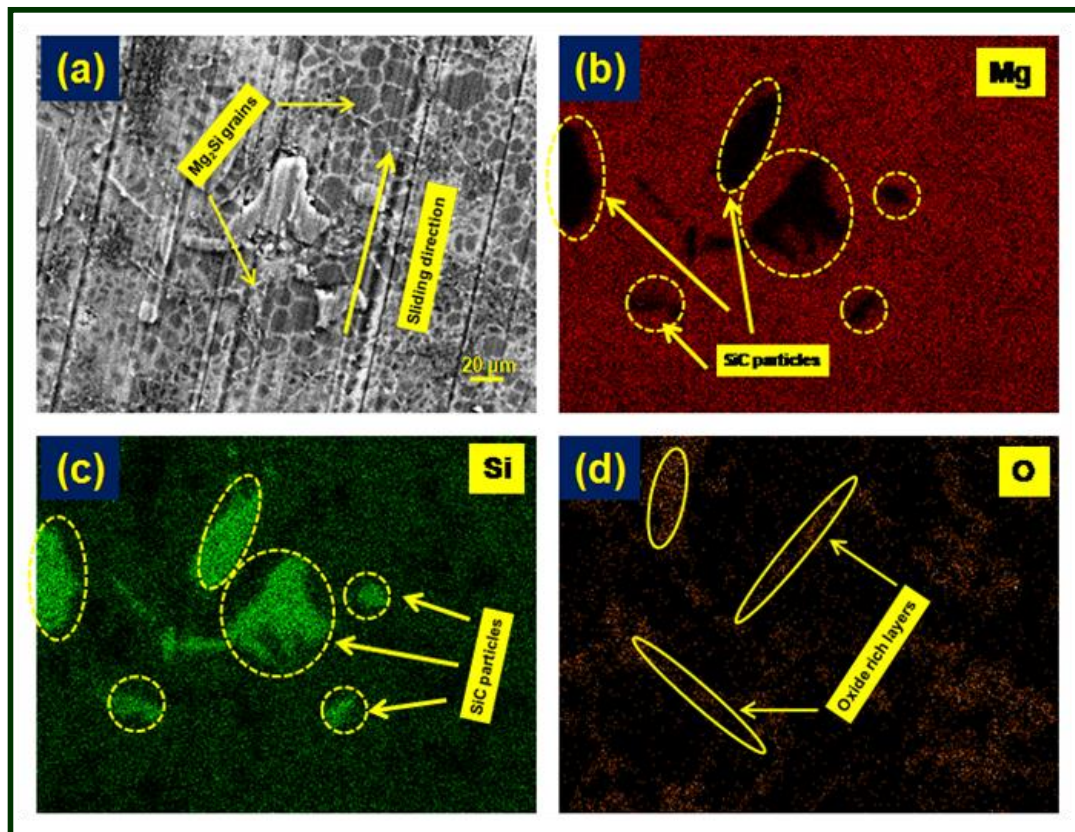


Figure 6.8. The coefficient of friction ( $\mu$ ) as a function of sliding distance (m) with different applied load conditions (a) 10 & (b) 30 and, (c) 50 N, respectively.

This surface indicates that the wear mechanism of pin material  $Mg_2Si$  was abrasive, sliding on the disc surface (SiC particles). The worn surface topography revealed the delamination type of material removal from pin surface by SiC particles. Further, the mechanism of material removal is two-body wear associated with brittle-brittle material abrasion (Figure 6.9(b&c)). The worn surface of the pin ( Figure 6.9(a)) exhibits the shearing off the material along the grain boundaries severally than intra-grains. The delamination takes place at the weak grain boundaries initially and propagates to the grains by hard abrasive particles, however, no back transferring of materials takes place. The dot maps of Mg shows the modified new surface as good as initial composition, except few SiC debris. The dot maps of Si shows the two bodies abrasive action of SiC particle over the  $Mg_2Si$  surface, without adhesiveness. The melting is not being observed between pin & disc during the sliding test. However, the surface temperature of the pin was increased locally by frictional force, which promotes the MgO formations on the surface (Figure 6.9(d)). The shearing of the material is smooth and more uniform suggests that good tribo-performance of the material. However, the high-affinity nature of Mg promotes the MgO formation at small temperature rise between the contact surfaces. The formation of MgO along the surfaces of  $Mg_2Si$  is not favorable for thermoelectric applications.

Figure 6.10(a) shows the images of disc surface with pin material debris, which is transferred from the pair during the dry sliding test. The maps based on energy dispersive spectroscopic studies reveal the SiC particles and corresponding pin material debris over disc surface ( Figure 6.10 (b-d)). The individual elemental maps indicate that the  $Mg_2Si$  material is removed as a form of small debris by brittle fracture ( Figure 6.10( b&c)). Further, a localized temperature rise caused by frictional force creates the

bulk debris bunches with massive surface oxide layers ( Figure 6.10(d)). The disc surface topography shows the SiC and Mg<sub>2</sub>Si debris along with MgO particles.



**Figure 6.9.** (a) Worn surfaces of Mg<sub>2</sub>Si after sliding experiments at maximum load (50 N) and sliding velocity (7 m/s) and (b)–(d) elemental mappings of the worn surface of Mg<sub>2</sub>Si.

The Mg dot mapping analysis at the disc surface confirms the bunches of MgO batch formation. The large surface area of detached debris and localized temperature rise are the primary cause of MgO formation. The cluster of MgO particles does not involve in tribo-action at present testing conditions, however, prolong service conditions may lead to the third body abrasive mechanism. The worn surface topography indicates the differences in the tribo-pair mating surfaces (pin and disc), in terms of structural and elemental composition. The formation of wear debris is higher at sliding speed 7 m/s and is evidenced by the wear rate in Figure 6.10. The worn surface analysis indicates the primary wear mechanism is abrasive, cracking and delamination.

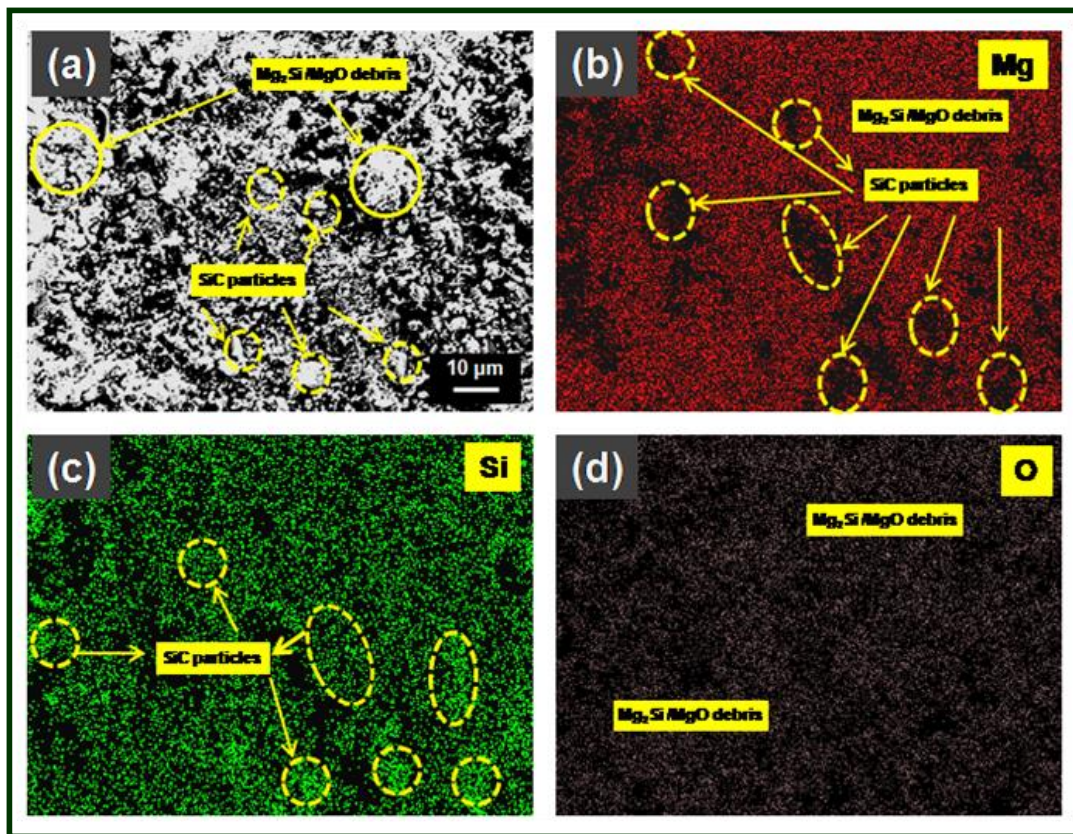


**Figure 6.10.** (a) Surfaces of disc wear track after sliding experiments at maximum load (50 N) and sliding velocity (7 m/s) and (b)–(d) elemental mappings of the worn surface of the disc.

Also, it suggests that the debris removed from the pin surfaces are not involved in wear during sliding, at the measured load and sliding speed conditions. Analysis of materials surfaces by tribology component are crucial for thermoelectric applications, and these surface level material properties are determined by the chemical composition at the interface. However, the tribological material properties of thermoelectric materials are not well characterized and understood. The present analysis will be helpful to predict such condition and validate the surface conditions at maximum performance level. The studies prove the material sustainability under the wear environment conditions and are useful for understanding the wear failure mechanism for further material development.



## 6.9. Conclusions

Mechanical investigations on synthesized n-type Mg<sub>2</sub>Si and p-type MnSi<sub>1.73</sub> were accessed by indentation hardness, indentation fracture toughness and wear & friction analysis methods, to ensure their service reliability at actual environmental conditions.

The microhardness values of synthesized n-type Mg<sub>2</sub>Si and p-type MnSi<sub>1.73</sub> were evaluated by using Vickers microhardness at three different applied loads (1, 3 & 5 N). The Mg<sub>2</sub>Si exhibits the microhardness values of 469±16, 451±10 and 446±5 Hv with load levels of 1, 3 and 5 N, respectively. The MnSi<sub>1.73</sub> exhibits the microhardness values of 1138±62, 1090±32 and 1021±16 Hv with load levels of 1, 3 and 5 N, respectively. It was confirmed that the high hardness values of the spark plasma sintered n-Mg<sub>2</sub>Si & p-MnSi<sub>1.73</sub> materials arising from the grain and grain boundaries strengthening mechanism.

The hardness and elastic modulus of synthesized *n-type* Mg<sub>2</sub>Si and *p-type* MnSi<sub>1.73</sub> were evaluated by using Nanoindentation test at different loads (10, 20, 30 and 40 mN). The hardness value of 5.4 ± 0.2 GPa and elastic modulus value of 142.5 ± 6 GPa were obtained in single step reactive spark plasma sintered Mg<sub>2</sub>Si. The hardness value of 16 ± 1 GPa and elastic modulus value of 367 ± 8 GPa were obtained in single step reactive spark plasma sintered MnSi<sub>1.73</sub>. Further, the hardness of the synthesized *n-type* Mg<sub>2</sub>Si and *p-type* MnSi<sub>1.73</sub> values are much higher than the other available thermoelectric materials.

The fracture toughness was calculated by indentation fracture technique, exhibited a high fracture toughness value of 1.71 ± 0.1 MPa√m for *n-type* Mg<sub>2</sub>Si and 3 ± 0.1 MPa√m for *p-type* MnSi<sub>1.73</sub>. The thermal shock resistance is considered as vital parameters for designing the silicide-based thermoelectric modules, and the value of

thermal shock resistance was found to be  $\sim 300$  W/m for *n-type* Mg<sub>2</sub>Si and 200 W/m for *p-type* MnSi<sub>1.73</sub>, which is higher than those reported for other available thermoelectric materials. The friction and wear properties of Mg<sub>2</sub>Si were studied to ensure its reliability during the actual hostile working conditions. The coefficient of friction and wear coefficient using dry sliding test was observed to be in the ranges of  $\sim 0.3$  to 0.4 and  $\sim 4$  to  $9 \times 10^{-3}$ , respectively. The worn surface analysis of the material suggested a two-body abrasive wear mechanism. The worn surface analysis was carried out by using energy dispersive spectroscopy mappings and correlated with wear rate, the coefficient of friction, and mechanism of wear.

The comprehensive spectrum of the mechanical properties of thermoelectric silicides including hardness, elastic modulus, fracture toughness, thermal shock resistance and tribological properties suggests the reliability of *n-type* Mg<sub>2</sub>Si and *p-type* MnSi<sub>1.73</sub> thermoelectric material for actual device applications.

# CHAPTER 7

Chapter 7 reports the highlights of this research work with important conclusions and future scope of this work

## 7.1. Conclusions

The following conclusions have been made from the present study

- The *n-type* Mg<sub>2</sub>Si and *p-type* MnSi<sub>1.73</sub> was synthesized successfully, employing plasma assisted reactive sintering process, which consumes a limited processing time as compared to long duration using conventional manufacturing techniques. The phase composition, distribution, microstructure was characterized using X-ray diffraction, high-resolution electron microscopy, and energy dispersive spectroscopy.
- The enhancement in figure-of-merit of single doping in Mg<sub>2</sub>Si is mainly due to the increase in its electronic conductivity. The single doped Mg<sub>2</sub>Si exhibits an increase in its electronic conductivity at par with dopants with electron donors, such as Sb and Bi. A detailed cross-examination of the materials microstructure, using HRTEM, evidence to dopant rich phases at the grain boundaries, facilitating inter-granular conductivity and thereby suggesting an electronic conducting mechanism similar to that proposed by the brick-layer model for ceramics. The enhancement in thermoelectric performance in terms of figure-of-merit ( $ZT$ )  $\approx 0.7$  was realized by use of the double-doping approach. The increase in figure-of-merit ( $ZT$ ) by double-doping approach is mainly due to the significant increase in the electrical conductivity.
- The benefits of rapid solidification technique using melt-spinning have been exploited to significantly improve the thermoelectric properties of *p-type*

Aluminium doped  $\text{MnSi}_{1.73}$ , which significantly improves the microstructure and aids an improved control on the phase composition of  $\text{MnSi}_{1.73}$ , which are identified to enhance its thermoelectric properties. The highest ZT  $\sim 0.82$  at 800 K was obtained in melt-spinning combined with spark plasma sintered  $\text{MnSi}_{1.73}$ , melt-spun at a high cooling rate of  $\sim 2 \times 10^7$  K/s. This extraordinary thermoelectric property in the processed  $\text{MnSi}_{1.73}$  resulting from an ultrafine-grained microstructure due to high cooling rates of solidification, which composing of  $\text{MnSi}_{1.73}$  matrix (20-30 nm) with additional Silicon nanoparticles (3-9 nm) homogeneously distributed in the matrix. The  $\text{MnSi}_{1.73}$  matrix and Silicon with nanocrystallite boundaries, at different dimensional scales, scatter the wide-ranging spectrum of low and medium scale wavelength phonons and therefore exhibiting in a low-value thermal conductivity, which mainly contributes to the improvement of ZT. Therefore, the nanostructured features of HMS as a result of the high cooling rate of solidification, the control of phase composition and devoid of the metallic cubic-Mn-Si phase offers a significant improvement in thermoelectric properties in the melt-spinning combined with spark plasma sintered HMS.

- The mechanical performance analysis of *n-type*  $\text{Mg}_2\text{Si}$  and *p-type*  $\text{MnSi}_{1.73}$  was carried out in the present study, to ensure the structural integrity of the material which is subjected to thermal and mechanical stresses under real working conditions. Hence, the mechanical properties of the thermoelectric material are similarly essential to circumvent the mechanical failure of their thermoelectric devices during real working conditions. Mechanical properties investigations on synthesized *n-type*  $\text{Mg}_2\text{Si}$  and *p-type*  $\text{MnSi}_{1.73}$  were accessed by indentation

hardness, indentation fracture toughness, thermal shock resistance and wear & friction analysis, in the present study.

- The hardness and elastic modulus of synthesized *n-type* Mg<sub>2</sub>Si and *p-type* MnSi<sub>1.73</sub> were evaluated by using Nanoindentation test. The hardness value of  $5.4 \pm 0.2$  GPa and elastic modulus value of  $142.5 \pm 6$  GPa were obtained in reactive spark plasma sintered Mg<sub>2</sub>Si. The hardness value of  $16 \pm 1$  GPa and elastic modulus value of  $367 \pm 8$  GPa were obtained in spark plasma sintered MnSi<sub>1.73</sub>. The fracture toughness was calculated by indentation fracture technique and suggested a high fracture toughness value of  $1.71 \pm 0.1$  MPa√m for *n-type* Mg<sub>2</sub>Si and  $3 \pm 0.1$  MPa√m for *p-type* MnSi<sub>1.73</sub>.
- The thermal shock resistance is considered as vital parameters for designing the thermoelectric modules, and thermal shock resistance value was observed to be  $\sim 300$  W/m for *n-type* Mg<sub>2</sub>Si and  $200$  W/m for *p-type* MnSi<sub>1.73</sub>, which is higher than those reported for other available thermoelectric materials. The tribological properties were accessed for its wear and friction resistance, and the coefficient of friction and wear coefficient values was observed to be in the ranges of  $\sim 0.3$  to  $0.4$  and  $\sim 4$  to  $9 \times 10^{-3}$ , respectively. The worn surface analysis was carried out by using EDS mappings and correlated with wear rate, COF, and mechanism of wear.
- The comprehensive investigation of the mechanical properties of thermoelectric silicides including elastic modulus, hardness, fracture toughness, thermal shock resistance and tribological properties confirms the durability of *n-type* Mg<sub>2</sub>Si and *p-type* MnSi<sub>1.73</sub> thermoelectric material for real device applications.

- The outcomes of the synthesized *n-type* Mg<sub>2</sub>Si and *p-type* MnSi<sub>1.73</sub> system with high thermoelectric figure-of-merit pave the pathway to realize the low-cost, efficient, and eco-friendly solar-thermoelectric power conversion, in the high-temperature range (500 – 800 K).

## 7.2. Scope of future work

The grain boundaries control a material's properties, either transport or mechanical properties of these metal silicides. The precise control of grain boundary via microstructural engineering is helpful for eliminating the poor ductility and brittleness, in thermoelectric metal silicides. It is proposed to perform an impedance spectroscopic analysis highlighting the nature and role of grain boundaries in doped Mg<sub>2</sub>Si systems, which are future scope in these potential thermoelectric materials. The work remains in evaluating the thermal stresses and creep behavior of cost-effective metal silicide thermoelectric materials to develop a reliable thermoelectric device for power generation. The process technology for synthesizing the individual thermoelements of *n-type* Mg<sub>2</sub>Si and *p-type* MnSi<sub>1.73</sub> along with their ohmic contacts in a single processing step employing spark plasma sintering at improved process parameters is to be addressed in future.

## References

- [1] D.M. Rowe, CRC Handbook of Thermoelectrics, CRC Press. 16 (1995).
- [2] G.J. Snyder, E.S. Toberer, Complex thermoelectric materials, *Nat. Mater.* 7 (2008) 105–114.
- [3] G.J. Snyder, T.S. Ursell, Thermoelectric efficiency and compatibility, *Phys. Rev. Lett.* 91 (2003) 148301.
- [4] D.M. Rowe, Thermoelectrics handbook: macro to nano, CRC Press. 80 (2005).
- [5] D.K. Aswal, R. Basu, A. Singh, Key issues in development of thermoelectric power generators: High figure-of-merit materials and their highly conducting interfaces with metallic interconnects, *Energy Convers. Manag.* 114 (2016) 50–67.
- [6] W. Liu, Q. Jie, H.S. Kim, Z. Ren, Current progress and future challenges in thermoelectric power generation: From materials to devices, *Acta Mater.* 87 (2015) 357–376.
- [7] D. Kraemer, Q. Jie, K. Mcenaney, F. Cao, W. Liu, L.A. Weinstein, J. Loomis, Z. Ren, G. Chen, Concentrating solar thermoelectric generators with a peak efficiency of 7.4%, *Nat. Energy.* 1 (2016) 16153.
- [8] K. McEnaney, D. Kraemer, Z. Ren, G. Chen, Modeling of concentrating solar thermoelectric generators, *J. Appl. Phys.* 110 (2011) 74502.
- [9] L.L. Baranowski, G.J. Snyder, E.S. Toberer, Concentrated solar thermoelectric generators, *Energy Environ. Sci.* 5 (2012) 9055–9067.
- [10] M. Telkes, Solar thermoelectric generators, *J. Appl. Phys.* 25 (1954) 765–777.
- [11] D. Kraemer, K. McEnaney, M. Chiesa, G. Chen, Modeling and optimization of solar thermoelectric generators for terrestrial applications, *Sol. Energy.* 86 (2012) 1338–1350.
- [12] L. Liu, X. Sen Lu, M.L. Shi, Y.K. Ma, J.Y. Shi, Modeling of flat-plate solar thermoelectric generators for space applications, *Sol. Energy.* 132 (2016) 386–394.
- [13] D. Kraemer, B. Poudel, H.-P. Feng, J.C. Caylor, B. Yu, X. Yan, Y. Ma, X. Wang, D. Wang, A. Muto, K. McEnaney, M. Chiesa, Z. Ren, G. Chen, High-performance flat-panel solar thermoelectric generators with high thermal

- concentration, *Nat. Mater.* 10 (2011) 532–538.
- [14] T.M. Tritt, H. Böttner, L. Chen, *Thermoelectrics: Direct Solar Thermal Energy Conversion*, *MRS Bull.* 33 (2008) 366–368.
- [15] D. Xia, C. Liu, S. Fan, A solar thermoelectric conversion material based on Bi<sub>2</sub>Te<sub>3</sub> and carbon nanotube composites, *J. Phys. Chem. C.* 118 (2014) 20826–20831.
- [16] L. Tayebi, Z. Zamanipour, D. Vashaee, Design optimization of micro-fabricated thermoelectric devices for solar power generation, *Renew. Energy.* 69 (2014) 166–173.
- [17] P. Sundarraj, D. Maity, S.S. Roy, R.A. Taylor, Recent advances in thermoelectric materials and solar thermoelectric generators – a critical review, *RSC Adv.* 4 (2014) 46860–46874.
- [18] E.K. Kuravi, S.; Trahan, J.; Goswami, D. Y.; Rahman, M. M.; Stefanakos, Thermal energy storage technologies and systems for concentrating solar power plants, *Prog. Energy Combust. Sci.* 39 (2013) 285–319.
- [19] M. Zebarjadi, K. Esfarjani, M.S. Dresselhaus, Z.F. Ren, G. Chen, Perspectives on thermoelectrics: from fundamentals to device applications, *Energy Environ. Sci.* 5 (2012) 5147–5162.
- [20] D. Narducci, Do we really need high thermoelectric figures of merit? A critical appraisal to the power conversion efficiency of thermoelectric materials, *Appl. Phys. Lett.* 99 (2011) 102104.
- [21] A. V Dmitriev, I.P. Zvyagin, Current trends in the physics of thermoelectric materials, *Physics-Uspekhi.* 53 (2010) 789–803.
- [22] R.J. Mehta, Y. Zhang, C. Karthik, B. Singh, R.W. Siegel, T. Borca-Tasciuc, G. Ramanath, A new class of doped nanobulk high-figure-of-merit thermoelectrics by scalable bottom-up assembly, *Nat. Mater.* 11 (2012) 233–240.
- [23] K.-H. Lee, H.-S. Kim, S.-I. Kim, E.-S. Lee, S.-M. Lee, J.-S. Rhyee, J.-Y. Jung, I.-H. Kim, Y. Wang, K. Koumoto, Enhancement of Thermoelectric Figure of Merit for Bi<sub>0.5</sub>Sb<sub>1.5</sub>Te<sub>3</sub> by Metal Nanoparticle Decoration, *J. Electron. Mater.* 41 (2012) 1165–1169.
- [24] S.N. Girard, J. He, X. Zhou, D. Shoemaker, C.M. Jaworski, C. Uher, V.P. Dravid, J.P. Heremans, M.G. Kanatzidis, High performance Na-doped PbTe-PbS thermoelectric materials: Electronic density of states modification and shape-controlled nanostructures, *J. Am. Chem. Soc.* 133 (2011) 16588–16597.



- [25] Z. Chen, Z. Jian, W. Li, Y. Chang, B. Ge, R. Hanus, J. Yang, Y. Chen, M. Huang, G.J. Snyder, Y. Pei, Lattice Dislocations Enhancing Thermoelectric PbTe in Addition to Band Convergence, *Adv. Mater.* 29 (2017) 1606768.
- [26] S. Bathula, M. Jayasimhadri, N. Singh, A.K. Srivastava, J. Pulikkotil, A. Dhar, R.C. Budhani, Enhanced thermoelectric figure-of-merit in spark plasma sintered nanostructured n-type SiGe alloys, *Appl. Phys. Lett.* 101 (2012) 213902.
- [27] K.F. Hsu, S. Loo, F. Guo, W. Chen, J.S. Dyck, C. Uher, T. Hogan, E.K. Polychroniadis, M.G. Kanatzidis, Cubic AgPbmSbTe<sub>2+m</sub>: Bulk Thermoelectric Materials with High Figure of Merit, *Science* (80-. ). 303 (2004) 818–821.
- [28] B. Gahtori, S. Bathula, K. Tyagi, M. Jayasimhadri, A.K. Srivastava, S. Singh, R.C. Budhani, A. Dhar, Giant enhancement in thermoelectric performance of copper selenide by incorporation of different nanoscale dimensional defect features, *Nano Energy.* 13 (2015) 36–46.
- [29] X. Chen, A. Weathers, J. Carrete, S. Mukhopadhyay, O. Delaire, D.A. Stewart, N. Mingo, S.N. Girard, J. Ma, D.L. Abernathy, J. Yan, R. Sheshka, D.P. Sellan, F. Meng, S. Jin, J. Zhou, L. Shi, Twisting phonons in complex crystals with quasi-one-dimensional substructures, *Nat. Commun.* 6 (2015) 6723.
- [30] P. Ramachandrarao, Rapid solidification of steels, *Bull. Mater. Sci.* 15 (1992) 503–513.
- [31] R.C. Budhani, T.C. Goel, K.L. Chopra, Melt-spinning technique for preparation of metallic glasses, *Bull. Mater. Sci.* 4 (1982) 549–561.
- [32] J. Xie, Y. Ohishi, Y. Miyazaki, A. Yusufu, H. Muta, K. Kurosaki, S. Yamanaka, Thermoelectric properties of Si/SiB 3 sub-micro composite prepared by melt-spinning technique, *J. Appl. Phys.* 118 (2015) 65103.
- [33] L. Yang, Z.G. Chen, M. Hong, G. Han, J. Zou, Enhanced Thermoelectric Performance of Nanostructured Bi<sub>2</sub>Te<sub>3</sub> through Significant Phonon Scattering, *ACS Appl. Mater. Interfaces.* 7 (2015) 23694–23699.
- [34] S.K. Mishra, S. Satpathy, O. Jepsen, Electronic structure and thermoelectric properties of bismuth telluride and bismuth selenide, *J. Phys. Condens. Matter.* 9 (1997) 461–470.
- [35] S. Gupta, N. Vijayan, A. Krishna, K. Thukral, K.K. Maurya, S. Muthiah, A. Dhar, B. Singh, G. Bhagavannarayana, Enhancement of thermoelectric figure of merit in Bi<sub>2</sub>Se<sub>3</sub> crystals through a necking process, *J. Appl. Crystallogr.* 48 (2015) 533–541.

- [36] R.J. Mehta, Y. Zhang, H. Zhu, D.S. Parker, M. Belley, D.J. Singh, R. Ramprasad, T. Borca-Tasciuc, G. Ramanath, Seebeck and figure of merit enhancement in nanostructured antimony telluride by antisite defect suppression through sulfur doping, *Nano Lett.* 12 (2012) 4523–4529.
- [37] P. Ying, X. Liu, C. Fu, X. Yue, H. Xie, X. Zhao, W. Zhang, T. Zhu, High performance  $\alpha$ -MgAgSb thermoelectric materials for low temperature power generation, *Chem. Mater.* 27 (2015) 909–913.
- [38] D.Y. Chung, T.P. Hogan, M. Rocci-Lane, P. Brazis, J.R. Ireland, C.R. Kannewurf, M. Bastea, C. Uher, M.G. Kanatzidis, A new thermoelectric material: CsBi<sub>4</sub>Te<sub>6</sub>, *J. Am. Chem. Soc.* 126 (2004) 6414–6428.
- [39] T. Schroder, T. Rosenthal, N. Giesbrecht, M. Nentwig, S. Maier, H. Wang, G.J. Snyder, O. Oeckler, Nanostructures in Te/Sb/Ge/Ag (TAGS) thermoelectric materials induced by phase transitions associated with vacancy ordering, *Inorg. Chem.* 53 (2014) 7722–7729.
- [40] K. Biswas, J. He, I.D. Blum, Chun-IWu, T.P. Hogan, D.N. Seidman, V.P. Dravid, M.G. Kanatzidis, Corrigendum: High-performance bulk thermoelectrics with all-scale hierarchical architectures, *Nature*. 490 (2012) 570–570.
- [41] L. Chen, X. Zeng, T.M. Tritt, S.J. Poon, Half-Heusler Alloys for Efficient Thermoelectric Power Conversion, *J. Electron. Mater.* 45 (2016) 5554–5560.
- [42] T. Caillat, J.-P. Fleurial, A. Borshchevsky, Preparation and thermoelectric properties of semiconducting Zn<sub>4</sub>Sb<sub>3</sub>, *J. Phys. Chem. Solids.* 58 (1997) 1119–1125.
- [43] M.I. Fedorov, G.N. Isachenko, Silicides: Materials for thermoelectric energy conversion, *Jpn. J. Appl. Phys.* 54 (2015) 07JA05.
- [44] A. Nozariasbmarz, A. Agarwal, Z.A. Coutant, M.J. Hall, J. Liu, R. Liu, A. Malhotra, P. Norouzzadeh, M.C. Öztürk, V.P. Ramesh, Y. Sargolzaeiaval, F. Suarez, D. Vashaee, Thermoelectric silicides: A review, *Jpn. J. Appl. Phys.* 56 (2017) 05DA04.
- [45] X. Cheng, N. Farahi, H. Kleinke, Mg<sub>2</sub>Si-Based Materials for the Thermoelectric Energy Conversion, *JOM.* 68 (2016) 2680–2687.
- [46] X. She, X. Su, H. Du, T. Liang, G. Zheng, Y. Yan, R. Akram, C. Uher, X. Tang, High thermoelectric performance of higher manganese silicides prepared by ultra-fast thermal explosion, *J. Mater. Chem. C.* 3 (2015) 12116–12122.
- [47] A.J. Zhou, X.B. Zhao, T.J. Zhu, Y.Q. Cao, C. Stiewe, R. Hassdorf, E. Mueller,

- Composites of higher manganese silicides and nanostructured secondary phases and their thermoelectric properties, in: *J. Electron. Mater.*, 2009: pp. 1072–1077.
- [48] H. Lee, G. Kim, B. Lee, J. Kim, S.M. Choi, K.H. Lee, W. Lee, Effect of Si content on the thermoelectric transport properties of Ge-doped higher manganese silicides, *Scr. Mater.* 135 (2017) 72–75.
- [49] A. Allam, C.A. Nunes, J. Zalesak, M.C. Record, On the stability of the Higher Manganese Silicides, *J. Alloys Compd.* 512 (2012) 278–281.
- [50] A.J. Zhou, X.B. Zhao, T.J. Zhu, S.H. Yang, T. Dasgupta, C. Stiewe, R. Hassdorf, E. Mueller, Microstructure and thermoelectric properties of SiGe-added higher manganese silicides, *Mater. Chem. Phys.* 124 (2010) 1001–1005.
- [51] A.J. Zhou, T.J. Zhu, X.B. Zhao, S.H. Yang, T. Dasgupta, C. Stiewe, R. Hassdorf, E. Mueller, Improved thermoelectric performance of higher manganese silicides with Ge additions, *J. Electron. Mater.* 39 (2010) 2002–2007.
- [52] A. Allam, P. Boulet, C.A. Nunes, J. Sopousek, P. Broz, M.C. Record, Phase transformations in Higher Manganese Silicides, *J. Alloys Compd.* 551 (2013) 30–36.
- [53] X. Chen, J. Zhou, J.B. Goodenough, L. Shi, Enhanced thermoelectric power factor of Re-substituted higher manganese silicides with small islands of MnSi secondary phase, *J. Mater. Chem. C* 3 (2015) 10500–10508.
- [54] Y. Miyazaki, H. Hamada, K. Hayashi, K. Yubuta, Crystal Structure and Thermoelectric Properties of Lightly Vanadium-Substituted Higher Manganese Silicides ( $Mn_{1-x}V_xSi_\gamma$ ), *J. Electron. Mater.* 46 (2017) 2705–2709.
- [55] S. Nishino, M. Miyata, K. Ohdaira, M. Koyano, T. Takeuchi, Thermal Conductivity Measurement of Liquid-Quenched Higher Manganese Silicides, *J. Electron. Mater.* 45 (2016) 1821–1826.
- [56] X. Chen, S.N. Girard, F. Meng, E. Lara-Curzio, S. Jin, J.B. Goodenough, J. Zhou, L. Shi, Approaching the minimum thermal conductivity in rhenium-substituted higher manganese silicides, *Adv. Energy Mater.* 4 (2014) 1400452.
- [57] P. Eaksuwanchai, K. Kurosaki, S. Tanusilp, Y. Ohishi, H. Muta, S. Yamanaka, Thermoelectric properties of Si-NiSi<sub>2</sub> bulk nanocomposites synthesized by a combined method of melt spinning and spark plasma sintering, *J. Appl. Phys.* 121 (2017) 225110.
- [58] A.F. May, J.P. Fleurial, G.J. Snyder, Thermoelectric performance of lanthanum telluride produced via mechanical alloying, *Phys. Rev. B - Condens. Matter*

- Mater. Phys. 78 (2008) 125205.
- [59] M. Ohtaki, Recent aspects of oxide thermoelectric materials for power generation from mid-to-high temperature heat source, *J. Ceram. Soc. Japan.* 119 (2011) 770–775.
- [60] J.H. Grebenkemper, Y. Hu, D. Barrett, P. Gogna, C.-K. Huang, S.K. Bux, S.M. Kauzlarich, High Temperature Thermoelectric Properties of Yb<sub>14</sub>MnSb<sub>11</sub> Prepared from Reaction of MnSb with the Elements, *Chem. Mater.* 27 (2015) 5791–5798.
- [61] R. Kabir, T. Zhang, R. Donelson, D. Wang, R. Tian, T.T. Tan, B. Gong, S. Li, Thermoelectric properties of Yb and Nb codoped CaMnO<sub>3</sub>, *Phys. Status Solidi Appl. Mater. Sci.* 211 (2014) 1200–1206.
- [62] S. Bathula, J. Mula, B.G. Bhasker, N.K. Singh, K. Tyagi, A.K. Srivastava, A. Dhar, Role of nanoscale defect features in enhancing the thermoelectric performance of p-type nanostructured SiGe alloys, *Nanoscale.* 7 (2015) 12474–12483.
- [63] D.M. Rowe, Applications of nuclear-powered thermoelectric generators in space, *Appl. Energy.* 40 (1991) 241–271.
- [64] J. Liebl, S. Neugebauer, A. Eder, M. Linde, B. Mazar, W. Stütz, The thermoelectric generator from BMW is making use of waste heat, *MTZ Worldw.* 70 (2009) 4–11.
- [65] Y.S. Jung, D.H. Jeong, S.B. Kang, F. Kim, M.H. Jeong, K.S. Lee, J.S. Son, J.M. Baik, J.S. Kim, K.J. Choi, Wearable solar thermoelectric generator driven by unprecedentedly high temperature difference, *Nano Energy.* 40 (2017) 663–672.
- [66] Y. Li, S. Witharana, H. Cao, M. Lasfargues, Y. Huang, Y. Ding, Wide spectrum solar energy harvesting through an integrated photovoltaic and thermoelectric system, *Particuology.* 15 (2014) 39–44.
- [67] W. Liu, K. Yin, Q. Zhang, C. Uher, X. Tang, Eco-friendly high-performance silicide thermoelectric materials, *Natl. Sci. Rev.* 4 (2017) 611–626.
- [68] S. Leblanc, S.K. Yee, M.L. Scullin, C. Dames, K.E. Goodson, Material and manufacturing cost considerations for thermoelectrics, *Renew. Sustain. Energy Rev.* 32 (2014) 313–327.
- [69] S. Chen, Z. Ren, Recent progress of half-Heusler for moderate temperature thermoelectric applications, *Mater. Today.* 16 (2013) 387–395.
- [70] B. Yu, W. Liu, S. Chen, H. Wang, H. Wang, G. Chen, Z. Ren, Thermoelectric

- properties of copper selenide with ordered selenium layer and disordered copper layer, *Nano Energy*. 1 (2012) 472–478.
- [71] O. Guillon, J. Gonzalez-Julian, B. Dargatz, T. Kessel, G. Schierning, J. Räthel, M. Herrmann, Field-assisted sintering technology/spark plasma sintering: Mechanisms, materials, and technology developments, *Adv. Eng. Mater.* 16 (2014) 830–849.
- [72] M. Suárez, A. Fernández, J.L. Menéndez, R. Torrecillas, H.U. Kessel, J. Hennicke, R. Kirchner, T. Kessel, Challenges and Opportunities for Spark Plasma Sintering : A Key Technology for a New Generation of Materials, *Sinter. Appl.* (2013) 319–342.
- [73] C. Dames, Cost optimization of thermoelectric materials for power generation: The case for ZT at (almost) any cost, *Scr. Mater.* 111 (2016) 16–22.
- [74] J. De Boor, C. Gloanec, H. Kolb, R. Sottong, P. Ziolkowski, E. Müller, Fabrication and characterization of nickel contacts for magnesium silicide based thermoelectric generators, *J. Alloys Compd.* 632 (2015) 348–353.
- [75] J. De Boor, T. Dasgupta, H. Kolb, C. Compere, K. Kelm, E. Mueller, Microstructural effects on thermoelectric efficiency: A case study on magnesium silicide, *Acta Mater.* 77 (2014) 68–75.
- [76] K.B. Holger Putz, *Pearson’s Crystal data: Crystal structure Database for Inorganic compounds*, ASM International, Materials Park, OH 44073-0022 USA, 2012.
- [77] <http://resource.npl.co.uk/mtdata/phdiagrams/mgsi.htm>, (n.d.).
- [78] M. Riffel, J. Schilz, Mechanical alloying of Mg<sub>2</sub>Si, *Scr. Metall. Mater.* 32 (1995) 1951–1956.
- [79] X. Niu, L. Lu, Formation of magnesium silicide by mechanical alloying, *Adv. Perform. Mater.* 4 (1997) 275–283.
- [80] C.R. Clark, C. Wright, C. Suryanarayana, E.G. Baburaj, F.H. Froes, Synthesis of Mg<sub>2</sub>X (X = Si, Ge, or Sn) intermetallics by mechanical alloying, *Mater. Lett.* 33 (1997) 71–75.
- [81] M. Riffel, S. J, Mill setting and microstructural evolution during mechanical alloying of Mg<sub>2</sub>Si, *J. Mater. Sci.* 33 (1998) 3427–3431.
- [82] J.M. Muñoz-Palos, M. Del Carmen Cristina, P. Adeva, Synthesis of Mg<sub>2</sub>Si powder by mechanical alloying and its consolidation, *Mater. Trans. JIM.* 37 (1996) 1602–1606.

- [83] K. Kondoh, H. Oginuma, E. Yuasa, T. Aizawa, Solid-State Synthesis of Mg<sub>2</sub>Si from Mg-Si Mixture Powder, *Mater. Trans.* 42 (2001) 1293–1300.
- [84] K. Kondoh, H. Oginuma, A. Kimura, S. Matsukawa, T. Aizawa, In-situ Synthesis of Mg<sub>2</sub>Si Intermetallics via Powder Metallurgy Process, *Mater. Trans.* 44 (2003) 981–985.
- [85] J.-Y. Jung, I.-H. Kim, S.-M. Choi, W.-S. Seo, S.-U. Kim, Synthesis of Thermoelectric Mg<sub>2</sub>Si by Mechanical Alloying, *J. Korean Phys. Soc.* 57 (2010) 1005–1009.
- [86] T. Kajikawa, I. Katsube, S. Sugihara, K. Soejima, Thermoelectric properties of sintered magnesium compounds, in: *Int. Conf. Thermoelectr. ICT, Proc.*, 1996: pp. 128–132.
- [87] T. Kajikawa, K. Shida, S. Sugihara, M. Ohmori, T. Hirai, Thermoelectric properties of magnesium silicide processed by powdered elements plasma activated sintering method, *16th Int. Conf. Thermoelectr.* (1997) 275–278.
- [88] L.M. Zhang, C.B. Wang, H.Y. Jiang, Q. Shen, Thermoelectric properties of Sb-doped Mg<sub>2</sub>Si by solid state reaction, in: *Int. Conf. Thermoelectr. ICT, Proc.*, 2003: pp. 146–148.
- [89] M. Yang, L. Zhang, Q. Shen, Synthesis and sintering of Mg<sub>2</sub>Si thermoelectric generator by spark plasma sintering, *J. Wuhan Univ. Technol. Mater. Sci. Ed.* 23 (2008) 870–873.
- [90] M.J. Yang, L.M. Zhang, L.Q. Han, Q. Shen, C.B. Wang, Simple fabrication of Mg<sub>2</sub>Si thermoelectric generator by spark plasma sintering, *Indian J. Eng. Mater. Sci.* 16 (2009) 277–280.
- [91] N. V. Morozova, S. V. Ovsyannikov, I. V. Korobeinikov, A.E. Karkin, K.I. Takarabe, Y. Mori, S. Nakamura, V. V. Shchennikov, Significant enhancement of thermoelectric properties and metallization of Al-doped Mg<sub>2</sub>Si under pressure, *J. Appl. Phys.* 115 (2014) 213705.
- [92] G.H. Li, Q.P. Kong, Processing and thermal stability of NANO-Mg<sub>2</sub>Si intermetallic compound, *Scr. Metall. Mater.* 32 (1995) 1435–1440.
- [93] L. Wang, X.Y. Qin, The effect of mechanical milling on the formation of nanocrystalline Mg<sub>2</sub>Si through solid-state reaction, *Scr. Mater.* 49 (2003) 243–248.
- [94] W. Xiong, X.Y. Qin, M.G. Kong, L. Chen, Synthesis and properties of bulk nanocrystalline Mg<sub>2</sub>Si through ball-milling and reactive hot-pressing, *Trans.*

- Nonferrous Met. Soc. China (English Ed. 16 (2006) 987–991.
- [95] M. Yang, L. Zhang, Q. Shen, Nanostructuring and thermoelectric properties of bulk N-type Mg<sub>2</sub>Si, *J. Wuhan Univ. Technol. Sci. Ed.* 24 (2009) 912–916.
- [96] E. Savary, F. Gascoin, S. Marinell, Fast synthesis of nanocrystalline Mg<sub>2</sub>Si by microwave heating: a new route to nano-structured thermoelectric materials, *Dalt. Trans.* 39 (2010) 11074.
- [97] V. Milekhine, M.I. Onsøyen, J.K. Solberg, T. Skaland, Mechanical properties of FeSi ( $\epsilon$ ), FeSi<sub>2</sub> ( $\zeta\alpha$ ) and Mg<sub>2</sub>Si, *Intermetallics*. (2002).
- [98] L. Wang, X.Y. Qin, W. Xiong, X.G. Zhu, Fabrication and mechanical properties of bulk nanocrystalline intermetallic Mg<sub>2</sub>Si, *Mater. Sci. Eng. A.* 459 (2007) 216–222.
- [99] R.D. Schmidt, E.D. Case, J. Giles, J.E. Ni, T.P. Hogan, Room-temperature mechanical properties and slow crack growth behavior of Mg<sub>2</sub>Si thermoelectric materials, *J. Electron. Mater.* 41 (2012) 1210–1216.
- [100] R.D. Schmidt, X. Fan, E.D. Case, P.B. Sarac, Mechanical properties of Mg<sub>2</sub>Si thermoelectric materials with the addition of 0–4 vol% silicon carbide nanoparticles (SiCNP), *J. Mater. Sci.* 50 (2015) 4034–4046.
- [101] K.N. and Y.K. Masashi Ishikawa, Takashi Nakamura, Shusaku Hirata, Tsutomu Iida, Mechanical properties of Mg<sub>2</sub>Si with metallic binders, *Jpn. J. Appl. Phys.* 54 (2015) 07JC03.
- [102] J.M. Higgins, A.L. Schmitt, I.A. Guzei, S. Jin, Higher manganese silicide nanowires of nowotny chimney ladder phase, *J. Am. Chem. Soc.* 130 (2008) 16086–16094.
- [103] Y. Miyazaki, D. Igarashi, K. Hayashi, T. Kajitani, K. Yubuta, Modulated crystal structure of chimney-ladder higher manganese silicides MnSi $\gamma$  ( $\gamma\sim 1.74$ ), *Phys. Rev. B - Condens. Matter Mater. Phys.* 78 (2008) 214104.
- [104] D.B. Migas, V.L. Shaposhnikov, A.B. Filonov, V.E. Borisenko, N.N. Dorozhkin, Ab initio study of the band structures of different phases of higher manganese silicides, *Phys. Rev. B.* 77 (2008) 75205.
- [105] K. Koumoto, R. Funahashi, E. Guilmeau, Y. Miyazaki, A. Weidenkaff, Y. Wang, C. Wan, Thermoelectric ceramics for energy harvesting, *J. Am. Ceram. Soc.* 96 (2013) 1–23.
- [106] <http://resource.npl.co.uk/mtdata/phdiagrams/mnsi.htm>, (n.d.).
- [107] W. Luo, H. Li, Y. Yan, Z. Lin, X. Tang, Q. Zhang, C. Uher, Rapid synthesis of

- high thermoelectric performance higher manganese silicide with in-situ formed nano-phase of MnSi, *Intermetallics*. 19 (2011) 404–408.
- [108] Y. Sadia, Y. Gelbstein, Silicon-rich higher manganese silicides for thermoelectric applications, *J. Electron. Mater.* 41 (2012) 1504–1508.
- [109] W. Luo, H. Li, F. Fu, W. Hao, X. Tang, Improved thermoelectric properties of Al-doped higher manganese silicide prepared by a rapid solidification method, *J. Electron. Mater.* 40 (2011) 1233–1237.
- [110] V. Ponnambalam, D.T. Morelli, Effect of Cr and Fe substitution on the transport properties of the nowotny chimney-ladder MnSi  $\delta$  ( $1.73 < \delta < 1.75$ ) compounds, *J. Electron. Mater.* 41 (2012) 1389–1394.
- [111] G. Liu, Q. Lu, X. Zhang, J. Zhang, Y. Shi, In situ synthesis and thermoelectric properties of Cr-doped higher manganese silicides, *J. Electron. Mater.* 41 (2012) 1450–1455.
- [112] T. Itoh, M. Yamada, Synthesis of thermoelectric manganese silicide by mechanical alloying and pulse discharge sintering, *J. Electron. Mater.* 38 (2009) 925–929.
- [113] A. Famengo, S. Battiston, M. Saleemi, S. Boldrini, S. Fiameni, F. Agresti, M.S. Toprak, S. Barison, M. Fabrizio, Phase content influence on thermoelectric properties of manganese silicide-based materials for middle-high temperatures, *J. Electron. Mater.* 42 (2013) 2020–2024.
- [114] D.K. Shin, K.W. Jang, S.C. Ur, I.H. Kim, Thermoelectric properties of higher manganese silicides prepared by mechanical alloying and hot pressing, *J. Electron. Mater.* 42 (2013) 1756–1761.
- [115] D.Y.N. Truong, H. Kleinke, F. Gascoin, Thermoelectric properties of higher manganese silicide/multi-walled carbon nanotube composites, *Dalt. Trans.* 43 (2014) 15092–15097.
- [116] C. Suryanarayana, Mechanical alloying and milling, *Prog. Mater. Sci.* 46 (2001) 1–184.
- [117] B.S. Murty, S. Ranganathan, Novel materials synthesis by mechanical alloying/milling, *Int. Mater. Rev.* 43 (1998) 101–141.
- [118] A. Sundararajan, B.G. Thomas, Heat Transfer During Melt Spinning of Al-7 % Si Alloy on a Cu-Be Wheel, in: *Mater. Soc. Annu. Meet.*, 2008: pp. 793–810.
- [119] V.I. Tkatch, S.N. Denisenko, O.N. Beloshov, Direct measurements of the cooling rates in the single roller rapid solidification technique, *Acta Mater.* 45 (1997)



2821–2826.

- [120] M. Cutler, N.F. Mott, Observation of anderson localization in an electron gas, *Phys. Rev.* 181 (1969) 1336–1340.
- [121] T.H.C. Childs, Dry and boundary lubricated sliding friction and wear for engine component materials, *Tribol. Ser.* 26 (1993) 51–74.
- [122] J.N. Panda, J. Bijwe, R.K. Pandey, Role of treatment to graphite particles to increase the thermal conductivity in controlling tribo-performance of polymer composites, *Wear.* 360–361 (2016) 87–96.
- [123] J. ichi Tani, H. Kido, Thermoelectric properties of Sb-doped Mg<sub>2</sub>Si semiconductors, *Intermetallics.* 15 (2007) 1202–1207.
- [124] Y. Niwa, Y. Todaka, T. Masuda, T. Kawai, M. Umemoto, Thermoelectric Properties of Ca-Mg-Si Alloys, *Mater. Trans.* 50 (2009) 1725–1729.
- [125] J. ichi Tani, H. Kido, Thermoelectric properties of Al-doped Mg<sub>2</sub>Si<sub>1-x</sub>Sn<sub>x</sub> ( $x \leq 0.1$ ), *J. Alloys Compd.* 466 (2008) 335–340.
- [126] T. Sakamoto, T. Iida, A. Matsumoto, Y. Honda, T. Nemoto, J. Sato, T. Nakajima, H. Taguchi, Y. Takanashi, Thermoelectric characteristics of a commercialized Mg<sub>2</sub>Si source doped with Al, Bi, Ag, and Cu, *J. Electron. Mater.* 39 (2010) 1708–1713.
- [127] M. Akasaka, T. Iida, A. Matsumoto, K. Yamanaka, Y. Takanashi, T. Imai, N. Hamada, The thermoelectric properties of bulk crystalline n- and p-type Mg<sub>2</sub>Si prepared by the vertical Bridgman method, *J. Appl. Phys.* 104 (2008) 13703.
- [128] Q.S. Meng, W.H. Fan, R.X. Chen, Z.A. Munir, Thermoelectric properties of Sc- and Y-doped Mg<sub>2</sub>Si prepared by field-activated and pressure-assisted reactive sintering, *J. Alloys Compd.* 509 (2011) 7922–7926.
- [129] J.I. Tani, H. Kido, Fabrication and thermoelectric properties of Mg<sub>2</sub>Si-based composites using reduction reaction with additives, *Intermetallics.* 32 (2013) 72–80.
- [130] N. Satyala, J.S. Krasinski, D. Vashaee, Simultaneous enhancement of mechanical and thermoelectric properties of polycrystalline magnesium silicide with conductive glass inclusion, *Acta Mater.* 74 (2014) 141–150.
- [131] J.-Y. Jung, I.-H. Kim, Solid-State Synthesis of Te-Doped Mg<sub>2</sub>Si, *J. Electron. Mater.* 40 (2011) 1144–1149.
- [132] J.I. Tani, H. Kido, Thermoelectric properties of Bi-doped Mg<sub>2</sub>Si semiconductors, *Phys. B Condens. Matter.* 364 (2005) 218–224.

- [133] S. Fiameni, S. Battiston, S. Boldrini, A. Famengo, F. Agresti, S. Barison, M. Fabrizio, Synthesis and characterization of Bi-doped Mg 2Si thermoelectric materials, *J. Solid State Chem.* 193 (2012) 142–146.
- [134] M. Ioannou, G. Polymeris, E. Hatzikraniotis, A.U. Khan, K.M. Paraskevopoulos, T. Kyratsi, Solid-state synthesis and thermoelectric properties of Sb-doped Mg 2Si materials, *J. Electron. Mater.* 42 (2013) 1827–1834.
- [135] J.I. Tani, H. Kido, Thermoelectric properties of P-doped Mg<sub>2</sub>Si semiconductors, *Japanese J. Appl. Physics*,. 46 (2007) 3309–3314.
- [136] H. Ihou-Mouko, C. Mercier, J. Tobola, G. Pont, H. Scherrer, Thermoelectric properties and electronic structure of p-type Mg<sub>2</sub>Si and Mg<sub>2</sub>Si<sub>0.6</sub>Ge<sub>0.4</sub> compounds doped with Ga, *J. Alloys Compd.* 509 (2011) 6503–6508.
- [137] Q. Zhang, J. He, T.J. Zhu, S.N. Zhang, X.B. Zhao, T.M. Tritt, High figures of merit and natural nanostructures in Mg<sub>2</sub>Si 0.4Sn<sub>0.6</sub> based thermoelectric materials, *Appl. Phys. Lett.* 93 (2008) 102109.
- [138] X. Zhou, G. Wang, H. Chi, X. Su, J.R. Salvador, W. Liu, X. Tang, C. Uher, Thermoelectric performance of Sb- and La-doped Mg 2Si 0.5Ge 0.5, *J. Electron. Mater.* 41 (2012) 1589–1594.
- [139] V. Zaitsev, M. Fedorov, E. Gurieva, I. Eremin, P. Konstantinov, A. Samunin, M. Vedernikov, Highly effective Mg<sub>2</sub>Si<sub>1-x</sub>Sn<sub>x</sub> thermoelectrics, *Phys. Rev. B.* 74 (2006) 45207.
- [140] D. Cederkrantz, N. Farahi, K.A. Borup, B.B. Iversen, M. Nygren, A.E.C. Palmqvist, Enhanced thermoelectric properties of Mg<sub>2</sub>Si by addition of TiO<sub>2</sub> nanoparticles, *J. Appl. Phys.* 111 (2012) 23701.
- [141] W. Liu, X. Tan, K. Yin, H. Liu, X. Tang, J. Shi, Q. Zhang, C. Uher, Convergence of conduction bands as a means of enhancing thermoelectric performance of n-type Mg 2Si 1-xSn x solid solutions, *Phys. Rev. Lett.* 108 (2012) 166601.
- [142] X. Zhang, Q. Lu, L. Wang, F. Zhang, J. Zhang, Preparation of Mg<sub>2</sub>Si<sub>1-x</sub> Sn x by Induction Melting and Spark Plasma Sintering, and Thermoelectric Properties, *J. Electron. Mater.* 39 (2010) 1413–1417.
- [143] O. Janka, J. V. Zaikina, S.K. Bux, H. Tabatabaifar, H. Yang, N.D. Browning, S.M. Kauzlarich, Microstructure investigations of Yb- and Bi-doped Mg<sub>2</sub>Si prepared from metal hydrides for thermoelectric applications, *J. Solid State Chem.* 245 (2017) 152–159.
- [144] J.E. Bauerle, Study of solid electrolyte polarization by a complex admittance

- method, *J. Phys. Chem. Solids*. 30 (1969) 2657–2670.
- [145] N.M. Beekmans, L. Heyne, Correlation between impedance, microstructure and composition of calcia-stabilized zirconia, *Electrochim. Acta*. 21 (1976) 303–310.
- [146] T. van Dijk, A.J. Burggraaf, Grain boundary effects on ionic conductivity in ceramic  $Gd_xZr_{1-x}O_{2-(x/2)}$  solid solutions, *Phys. Status Solidi*. 63 (1981) 229–240.
- [147] M. Liu, X.Y. Qin, Enhanced thermoelectric performance through energy-filtering effects in nanocomposites dispersed with metallic particles, *Appl. Phys. Lett.* 101 (2012) 132103.
- [148] N. Wakeham, A.F. Bangura, X. Xu, J.-F. Mercure, M. Greenblatt, N.E. Hussey, Gross violation of the Wiedemann–Franz law in a quasi-one-dimensional conductor, *Nat. Commun.* 2 (2011) 396.
- [149] C.L. Kane, M.P.A. Fisher, Thermal Transport in a Luttinger Liquid, *Phys. Rev. Lett.* 76 (1996) 3192–3195.
- [150] A.J. Minnich, M.S. Dresselhaus, Z.F. Ren, G. Chen, Bulk nanostructured thermoelectric materials: current research and future prospects, *Energy Environ. Sci.* 2 (2009) 466.
- [151] P. Pichanusakorn, P. Bandaru, Nanostructured thermoelectrics, *Mater. Sci. Eng. R Reports*. 67 (2010) 19–63.
- [152] N. Nafsin, R.H.R. Castro, Direct measurements of quasi-zero grain boundary energies in ceramics, *J. Mater. Res.* 32 (2017) 166–173.
- [153] C. Sealy, Dopants go against the grain in ceramics, *Mater. Today*. 20 (2017) 159.
- [154] N.J. Kidner, N.H. Perry, T.O. Mason, E.J. Garboczi, The brick layer model revisited: Introducing the nano-grain composite model, *J. Am. Ceram. Soc.* 91 (2008) 1733–1746.
- [155] A. Michels, C.E. Krill, H. Ehrhardt, R. Birringer, D.T. Wu, Modelling the influence of grain-size-dependent solute drag on the kinetics of grain growth in nanocrystalline materials, *Acta Mater.* 47 (1999) 2143–2152.
- [156] T.H. An, S.M. Choi, W.S. Seo, C. Park, I.H. Kim, S.U. Kim, The effect of microstructure on the thermoelectric properties of polycrystalline higher manganese silicides, *Jpn. J. Appl. Phys.* 52 (2013) 10MC11.
- [157] P. Bellanger, S. Gorsse, G. Bernard-Granger, C. Navone, A. Redjaimia, S. Vivès, Effect of microstructure on the thermal conductivity of nanostructured  $Mg_2(Si,Sn)$  thermoelectric alloys: An experimental and modeling approach, *Acta*

- Mater. 95 (2015) 102–110.
- [158] Z. Li, J.F. Dong, F.H. Sun, S. Hirono, J.F. Li, Significant Enhancement of the Thermoelectric Performance of Higher Manganese Silicide by Incorporating MnTe Nanophase Derived from Te Nanowire, *Chem. Mater.* 29 (2017) 7378–7389.
- [159] X. Shi, X. Shi, Y. Li, Y. He, L. Chen, Q. Li, Enhanced power factor of higher manganese silicide via melt spin synthesis method, *J. Appl. Phys.* 116 (2014) 245104.
- [160] S. Vivès, C. Navone, E. Gaudin, S. Gorsse, Improved microstructure and thermoelectric properties of higher manganese silicide processed by reactive spark plasma sintering, *J. Mater. Sci.* 52 (2017) 12826–12833.
- [161] D.Y. Nhi Truong, D. Berthebaud, F. Gascoin, H. Kleinke, Molybdenum, Tungsten, and Aluminium Substitution for Enhancement of the Thermoelectric Performance of Higher Manganese Silicides, *J. Electron. Mater.* 44 (2015) 3603–3611.
- [162] D. V. Dudina, A.K. Mukherjee, Reactive spark plasma sintering: Successes and challenges of nanomaterial synthesis, *J. Nanomater.* 2013 (2013) 625218.
- [163] Z.G. Chen, G. Hana, L. Yanga, L. Cheng, J. Zou, Nanostructured thermoelectric materials: Current research and future challenge, *Prog. Nat. Sci. Mater. Int.* 22 (2012) 535–549.
- [164] Q. Hao, G. Zhu, G. Joshi, X. Wang, A. Minnich, Z. Ren, G. Chen, Theoretical studies on the thermoelectric figure of merit of nanograined bulk silicon, *Appl. Phys. Lett.* 97 (2010) 63109.
- [165] G. Chen, G.H. Zhu, H. Lee, Y.C. Lan, X.W. Wang, G. Joshi, D.Z. Wang, J. Yang, D. Vashaee, H. Guilbert, A. Pillitteri, M.S. Dresselhaus, Z.F. Ren, Increased Phonon Scattering by Nanograins and Point Defects in Nanostructured Silicon with a Low Concentration of Germanium, *Phys. Rev. Lett.* 102 (2009) 196803.
- [166] G. Chen, Phonon heat conduction in nanostructures, *Int. J. Therm. Sci.* 39 (2000) 471–480.
- [167] W. Kim, J. Zide, A. Gossard, D. Klenov, S. Stemmer, A. Shakouri, A. Majumdar, Thermal conductivity reduction and thermoelectric figure of merit increase by embedding nanoparticles in crystalline semiconductors, *Phys. Rev. Lett.* 96 (2006) 45901.

- [168] G. Cabouro, S. Chevalier, E. Gaffet, Y. Grin, F. Bernard, Reactive sintering of molybdenum disilicide by spark plasma sintering from mechanically activated powder mixtures: Processing parameters and properties, *J. Alloys Compd.* 465 (2008) 344–355.
- [169] X.B. Zhao, X.H. Ji, Y.H. Zhang, T.J. Zhu, J.P. Tu, X.B. Zhang, Bismuth telluride nanotubes and the effects on the thermoelectric properties of nanotube-containing nanocomposites Bismuth telluride nanotubes and the effects on the thermoelectric properties of nanotube-containing nanocomposites, *Appl. Phys. Lett.* 86 (2005) 62111.
- [170] Z. Zamanipour, X. Shi, M. Mozafari, J.S. Krasinski, L. Tayebi, D. Vashaee, Synthesis, characterization, and thermoelectric properties of nanostructured bulk p-type MnSi<sub>1.73</sub>, MnSi<sub>1.75</sub>, and MnSi<sub>1.77</sub>, *Ceram. Int.* 39 (2013) 2353–2358.
- [171] X. Tang, W. Xie, H. Li, W. Zhao, Q. Zhang, M. Niino, Preparation and thermoelectric transport properties of high-performance p-type Bi<sub>2</sub>Te<sub>3</sub> with layered nanostructure, *Appl. Phys. Lett.* 90 (2007) 12102.
- [172] W. Xie, J. He, H.J. Kang, X. Tang, S. Zhu, M. Laver, S. Wang, J.R.D. Copley, C.M. Brown, Q. Zhang, T.M. Tritt, Identifying the specific nanostructures responsible for the high thermoelectric performance of (Bi,Sb)<sub>2</sub>Te<sub>3</sub> nanocomposites, *Nano Lett.* 10 (2010) 3283–3289.
- [173] H. Li, X. Tang, Q. Zhang, C. Uher, Rapid preparation method of bulk nanostructured Yb<sub>0.3</sub>Co<sub>4</sub>Sb<sub>12+y</sub> compounds and their improved thermoelectric performance, *Appl. Phys. Lett.* 93 (2008) 252109.
- [174] G. Tan, Y. Zheng, X. Tang, High thermoelectric performance of nonequilibrium synthesized CeFe<sub>4</sub>Sb<sub>12</sub> composite with multi-scaled nanostructures, *Appl. Phys. Lett.* 103 (2013) 183904.
- [175] G. Tan, W. Liu, S. Wang, Y. Yan, H. Li, X. Tang, C. Uher, Rapid preparation of CeFe<sub>4</sub>Sb<sub>12</sub> skutterudite by melt spinning: rich nanostructures and high thermoelectric performance, *J. Mater. Chem. A.* 1 (2013) 12657.
- [176] Q. Zhang, Y. Zheng, X. Su, K. Yin, X. Tang, C. Uher, Enhanced power factor of Mg<sub>2</sub>Si<sub>0.3</sub>Sn<sub>0.7</sub> synthesized by a non-equilibrium rapid solidification method, *Scr. Mater.* 96 (2015) 1–4.
- [177] V.I. Tkatch, A.I. Limanovskii, S.N. Denisenko, S.G. Rassolov, The effect of the melt-spinning processing parameters on the rate of cooling, *Mater. Sci. Eng. A.* 323 (2002) 91–96.

- [178] T. Gheiratmand, H.R.M. Hosseini, P. Davami, F. Ostadhossein, M. Song, M. Gjoka, On the effect of cooling rate during melt spinning of FINEMET ribbons, *Nanoscale*. 5 (2013) 7520–7527.
- [179] D. Turnbull, Formation of crystal nuclei in liquid metals, *J. Appl. Phys.* 21 (1950) 1022–1028.
- [180] J.P. Heremans, C.M. Thrush, D.T. Morelli, Thermopower enhancement in PbTe with Pb precipitates, *J. Appl. Phys.* 98 (2005) 63703.
- [181] J.M. Zide, D.O. Klenov, S. Stemmer, A.C. Gossard, G. Zeng, J.E. Bowers, D. Vashaee, A. Shakouri, Thermoelectric power factor in semiconductors with buried epitaxial semimetallic nanoparticles, *Appl. Phys. Lett.* 87 (2005) 112102.
- [182] L.-D. Zhao, V.P. Dravid, M.G. Kanatzidis, The panoramic approach to high performance thermoelectrics, *Energy Environ. Sci.* 7 (2014) 251–268.
- [183] M. Saravanan, R.M.Pillai, B.C.Pai, Equal channel angular pressing of aluminium alloys and composites -An overview, *Alum. India*. 5 (2005) 3–14.
- [184] C.A. Schuh, Nanoindentation studies of materials, *Mater. Today*. 9 (2006) 32–40.
- [185] W.C. Oliver, G.M. Pharr, An improved technique for determining hardness and elastic modulus using load and displacement sensing indentation experiments, *J. Mater. Res.* 7 (1992) 1564–1583.
- [186] A. Krishna, N. Vijayan, B. Singh, K. Thukral, K.K. Maurya, Crystalline perfection and mechanical investigations on vertical Bridgman grown Bismuth telluride ( $\text{Bi}_2\text{Te}_3$ ) single crystals for thermoelectric applications, *Mater. Sci. Eng. A*. 657 (2016) 33–37.
- [187] Y.K. Masashi Ishikawa, Takashi Nakamura, Shusaku Hirata, Tsutomu Iida, Keishi Nishio, Mechanical properties of  $\text{Mg}_2\text{Si}$  with metallic binders, *Jpn. J. Appl. Phys.* 54 (2015) 07JC03.
- [188] L.D. Zhao, B.P. Zhang, J.F. Li, M. Zhou, W.S. Liu, J. Liu, Thermoelectric and mechanical properties of nano-SiC-dispersed  $\text{Bi}_2\text{Te}_3$  fabricated by mechanical alloying and spark plasma sintering, *J. Alloys Compd.* 455 (2008) 259–264.
- [189] F. Ren, B.D. Hall, J.E. Ni, E.D. Case, J. Sootsman, M.G. Kanatzidis, E. Lara-Curzio, R.M. Trejo, E.J. Timm, Mechanical Characterization of PbTe-based Thermoelectric Materials, in: *MRS Proc.*, 2008: pp. 121–126.
- [190] J.E. Ni, E.D. Case, K.N. Khabir, R.C. Stewart, C.I. Wu, T.P. Hogan, E.J. Timm, S.N. Girard, M.G. Kanatzidis, Room temperature Young's modulus, shear

- modulus, Poisson's ratio and hardness of PbTe-PbS thermoelectric materials, *Mater. Sci. Eng. B Solid-State Mater. Adv. Technol.* 170 (2010) 58–66.
- [191] K. Tyagi, B. Gahtori, S. Bathula, M. Jayasimhadri, S. Sharma, N.K. Singh, D. Haranath, A.K. Srivastava, A. Dhar, Crystal structure and mechanical properties of spark plasma sintered Cu<sub>2</sub>Se: An efficient photovoltaic and thermoelectric material, *Solid State Commun.* 207 (2015) 21–25.
- [192] K. Niihara, A fracture mechanics analysis of indentation-induced Palmqvist crack in ceramics, *J. Mater. Sci. Lett.* 2 (1983) 221–223.
- [193] K. Niihara, R. Morena, D.P.H. Hasselman, Evaluation of K<sub>Ic</sub> of brittle solids by the indentation method with low crack-to-indent ratios, *J. Mater. Sci. Lett.* 1 (1982) 13–16.
- [194] M. Tanaka, N. Fujimoto, K. Higashida, Fracture Toughness Enhanced by Grain Boundary Shielding in Submicron-Grained Low Carbon Steel, *Mater. Trans.* 49 (2008) 58–63.
- [195] M. Saravanan, B. Sivaiah, A.K. Srivastava, A. Dhar, Ultrafine grain structure features in spray-formed AZ31 magnesium alloy, *Mater. Des.* 60 (2014) 21–25.
- [196] J.R. Salvador, J. Yang, X. Shi, H. Wang, A.A. Wereszczak, H. Kong, C. Uher, Transport and mechanical properties of Yb-filled skutterudites, *Philos. Mag.* 89 (2009) 1517–1534.
- [197] S. Bathula, B. Gahtori, M. Jayasimhadri, S.K. Tripathy, K. Tyagi, A.K. Srivastava, A. Dhar, Microstructure and mechanical properties of thermoelectric nanostructured n-type silicon-germanium alloys synthesized employing spark plasma sintering, *Appl. Phys. Lett.* 105 (2014) 61902.
- [198] T. Sakamoto, T. Iida, Y. Honda, M. Tada, T. Sekiguchi, K. Nishio, Y. Kogo, Y. Takanashi, The use of transition-metal silicides to reduce the contact resistance between the electrode and sintered n-type Mg<sub>2</sub>Si, *J. Electron. Mater.* 41 (2012) 1805–1810.
- [199] P. Koteswaram, Meteorology and climatology of the Rajasthan desert, *Proc. Indian Natn. Sci. Acad.* 44 (1978) 401–410.
- [200] R. Singh, R. Pandey, Rooplal, M. Ranganath, S. Maji, Tribological performance analysis of textured steel surfaces under lubricating conditions, *Surf. Topogr. Metrol. Prop.* 4 (2016) 34005.
- [201] J.F. Archard, Wear Theory and Mechanisms, *Wear.* (1980) 35–80.

---

---

## RESEARCH PUBLICATIONS

(Included in this thesis)

---

---

1. **Saravanan Muthiah**, R.C.Singh, B. D. Pathak, P.K. Avasthi, R. Kumar, A. Kumar, A. K. Srivastava, and Ajay Dhar.  
Significant enhancement in thermoelectric performance of nanostructured higher manganese silicide synthesized employing melt spinning technique.  
*2018, Nanoscale, Vol.10, 1970-1977.*
2. **Saravanan Muthiah**, R.C.Singh, B. D. Pathak and Ajay Dhar.  
Mechanical properties of thermoelectric n-type magnesium silicide synthesized employing in-situ spark plasma reaction sintering.  
*2017, Material Research Express, Vol.4, 075507*
3. **Saravanan Muthiah**, R.C.Singh, B.D. Pathak and Ajay Dhar.  
Facile synthesis of higher manganese silicide employing spark plasma assisted reaction sintering with enhanced thermoelectric performance.  
*2016, Scripta Materialia, Vol.119, 60-64.*
4. **Saravanan Muthiah**, B. Sivaiah, B. Gahtori, K. Tyagi, A. K. Srivastava, B. D. Pathak, Ajay Dhar, and R. C. Budhani.  
Double-Doping Approach to Enhancing the Thermoelectric Figure-of-Merit of n-Type Mg<sub>2</sub>Si Synthesized by Use of Spark Plasma Sintering.  
*2014, Journal of Electronic Materials, Vol.43, 2035-2039.*
5. **Saravanan Muthiah**, J. Pulikkotil, A.K. Srivastava, A. Kumar, B.D. Pathak, Ajay Dhar, R.C. Budhani.  
Conducting grain boundaries enhancing thermoelectric performance in doped Mg<sub>2</sub>Si.  
*2013, Applied Physics Letters, Vol.103, 053901.*

---

---

## CONFERENCES

---

---

1. **Saravanan Muthiah**, R.C.Singh, B.D. Pathak and Ajay Dhar.  
Nanomechanical characterization of aluminium doped higher manganese silicide synthesized employing reactive spark plasma sintering.  
*2018, Presented at 1<sup>st</sup> International Conference on New Frontiers in Engineering, Science and Technology, January 8-12, Delhi Technological University; Delhi, India*
2. **Saravanan Muthiah**, R.C.Singh, B.D. Pathak and Ajay Dhar.  
Enhancement of thermoelectric performance in silicides employing spark plasma sintering technique.  
*2015, Presented at New Horizons in Materials Processing and Applications, November 13 - 16, Coimbatore, India.*



3. **Saravanan Muthiah**, A. K. Srivastava, B. D. Pathak, Ajay Dhar and R. C. Budhani.  
Enhanced thermoelectric performance in low-cost Magnesium Silicide thermoelectric materials by doping approach.  
*2013, Presented at 2<sup>nd</sup> TAPSUN Conference (Theme: Advances in Futuristic Solar Energy Materials & Technologies), September 13-14, CSIR – CLRI, Chennai, India.*
  
4. **Saravanan Muthiah**, B.Sivaiah, B. Gahtori, K.Tyagi, A.K. Srivastava, B. D. Pathak, Ajay Dhar and R. C. Budhani.  
Double doping approach for enhancing thermoelectric figure-of-merit in n-type Mg<sub>2</sub>Si synthesized using spark plasma sintering.  
*2013, Presented at 32<sup>nd</sup> International Conference on Thermoelectrics (ICT 2013), June 30- July 4, Kobe, Japan.*

## BIO-DATA OF THE AUTHOR

1. Name and full correspondence address : M. Saravanan  
23, Energy Materials Complex (HEPP),  
Advanced Materials & Devices Division,  
National Physical Laboratory (CSIR),  
Dr.K.S.Krishnan Marg,  
New Delhi-110012.
2. Email and contact number : [msaravanan04@gmail.com](mailto:msaravanan04@gmail.com)  
Tele (off.) 011-45609472  
Mob: 9958110772
3. Institution : National Physical Laboratory (CSIR)  
New Delhi-110012.
4. Date of Birth : 06 April 1981
5. Gender : Male
6. Research Experience:

S.No	Position held	Name of the Institution	From	To
1	Graduate Trainee	Liquid Propulsion Systems Centre (ISRO), Mahendragiri	August 2003	June 2004
2	Research Intern	National Institute for Interdisciplinary Science & Technology (CSIR), Thiruvananthapuram	June 2004	June 2006
3	Project Assistant	National Institute for Interdisciplinary Science & Technology (CSIR), Thiruvananthapuram	June 2006	October 2006
4	Junior Scientist	National Physical Laboratory (CSIR), New Delhi	March 2007	March 2010
5	Scientist	National Physical Laboratory (CSIR), New Delhi	March 2010	Till date

7. No. of SCI Publications: 20

8. Membership in Professional Scientific bodies:

- Life Member, The Institution of Engineers (India)
- Life Member, The Indian Institute of Metals (IIM)
- Life Member, Materials Research Society of India (MRSI)
- Life Member, Metrology Society of India (MSI)